Phonons of Epitaxially Grown Graphene on Ir(111) and Molecular Vibrational Excitations Studied by Angle-Resolved Electron Energy Loss Spectroscopy

D i s s e r t a t i o n

zur Erlangung des akademischen Grades
doctor rerum naturalium (Dr. rer. nat.)

der Fakultät für Mathematik und Naturwissenschaften
der Technischen Universität Ilmenau

vorgelegt von
M i c h a e l E n d l i c h
aus Nordhausen

Ilmenau 2016

1. Gutachter | Prof. Dr. Jörg Kröger
Technische Universität Ilmenau, Germany.

2. Gutachter | Prof. Dr. Siegfried Stapf
Technische Universität Ilmenau, Germany.

3. Gutachter | Prof. Dr. Ludger Wirtz
Université du Luxembourg, Luxembourg.

Tag der Einreichung | 7. Februar 2016
Tag der wissenschaftlichen Aussprache | 24. Mai 2016

urn:nbn:de:gbv:ilm1-2016000287

Contents

Introduction

The surprising experimental discovery of the two-dimensional carbon allotrope graphene has ushered in a new era of fundamental physics [1]. Previously, the existence of such a material was not expected since theoretical predictions argued that strictly two-dimensional crystals were thermodynamically unstable [2]. However, experimentalists could successfully isolate graphene by mechanical exfoliation [3]. Subsequent experiments by transmission electron microscopy provided subtle reasons for its stability since suspended graphene sheets exhibit corrugations in the third dimension [4]. Since its discovery, graphene has attracted tremendous interest owing to the ambipolar field effect [3, 5, 6], charge carriers behaving like massless Dirac fermions [7, 8], a linear band dispersion [9–11], extremely high charge-carrier mobilities [12–14], and ballistic electron transport at room temperature [15, 16]. Apart from the importance in terms of fundamental physics, graphene's exceptional physical properties make it also a promising candidate for future technology [17] such as high-performance field effect transistors on flexible substrates [18, 19], spin electronic devices with room temperature spin transport [20, 21] as well as flexible and transparent photonic and optoelectronic devices that are tunable over a wide energy range [22, 23].

From experiments in fundamental research to future technological applications, large-area graphene films with a high structural homogeneity combined with low production costs are required [24]. Such films can be epitaxially grown on metal surfaces by chemical vapor deposition [25]. Indeed, investigations into graphene on metal surfaces have firmly taken root in graphene research apart from mechanical exfoliation and epitaxial growth of graphene on silicon carbide [25]. To preserve the unique properties of graphene on metal surfaces as much as possible the preparation and characterization of single layers of graphene has become an increasingly important research field [25, 26]. Among the large variety of metal surfaces Ir(111) and Pt(111) are outstanding. The graphene–surface distance is $\approx 338\,\mathrm{pm}$ on Ir(111) [27] and $\approx 330\,\mathrm{pm}$ on Pt(111) [28]. These values represent the largest distances that have been reported for graphene on metal surfaces so far and imply a weak graphene–metal interaction. In fact, the characteristic electronic structure of graphene on Ir(111) is weakly affected since the Dirac cones at the $\bar{\mathrm{K}}$ point of the surface Brillouin zone are shifted only slightly above the Fermi level [29].

The high structural homogeneity of graphene on Ir(111) in combination with the preservation of virtually pristine graphene properties has provided impetus to detailed explorations of the growth kinetics [30–33], of the graphene–metal interaction [27, 34] and of the electronic band structure [29, 35]. In addition to a closed layer of graphene, the growth [36] and the exciting electronic phenomena [37–40] of graphene quantum dots supported on Ir(111) have been investigated. However, despite from these results which are entirely related to structural and electronic properties, there is a lack of experimental studies concerning the dynamical properties of graphene on metal surfaces with weak interaction. But a profound knowledge is indispensable since the dynamical properties of carbon materials have been shown to severely influence the electron transport properties. For instance, electron scattering from optical phonons leads to a collapse of the ballistic electron transport in carbon nanotubes [41, 42]. Likewise, the transport properties of graphene are affected by the interaction of electrons with acoustic [43, 44], optical [45] and flexural phonons [13, 46, 47]. Moreover, graphene on lattice mismatched metal surfaces exhibits superstructures to different extents [28, 48–50]. Such graphene superstructures can lead to new physical properties like an anisotropically renormalized group velocity of charge carriers around the Dirac point [51, 52], charge inhomogeneities and localized states [53], the appearance of additional branches of Dirac fermions [54, 55] and band gaps [56]. In fact, a replication of the Dirac cones and the opening of gaps in the electronic band structure has been demonstrated for graphene on Ir(111) [29, 35]. These results give serious reason for an impact of superstructures also on the dynamical properties of graphene.

Graphene on Ir(111) holds further potential. In recent years, the adsorption of increasingly complex molecules on well-defined, monocrystalline surfaces under ultrahigh vacuum conditions has become a crucial research area of surface physics and chemistry [57–59]. Geometrical, electronic and vibrational properties of molecules adsorbed to metal surfaces can be strongly modified due to a molecule–substrate interaction [60–66]. Such an interaction impairs the molecular gas phase properties which should be preserved on surfaces. Notably, these properties include sharp molecular orbitals which are important for long dwell times of electrons in catalytic reactions or during the conversion of light into electrical energy. Likewise, the performance of molecular electronic devices depends on fundamental properties regarding charge carrier mobilities and lifetimes which are strongly improved by the localization of electronic states [67, 68]. So far, thin dielectric films like oxides [69–73], alkali halides [67, 74–77], alkanethiols [78, 79], nitrides [80] or molecules [64, 68, 81] are used to decouple molecules from inorganic surfaces. However, such thin films are often structurally inhomogeneous. Furthermore, the polar character of the alkali halide layers can interfere with the properties of the adsorbed molecules.

An alternative and fairly new approach envisions graphene as a promising candidate to decouple molecules from metal surfaces. This is based on the assumption that graphene should be nearly inert because of its strong sp^2 hybridization. For a practical realization, graphene on Ir(111) is again excellently suitable. Due to its large graphene–substrate distance, which is nearly identical to the interlayer distance in graphite ($\approx 335\,\mathrm{pm}$), the electronic band structure is virtually unaffected compared to pristine graphene. Therefore, molecules adsorbed to graphene should be largely decoupled from Ir(111). Currently, there is an overwhelming abundance of experimental and theoretical studies that attempt to change electronic properties of graphene by adsorbing molecules [82–90]. However, only a few studies deal with the properties of the adsorbed molecules.

Several of these studies focus on structural and electronic properties [91]. The adsorption of PTCDA[1] molecules to graphene on silicon carbide allows the observation of long-range ordered two-dimensional supramolecular arrays [92, 93]. These arrays are not affected by defects in the graphene film and merely show a slight charge transfer from the adsorbed molecules to graphene [92, 93]. Further structural aspects of supramolecular arrays have been observed for the electron acceptor molecule TCNQ[2] adsorbed to graphene on Ir(111) [94], metal phthalocyanines[3] adsorbed to graphene on Ru(0001) [95], and PTCDI[4] derivatives adsorbed to graphene on Rh(111) [96]. The adsorption of BTP[5] molecules to graphene on Ru(0001) has been employed to investigate the interplay between molecule–molecule and molecule–substrate interactions [97].

Besides structural and electronic properties only a marginal amount of investigations sheds light on the dynamical properties of molecules adsorbed to graphene [98–100]. W. Dou *et al.* deposited phthalocyanines with different metallic centers on graphene at Ni(111) and characterized the system with inelastic electron scattering [99]. The Raman-active vibrations of iron(II) and cobalt(II) phthalocyanine showed asymmetric line shapes. Therefore, a strong interaction between the molecules and the Ni(111) surface can be inferred [101, 102]. Works of X. Ling *et al.* [98, 100] suggest an increased Raman signal for molecules adsorbed on a single layer of graphene. Here, the amount of amplification is dependent on the vibrational symmetry and on charge transfer.

[1] PTCDA is the acronym for the chemical compound perylene-3,4,9,10-tetracarboxylic dianhydride with the empirical formula $C_{24}H_8O_6$.

[2] TCNQ is the acronym for the chemical compound 7,7',8,8'-tetracyano-*p*-quinodimethane with the empirical formula $C_{12}H_4N_4$.

[3] In the study, the metal phthalocyanines iron(II) phthalocyanine and nickel(II) phthalocyanine with the empirical formula $C_{32}H_{16}N_8Fe$ and $C_{32}H_{16}N_8Ni$ were used.

[4] PTCDI is the acronym for the chemical compound 3,4,9,10-perylenetetracarboxylic diimide with the empirical formula $C_{24}H_{10}N_2O_4$.

[5] BTP is the acronym for the chemical compound 2,4'-bis(terpyridine) with the empirical formula $C_{40}H_{26}N_8$.

Although the dynamical properties are likewise an integral part of the mentioned systems, only little attention is paid to them so far. Therefore, the first part of the present thesis is devoted to the exploration of the dynamical properties of graphene on Ir(111). Large-area graphene films with a high structural homogeneity will be grown on Ir(111) by adopting established methods of graphene growth. In order to obtain the dynamical properties both with a high energy and angular resolution, the phonon dispersion relation of graphene on Ir(111) is determined by angle-resolved inelastic electron scattering. The second part of the thesis aims at demonstrating a possible decoupling of organic molecules from Ir(111) by an interjacent graphene layer. Furthermore, any potential influences of molecule–molecule and molecule–substrate interactions on the dynamical properties are supposed to be uncovered. For this purpose, molecules adsorbed on Ir(111) and on graphene will be investigated by vibrational spectroscopy. As organic molecules, phthalocyanines will be used because of their chemical and thermal stability as well as their easy-to-handle vaporizability under ultrahigh vacuum conditions. During the investigations, the following open questions will be addressed:

(a) Does the metal substrate influence the dynamical properties of graphene on Ir(111)?

(b) Will the superstructure of graphene on Ir(111) have an impact on the phonon dispersion relation of graphene?

(c) Can organic molecules like phthalocyanines be decoupled from Ir(111) by an interjacent graphene layer?

(d) Do phthalocyanines affect the dynamical properties of neighboring molecules?

For the elucidation of the questions detailed experimental studies, theoretical modeling and comparisons with the literature will be performed. **Chapter 1** briefly introduces the most relevant parts of the experimental setup including the instrumentation at the ultrahigh vacuum chamber, the cleaning of Ir(111), the growth of graphene and the molecule evaporation. A subsequent section focuses on angle-resolved inelastic electron scattering and, in particular, on the careful calibration of the scattering setup which is necessary to obtain accurate phonon dispersion relations.

Chapter 2 sheds light on the dynamical properties of graphene on Ir(111) and emphasizes the role of the metal substrate. The phonon dispersion relation of singly oriented graphene on Ir(111) is determined by means of angle-resolved inelastic electron scattering and density functional theory (DFT) calculations. Various deviations from the phonon dispersion relations of pristine graphene and graphite are observed across the surface Brillouin zone.

Chapter 3 elaborates on the decoupling of phthalocyanines from an Ir(111) substrate by means of an interjacent graphene layer. To demonstrate such a decoupling most clearly phthalocyanines are adsorbed to Ir(111) and to graphene on Ir(111). Both systems are studied by scanning tunneling microscopy (STM), vibrational spectroscopy and supporting DFT calculations.

Chapter 4 focuses on a possible utilization of carbon monoxide as a molecular probe for static electric dipole interactions on surfaces. For this purpose, carbon monoxide and phthalocyanines are coadsorbed on Ir(111). To uncover potential dipole-dipole interactions, the energy and the spectroscopic line shape of the C–O stretch mode are determined by means of vibrational spectroscopy and interpreted by detailed DFT calculations.

With these investigations, the thesis would like to make a small contribution to the scientific progress regarding the dynamical properties of two-dimensional materials on surfaces and the influence of molecule–molecule and molecule–substrate interactions on the dynamical properties of molecules adsorbed to surfaces. Perhaps, the work may even be an impetus for forthcoming research to expand and deepen the level of knowledge in these fields or to create new associations with other fields.

CHAPTER 1

Experimental

Angle-resolved inelastic electron scattering is a versatile and powerful tool to explore structural and dynamical properties of pristine surfaces as well as of molecules and two-dimensional layers at surfaces. In oder to enable measurements with this technique and to gain reliable and reproducible results extremely clean and long-range ordered crystalline surfaces are indispensable. Therefore, an ultrahigh vacuum system is necessary. In this regard, the first part of the chapter is devoted to introducing the ultrahigh vacuum surface analysis system (Section 1.1) which is followed by a description of the sample preparation including the cleaning of Ir(111), the growth of graphene and the evaporation of phthalocyanines (Section 1.2). The second part deals with the basics concerning inelastic electron scattering, with a particular emphasis on measuring phonon dispersion relations and analyzing molecule vibrations (Section 1.3).

1.1 Surface Analysis System

The surface analysis system (Fig. 1.1) consists of three ultrahigh vacuum chambers: a load lock chamber with a base pressure of 10^{-6} Pa as well as a preparation and an analysis chamber, both with a base pressure of 10^{-9} Pa.[1] The load lock chamber is used for transferring samples from ambient pressures to ultrahigh vacuum and *vise versa*. In order to clean and prepare samples, the preparation chamber is equipped with an ion sputtering gun, a filament for electron impact heating, an evaporator to deposit molecules on the sample surface, a quartz microbalance to monitor deposition rates, various gas inlets and a source for atomic hydrogen and deuterium. The analysis chamber holds the main analysis tool — an Ibach spectrometer providing angle-resolved inelastic electron scattering, also known as electron energy loss spectroscopy (EELS) or high-resolution electron energy loss spectroscopy. For this purpose, the manipulator does not only allow a movement of the sample in x-, y- and z-direction but also in polar and azimuthal direction. In addition, the sample can be analyzed by low-energy electron diffraction (LEED) and scanning tunneling microscopy.

[1] Mass spectra of the preparation and analysis chamber acquired at their base pressures are shown in Figs. A.1(a) and A.1(b) of Appendix A, respectively.

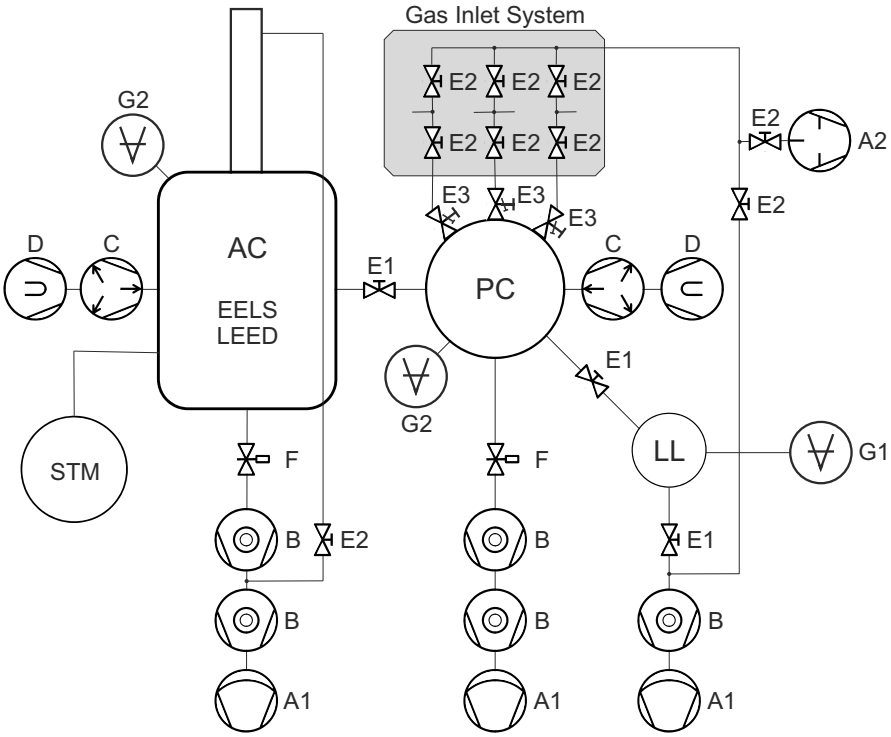

Fig. 1.1: Sketch of the surface analysis system which is divided in a load lock chamber (LL), a preparation chamber (PC) and an analysis chamber (AC). The ultrahigh vacuum system is pumped by diaphragm pumps (A1), a rotary vane pump (A2), turbomolecular pumps (B), ion pumps (C) and sometimes by titan sublimation pumps (D). In order to separate vacuum components from each other or to regulate the mass flow of gases several valves are available: hand valves (E1), bellows valves (E2), ultrahigh vacuum leak valves (E3) and gate valves (F). The pressures are determined by cold cathode (G1) and hot cathode (G2) ionization gauges.

To perform experiments in ultrahigh vacuum, the chambers are pumped by diaphragm and turbomolecular pumps. The slightly poorer final pressure of diaphragm pumps compared to rotary vane pumps is tolerated to avoid the diffusion of oil into the chambers. Only the gas inlet system can be evaporated by a rotary vane pump when high pump rates are required. Furthermore, the preparation and analysis chambers are evacuated by ion pumps and occasionally by titan sublimations pumps to reach a base pressure of 10^{-9} Pa. In case a chamber was exposed to ambient pressures, an annealing at temperatures above 370 K for at least 48 h has been initialized to get rid of adsorbed water and other residual gases on the chamber walls. The composition of the residual gas can be analyzed by two installed mass spectrometers. Finally, to insulate the whole surface analysis system from external vibrations a pneumatic vibration isolation system was installed.[2]

[2] We have used the S-2000 Stabilizer Series from the Newport Corporation, Irvine, CA 92606, USA.

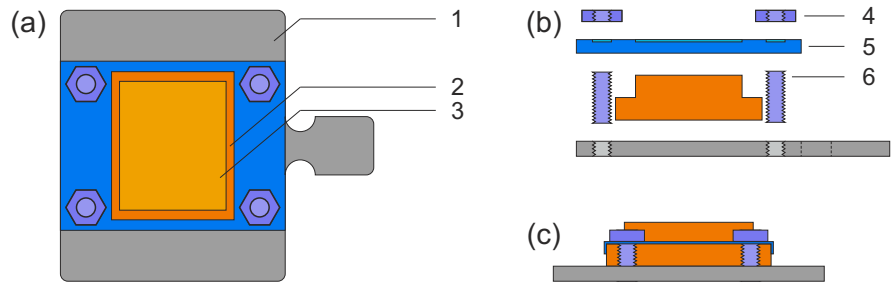

Fig. 1.2: Sketch of the sample holder: **(a)** top view, **(b)** side view and **(c)** front view. The sample holder consists of a Ta basic plate (1), an Ir single crystal (2) with a polished Ir(111) surface (3) as well as Mo nuts (4), a thin Mo sheet (5) and Mo threaded rods (6) to fix the crystal. Lightened areas in (b) indicate concealed bores.

1.2 Sample Preparation

The investigations are performed on a commercially available Ir(111) single crystal.[3] Its surface was oriented with an accuracy of less than 0.1° by chemical mechanical polishing. To carefully remove all residues of the polishing, the Ir(111) crystal was cleaned in an ultrasonic bath with acetone, 2-propanol, methanol and highly purified water. Immediately after, gaseous nitrogen was used to dry the crystal. The dried crystal was fixed in a highly temperature-stable and ultrahigh vacuum compatible sample holder (Fig. 1.2) consisting only of titanium and molybdenum parts which were previously annealed under vacuum conditions at 1200 K. The assembled sample holder was then transferred into the ultrahigh vacuum chamber.

Cleaning of Ir(111). Atomically smooth Ir(111) surfaces were prepared by repeated cycles of Ar^+ bombardment and annealing [103]. While sputtering, highly purified argon gas[4] was flowing through a home-made sputter gun with a partial pressure of 5×10^{-4} Pa. The argon atoms were ionized using electron bombardment. The focused ion beam was accelerated with 1500 V onto the sample surface. Each sputtering was followed by an annealing at 1200 K to restore the surface order. Higher temperatures were avoided to prevent diffusion of bulk impurities towards to the surface. A typical cleaning cycle includes a sputtering part with a duration of 600 s and an annealing part with a duration of 60 s. The sputter-annealing process was always repeated until low-energy diffraction pattern showed a clear Ir(111)-(1×1) structure and no adsorbate vibrations could be detected by inelastic electron scattering.

[3] Ordered from the Mateck GmbH, D-52428 Jülich, Germany. The purity is specified by the manufacturer with 99.99%.

[4] Ordered from the Air Liquide Deutschland GmbH, D-40235 Düsseldorf, Germany with a specified purity of 99.999%. A mass spectrum acquired in ultrahigh vacuum is given in Fig. A.2(a) of Appendix A.

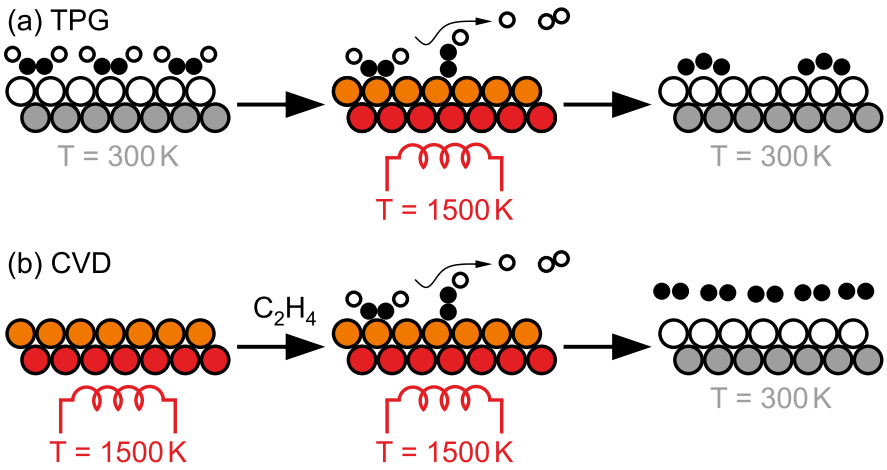

Fig. 1.3: Typical processes used for the growth of graphene on Ir(111): **(a)** temperature-programmed growth (TPG) and **(b)** growth by chemical vapor deposition (CVD) [104]. Small black (white) circles indicate carbon (hydrogen) atoms, large circles Ir atoms. During the growth of graphene chemisorbed ethene (C_2H_4) on Ir(111) is thermally and catalytically dissociated [105] as shown in the middle sketch of each row.

Growth of Graphene. In recent years, the growth of graphene on Ir(111) has been studied both experimentally [30, 31, 104, 106–111] and theoretically [33, 36]. Currently, two different growth methods are employed which expose clean Ir(111) surfaces to hydrocarbons, in particular to ethene (C_2H_4), at temperatures ranging from 900 K to 1500 K [104]. I. Temperature programmed growth [Fig. 1.3(a)] due to room temperature saturation of the Ir(111) surface with C_2H_4 molecules and their subsequent thermal decomposition at high temperatures. As a result, compact nanoscale graphene islands are formed whose size can be tuned from a few to a couple of tens of nanometers depending on the growth temperature. II. Chemical vapor deposition [Fig. 1.3(b)] of C_2H_4 to the hot Ir(111) surface. This method facilitates the growth of single-layer graphene with a high crystalline quality on the entire sample surface. Both growth processes are based on the catalytic activity of the Ir(111) surface [105]. As soon as the surface is completely covered by graphene, a further mass flow of C_2H_4 can not contribute to the growth of a second graphene layer. For our purposes, graphene was grown by chemical vapor deposition at 1500 K — a rather high temperature, which renders the growth with no rotational domains possible [108]. The partial pressure of purified ethene[5] was adjusted to 5×10^{-4} Pa. Exposure of clean Ir(111) to ethene for 120 s leads to a single layer of highly ordered and singly oriented graphene as revealed by low energy electron diffraction. The cleanliness of the prepared graphene film was checked by inelastic electron scattering.

[5] Ordered from the Air Liquide Deutschland GmbH, D-40235 Düsseldorf, Germany with a specified purity of 99.95%. A mass spectrum acquired in ultrahigh vacuum is given in Fig. A.2(b) of Appendix A.

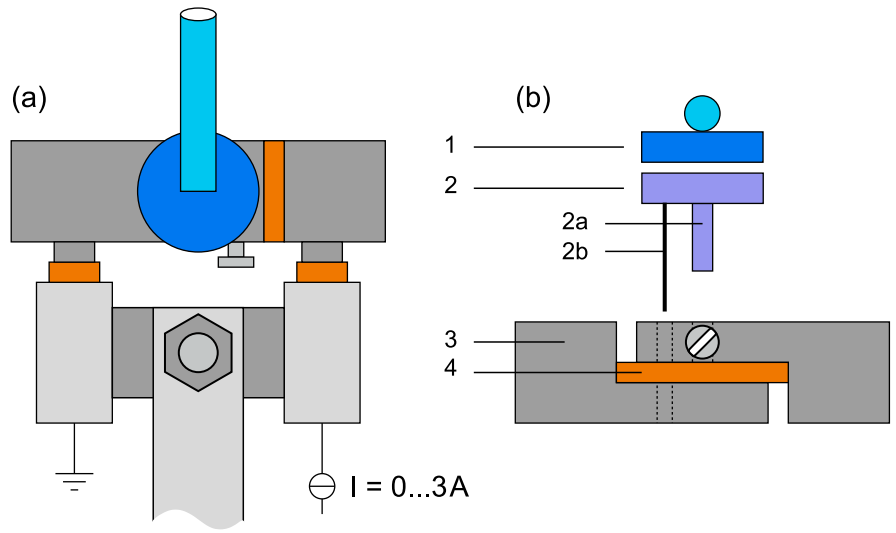

Fig. 1.4: Sketch of the home-made molecule evaporator: **(a)** top view and **(b)** front view. The evaporator consists of a Ta crucible (1), an ultra-high vacuum button heater (2) with a Mo body, a grounded lead (2a) and a power lead (2b), and diverse stainless steel parts (3) which are electrically isolated by Al_2O_3 ceramics (4).

Molecule Evaporation. A home-made evaporator was built for the deposition of organic molecules, in particular for the deposition of different phthalocyanine molecules[6]. The evaporator consists of an ultrahigh vacuum button heater[7] with an attached Ta crucible. The temperature of the button heater can be increased up to 1500 K. Before the first use, and typically prior to each refilling with molecules the evaporator was annealed *in situ* for 300–600 s with a current of 2.4 A at ≈ 1200 K to carefully remove all residual solvents and phthalocyanines. Thereafter, the evaporator was removed from the vacuum chamber, filled with molecules and reinstalled. In order to remove residual solvents from the molecule powder and adsorbed water from the evaporator, a current of 1.0 A, *i.e.*, a degassing temperature of ≈ 500 K was applied to the evaporator over night. The degassing temperature is well below the sublimation temperature of phthalocyanines which ranges between 700 K and 800 K [112, 113]. For the evaporation of phthalocyanine molecules the current through the button heater was set to 1.3–1.4 A depending on the used phthalocyanine compound. The crucible was then allowed to achieve thermal equilibrium within half an hour to ensure nearly constant deposition rates. All depositions were done at room temperature with the sample surface aligned perpendicular to the molecular beam. A subsequent substrate annealing to 500 K was applied when the molecules have been deposited on pristine Ir(111) surfaces.

[6] Ordered from Alfa Aesar, Heysham, Lancashire LA3 2XY, United Kingdom.
[7] Ordered from the HeatWave Labs, Inc., Watsonville, CA 95076, USA.

1.3 Angle-Resolved Inelastic Electron Scattering

Electron energy loss spectroscopy using inelastic scattering of electrons is a versatile and sensitive surface science tool to probe such exciting phenomena like adsorbate vibrations [114, 115], phonons [116, 117], plasmons [118, 119], electronic transitions [120] and spin waves [121, 122]. To this end, a monochromatized electron beam is reflected at a sample surface and the scattered electrons are detected energy- and angle-resolved. One of the first electron spectrometers was operated with an energy resolution of $\approx 50\,\mathrm{meV}$ [114]. Due to pioneering work on the electron optics led by H. Ibach [123–126] the latest spectrometer is able to reach a resolution below 1 meV [127], which has been demonstrated experimentally for carbon monoxide adsorbed on W(110) [128]. The angular resolution of the spectrometer enables the determination of physical properties as a function of the wave vector, *i.e.*, the recording of dispersion relations over the entire surface Brillouin zone. In dependence of the scattering conditions, the wave vector resolution around $\bar{\Gamma}$ is below $0.001\,\mathrm{\AA}^{-1}$ and for the entire surface Brillouin zone below $0.05\,\mathrm{\AA}^{-1}$. For investigations of adsorbed atoms and molecules, it may be important to know the limits of detectability. These limits can be affected by the dynamic dipole moment of the adsorbed species, the substrate temperature, the kinetic energy of the impinging electrons and the energy resolution of the spectrometer. In the case of strong dipole scatters like carbon monoxide detection limits in the range of 10^{-4} monolayers are possible [129, pp. 123-124].

Ibach Electron Spectrometer

In all experiments of the present thesis, an Ibach electron spectrometer as shown in Fig. 1.5 was used [127]. The key elements of the spectrometer are free-form electrostatic deflectors featuring stigmatic focusing at a deflection angle of $\approx 143°$ and angular aberration correction for small angles in the dispersion plane [130]. By correcting the focus, the deflectors can produce monochromatic electron beams with a higher intensity. In general, the spectrometer consists of a thermal cathode emission system, a 151° and a 143° cylindrical deflector in a row as monochromators, a lens system between the second monochromator and the sample, a second identical, but reversed lens system after the sample, an analyzer consisting of another 143° cylindrical deflector, and a channeltron detector. A LaB_6-cathode generates an intensive electron beam with a narrow energy distribution. Typically, a voltage of $\approx 2.4\,\mathrm{V}$ is applied to achieve a current of 1.55 A. The emitted electron beam is adapted to the entrance slit of the first monochromator by a Wehnelt cylinder and three electrostatic lenses (A-lenses). The first monochromator is a two-dimensional focusing and retarding deflector which additionally corrects space

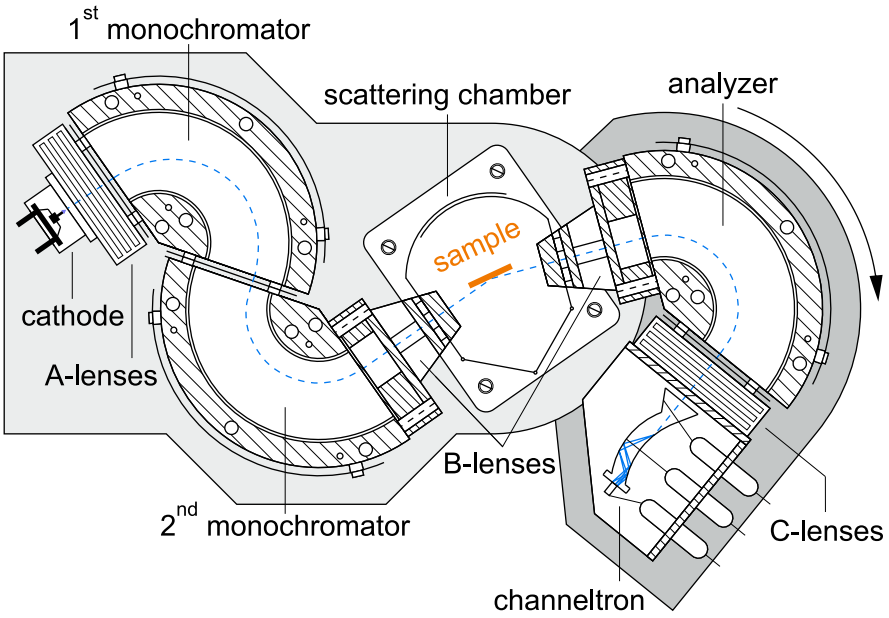

Fig. 1.5: Sketch of an Ibach spectrometer which features a hot cathode to generate an electron beam (blue line), a lens system (A-lenses), a 151° and a 143° cylindrical deflector in a row as monochromators, a lens system (B-lenses) between the second monochromator and the sample (orange line), a second identical, but reversed lens system after the sample, an analyzer consisting of another 143° cylindrical deflector, a further lens system (C-lenses) and a channeltron detector. The analyzing components (dark grey area) can be rotated by 65° relative to the fixed components of electron emission and monochromatization (light grey area). Partially adapted from [130].

charge effects. Such a correction is highly desirable since space charge effects in energy dispersive devices are the limiting factor in producing a high monochromatic current [126, p. 2]. The second monochromator is also two-dimensional focusing but not retarding. Using a first two-lens system (B-lenses), the electron beam is focused on the sample surface. Between the exit slit of the second monochromator and the scattering chamber, the electrons are accelerated by a freely adjustable voltage between 0 eV and 250 eV. The same voltage is applied to the scattering chamber and the sample manipulator to guarantee a nearly field-free motion of the electrons within the scattering chamber. In order to compensate work function differences, the sample is energized by an additional voltage. Using the second two-lens system (B-lenses), the reflected electron beam is focused on the analyzer system which is rotatable by 65°. The deflector of the analyzer is identical to the second monochromator. After passing the analyzer, the electron beam is focused on the channeltron by three further electrostatic lenses (C-lenses). Here, the beam triggers a secondary electron cascade which is electronically amplified and digitally recorded. In this way, energy losses of the scattered electrons can be detected from 0 eV to 50 eV. Further details regarding the spectrometer are reviewed by H. Ibach [126].

Calibration of the Spectrometer

In order to facilitate the determination of physical properties at different scattering conditions, the sample and the analyzer system of the spectrometer are rotatable whereas the direction of the incident electron beam is fixed[8]. Figure 1.6 illustrates the geometrical relations for the electron scattering process which occurs in the scattering chamber of the spectrometer (Fig. 1.5). Here, the polar coordinate systems of the manipulator and of the analyzer are initially independent from each other. The manipulator angle is measured in units of φ, the analyzer position in units of ϑ. However, an explicit relation between the sample orientation φ_s and the position of the analyzer ϑ_s where specularly reflected electrons can be detected is indispensable.

For that reason, an independent polar coordinate system is introduced. The pole of the system is defined by the intersection between the spectrometer axis[9] and the manipulator axis, its polar axis is given by the spectrometer axis and its polar angle ϕ is measured counterclockwise from the polar axis. First of all, the spectrometer without a sample is considered. The electron beam emerging from the monochromators and the spectrometer axis enclose a fixed angle of $\phi_\mathrm{m} = 35°$ [131]. After passing the empty spectrometer, the beam can be detected at the analyzer position ϑ_m. Secondly, the path of the electron beam is analyzed while the sample is inserted into the spectrometer. When the sample is rotated until its surface normal is parallel to the chamber axis at $\phi = 90°$, the calibration angle φ_0 can be read at the manipulator scale. As soon as the sample is rotated in an arbitrary orientation φ_s, the reflected electron beam can be detected in specular direction at the analyzer position ϑ_s. Using Fig. 1.6 the manipulator scale can be expressed in units of ϕ [Eq. (1.1)] and the angle of incidence α in units of the sample alignment φ_s [Eq. (1.2)]. Finally, the analyzer position ϑ_s for the detection of specularly reflected electrons can be evaluated[10] as function of φ_s [Eq. (1.3)] by using the conversion $\vartheta[°] = 2.3°/\mathrm{mm} \cdot \vartheta[\mathrm{mm}]$, which is applicable to our spectrometer.

$$\phi(\varphi) = \varphi - \varphi_0 \tag{1.1}$$

$$\alpha(\varphi_\mathrm{s}) = \phi_\mathrm{m} - \phi(\varphi_\mathrm{s}) = \phi_\mathrm{m} - (\varphi_\mathrm{s} - \varphi_0) \tag{1.2}$$

$$\vartheta_\mathrm{s}(\varphi_\mathrm{s}) = \vartheta_\mathrm{m} + \frac{2\alpha}{2.3°/\mathrm{mm}} = \vartheta_\mathrm{m} + \frac{2[\phi_\mathrm{m} - (\varphi_\mathrm{s} - \varphi_0)]}{2.3°/\mathrm{mm}} \tag{1.3}$$

[8] These conditions apply to our spectrometer ordered from the SPECS Surface Nano Analysis GmbH, D-13355 Berlin, Germany [131]. In other spectrometers the monochromator instead of the analyzer unit can be rotated.

[9] The spectrometer axis is used as reference axis because it can be unambiguously identified outside the ultrahigh vacuum chamber.

[10] The most difficult step is the estimation of φ_0. For an accurate calculation of ϑ_s, the value of φ_0 should be determined by averaging over several single measurements.

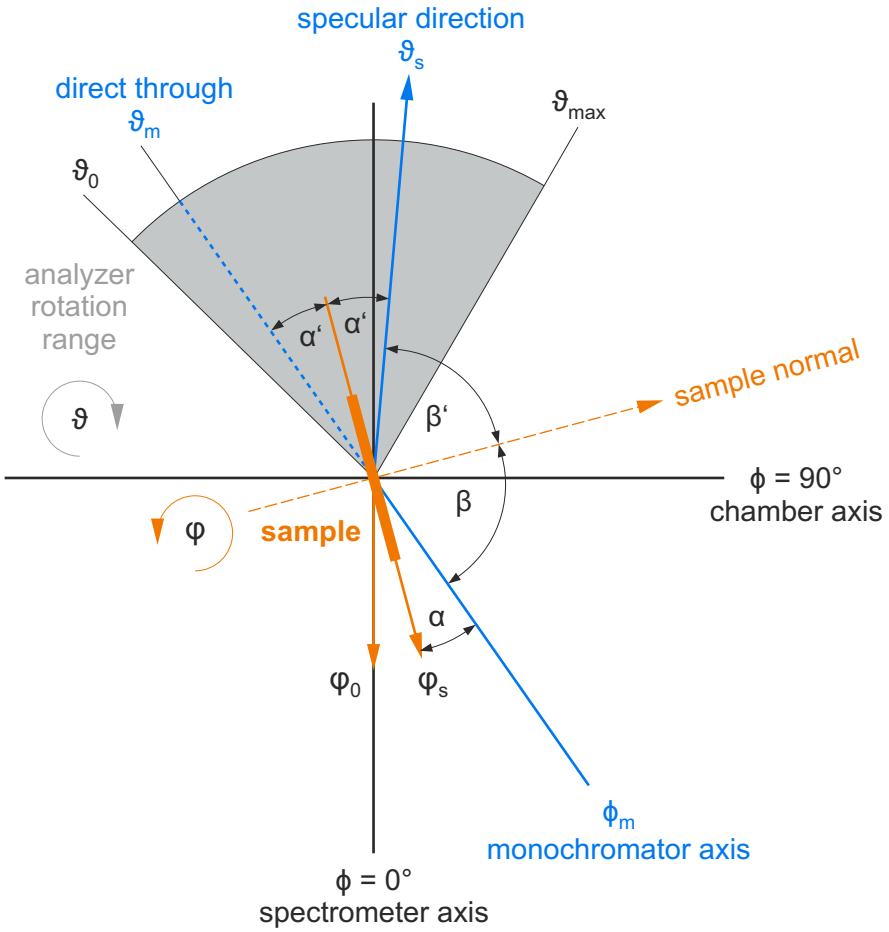

Fig. 1.6: Sketch of the global scattering geometry. A monochromatized electron beam (blue line) is specularly reflected at a sample surface (thick orange line) and collected by the analyzing components of the spectrometer which are rotatable between ϑ_0 and $\vartheta_{\max}$ (grey circular segment). A detailed description is given in the text.

A careful calibration of the spectrometer includes the determination of φ_0 and ϑ_m, which is especially recommended before measuring dispersion relations. In addition, the intersection of the incident electron beam and the sample surface should ideally coincide with the center of the analyzer rotation range (gray circular segment in Fig. 1.6). Misalignment of the sample may result in the detection of the reflected electron beam at an inaccurate analyzer position $\vartheta_\mathrm{s} \pm \Delta\vartheta\mathrm{s}$. Using the relation $2\alpha' = (\vartheta_\mathrm{s} - \vartheta_\mathrm{m}) \cdot 2.3°/\mathrm{mm}$, a misalignment leads to an inequality between the angle of incidence α and the angle of reflectance α'. The latter influences the calculation of the parallel wave vector transfer. To avoid inaccuracy, first, the ideal position ϑ_s of the analyzer should be set, and then, the detected beam intensity at the channeltron should be maximized by varying the sample position in x-, y- and z-direction.

Kinematics of Planar Scattering

After dealing with the spectrometer calibration, now, the kinematics of the scattering process are outlined. In general, scattering at surfaces is a three-dimensional problem. However, the used spectrometer restricts the scattering to two dimensions. Figure 1.7 shows a sketch of the scattering kinetics in the sagittal plane. Incident electrons, which can be described by plane waves with a wave vector $\vec{k}$ and a kinetic energy E, enclose an angle β with the normal of a planar sample surface. Elastically scattered electrons of the same kinetic energy leave the surface with a wave vector $\vec{k_\mathrm{s}}$, where $|\vec{k_\mathrm{s}}| = |\vec{k}|$, inelastically scattered electrons leave the surface with a kinetic energy E' and a wave vector $\vec{k'}$, where $|\vec{k'}| \neq |\vec{k}|$. The inelastic electron scattering process is accompanied by an energy transfer $\hbar\omega$ and a wave vector transfer $\vec{q}$. According to time-dependent quantum-mechanical perturbation theory, scattering of electrons at crystalline surfaces obeys the conservation of energy [Eq. (1.4)] and crystal momentum [Eq. (1.5)] parallel to the surface [132, p. 138].

$$E' = E \pm \hbar\omega(\vec{q_\parallel}) \tag{1.4}$$

$$\vec{k'_\parallel} = \vec{k_\parallel} \pm \vec{q_\parallel} \pmod{\vec{g_\parallel}} \tag{1.5}$$

Here, the plus sign describes the adsorption of a surface vibration, *i. e.*, the electron gains energy, the minus sign describes the excitation of a surface vibration, *i. e.*, the electron loses energy, and $\vec{g_\parallel}$ denotes a reciprocal surface lattice vector. The conservation of crystal momentum only applies for perfect crystalline surfaces and is a direct consequence of their two-dimensional translational symmetry [132, p. 153]. In the case of planar scattering, the magnitude of the parallel wave vector transfer $q_\parallel$ can be calculated with the aid of Eq. (1.6),

$$q_\parallel = \sqrt{\frac{2m_\mathrm{e}E}{\hbar^2}}\left[\sin(\beta') - \sqrt{1 - \frac{\hbar\omega}{E}}\sin(\beta' - \gamma')\right] \tag{1.6}$$

with m_e the electron mass. The angle β' can be evaluated as $90° - \alpha' = 90° - 1/2 \cdot (\vartheta_\mathrm{s} - \vartheta_\mathrm{m}) \cdot 2.3°/\mathrm{mm}$ (Fig. 1.6). The off-specular angle γ', which is defined anticlockwise from the specular direction, is determined by $(\vartheta_\mathrm{off} - \vartheta_\mathrm{s}) \cdot 2.3°/\mathrm{mm}$ with ϑ_off the position of the analyzer during an off-specular measurement (Fig. 1.7). Particularly with regard to the measurement of dispersion relations, it would be helpful to know the maximum $q_\parallel$ value, $q_\parallel^\mathrm{max}$, that can be achieved with a given sample orientation φ_s and kinetic energy E of impinging electrons. In order to calculate $q_\parallel^\mathrm{max}$ using Eq. (1.6), ϑ_off is replaced by ϑ_max, the maximum achievable position of the analyzer. If necessary, $q_\parallel^\mathrm{max}$ can be increased by

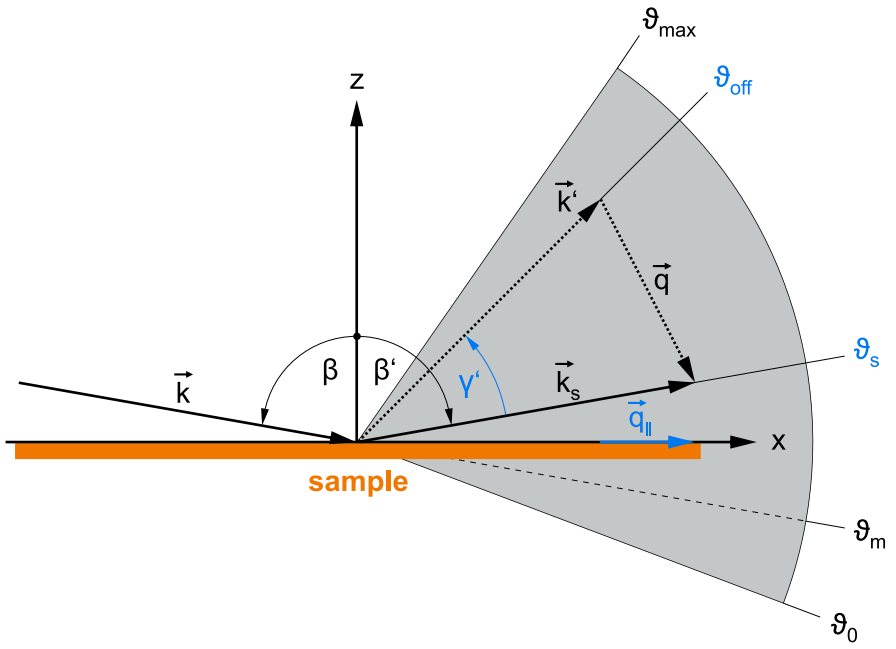

Fig. 1.7: Sketch of the scattering process in the sagittal plane, here shown as xz-plane. An incident electron with wave vector $\vec{k}$ is scattered at a planar sample surface (orange area) and encloses an angle β with the surface normal. Elastically scattered electrons with a wave vector $\vec{k_s}$ are detected at the analyzer position ϑ_s, inelastically scattered electrons with a wave vector $\vec{k'}$ at the analyzer position ϑ_off. The inelastic scattering process is accompanied by a wave vector transfer $\vec{q}$ which is conserved parallel to the surface. The magnitude of the parallel wave vector transfer $\vec{q_\parallel}$ is a function of the off-specular angle γ'. The analyzer can be rotated between ϑ_0 and ϑ_max (grey area). Adapted from [132, p. 154].

enlarging the range of γ' (Fig. 1.7), *i. e.*, by adjusting the sample orientation φ_s so that the angle β' is increased (Fig. 1.6). Another possibility is to increase E. Furthermore, it is crucial to estimate the accuracy of $q_\parallel$, an experimental value which is affected by different uncertainties. On this account, a first-order Taylor series expansion is used [Eq. (1.7)] since the uncertainty $\Delta q_\parallel$ is small compared with $q_\parallel$.

$$\Delta q_\parallel = \left|\frac{\partial q_\parallel}{\partial E}\right| \Delta E + \left|\frac{\partial q_\parallel}{\partial(\hbar\omega)}\right| \Delta(\hbar\omega) + \left|\frac{\partial q_\parallel}{\partial \beta'}\right| \Delta\beta' + \left|\frac{\partial q_\parallel}{\partial \gamma'}\right| \Delta\gamma' \tag{1.7}$$

The individual uncertainties can be estimated by $\Delta E = 20\,\mathrm{meV}$ according to detailed tests of the manufacturer of the electronics[11], $\Delta(\hbar\omega) \leq 1\,\mathrm{meV}$ using the best spectrometer resolution [127], $\Delta\beta' = 3.3E^{-0.33} \cdot \pi/180°$ for a spectrometer with $0.3\,\mathrm{mm} \times 3\,\mathrm{mm}$ monochromator slits and with E given in eV [133], and $\Delta\gamma' = 0.01\,\mathrm{mm} \cdot 2.3°/\mathrm{mm} \cdot \pi/180°$ referring to the smallest readable unit at the linear motion feedthrough.

[11] Private communication with the GCD Hard- & Software GmbH, D-91052 Erlangen, Germany.

Scattering Mechanisms

In response to first experimental achievements using inelastic electron scattering [114, 116, 134], several theoretical descriptions were developed to explain the underlying scattering mechanisms. These include a semiclassical treatment [135], a fully quantum mechanical model without [136] and with multiphonon processes [137] and an extended model based on electric field fluctuations without resorting to specific surface excitations [138]. Subsequently, theoretical treatments of molecules adsorbed at surfaces appeared [139–143]. The theories have been comprehensively reviewed by Ibach and Mills [129] and in part also by others [144, 145]. Hence, only a brief survey of the scattering theory is given.

Typically, two scattering regimes are distinguished — the dipole and the impact scattering regime. For specular scattering geometries, the inelastic cross section is dominated by dipole scattering (dipole scattering regime). Here, probe electrons are scattered at long-range electric dipole fields in the range of $\approx 100\,\text{Å}$ above the surface [102, 145]. These fields originate from dynamic dipole moments of molecular vibrations and all other elementary surface excitations which trigger charge density fluctuations. [129, p. 66]. So, the scattering is mediated by a Coulomb interaction between the electrical field of the incident electron and the dynamic dipole moment of the excitation [102]. The scattered electrons exhibit only small angular deviations from the specular direction and low wave vector transfers. Since the scattering takes place well above the surface, instead of a microscopic theory, a macroscopic dipole theory can adequately describe the scattering process.

In the dipole scattering regime, only dipole-active excitations which satisfy the surface dipole selection rule give reason to strong features in energy loss spectra. Within the framework of dielectric theory, this rule selects all excitations with a finite dynamic dipole moment $\vec{p}$ perpendicular to the surface. A qualitative explanation is given in Fig. 1.8 showing dynamic dipole moments of diatomic molecules on top of a semi-infinite metal crystal [132, p. 171]. In addition to the molecular dipole moments, $\vec{p}$, the induced image dipole moments, $\vec{p}_\text{i}$, in the metal also contributes to the total scattering cross section. For the sake of convenience we assume that $|\vec{p}_\text{i}| \approx |\vec{p}|$. Then, a molecular excitation with a dynamic dipole moment oriented perpendicular to the surface [Fig. 1.8(a)] and its image dipole moment add up to a total dipole moment of $\vec{P} = 2\vec{p}$. In contrast, a molecular excitation with a dynamic dipole moment oriented parallel to the surface [Fig. 1.8(b)] induces an antiparallel image dipole moment which compensates the first so that $\vec{P} = 0$. Alternatively, the surface dipole selection rule can be expressed in terms of group theory. Only those excitations which belong to the total symmetric representation

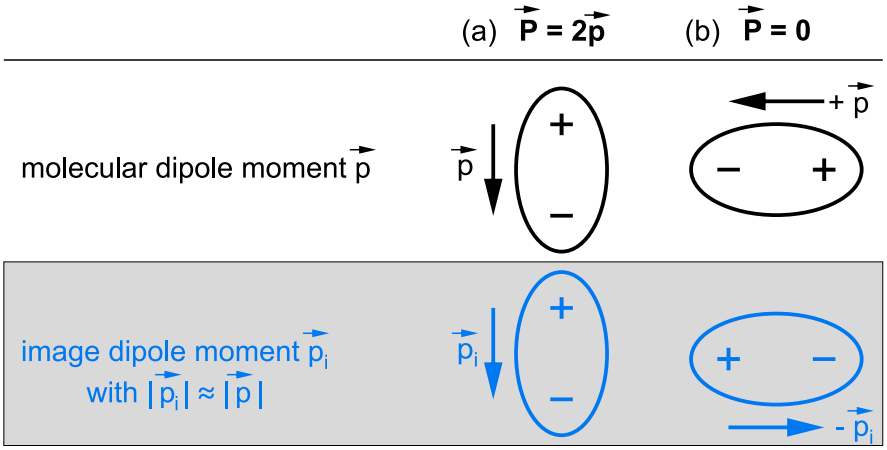

Fig. 1.8: Qualitative explanation of the surface selection rule in the dipole scattering regime. Molecular dipole moments, $\vec{p}$, and induced image dipole moments, $\vec{p}_\mathrm{i}$, of a diatomic molecule vibrating on a semi-infinite metal crystal are indicated by black and blue color, respectively. The total dipole moment $\vec{P}$ equals **(a)** $2\vec{p}$ for a vibration perpendicular to the surface, and **(b)** zero for a vibration parallel to the surface. Adapted from [132, p. 171].

are dipole-active in inelastic electron scattering experiments [132, p. 334]. In the case of chemisorption, the symmetry of the whole adsorbate complex, *i. e.*, the adsorbate together with the substrate has to be considered, and not only the symmetry of the free atom or molecule.

For off-specular scattering geometries, the inelastic cross section is dominated by impact scattering (impact scattering regime). Here, probe electrons which have a distance of $\approx 1\,\text{Å}$ to the surface are scattered by localized atomic potentials [102, 144]. Due to the short distance, an accurate description of the impact scattering requires a microscopic theory which utilizes plane waves for the incident and scattered electrons, spherically symmetric muffin tin potentials for the nuclei of the substrate and a multiple scattering formalism [146, 147]. The scattered electrons exhibit a broad angular distribution and high wave vector transfers. Selection rules are more difficult to derive than for the dipole scattering regime. In principle, almost all excitations are accessible. For planar scattering, however, excitations with a polarization parallel to the surface but perpendicular to the scattering plane can not be observed [145].

Summary and Conclusions

For the realization of the planned experiments an ultrahigh vacuum chamber is available. The subsequently described procedures facilitate the preparation of atomically clean Ir(111) surfaces, the growth of a single layer of highly ordered and singly oriented

graphene, and the controlled evaporation of different phthalocyanines. Owing to the electron energy loss spectroscopy we have a versatile and sensitive surface science tool to probe the dynamical properties of molecules and two-dimensional layers on surfaces. After a brief introduction to the used spectrometer design[12], the calibration of the spectrometer is explicated which is indispensable for an accurate determination of the phonon dispersion relation of graphene.[13] The following remarks on the kinetics of inelastic electron scattering were aimed at deriving equations for the calculation of the parallel wave vector $q_{\parallel}$ and its standard deviation $\Delta q_{\parallel}$. Finally, the relevant scattering mechanisms of inelastic electron scattering were elucidated. The provided information will help us below to interpret the energy loss spectra acquired in specular and off-specular direction.

[12] Here, we deliberately deviate from the latest manual [131]. The information described therein are partly not consistent with the monochromators of our spectrometer. The correct parameters could be ascertained in discussions with the scientific stuff of the SPECS Nano Analysis GmbH, D-13355 Berlin, Germany.

[13] Besides a calibration, also a fine-tuning of the spectrometer's electrostatic lenses and deflectors is necessary. For useful hints, which take the latest findings of H. Ibach into account, please consult Appendix B.

CHAPTER 2

Phonons of Graphene on Ir(111)

The results presented have been published in Physical Review B ***88****, 205403 (2013) and in Annalen der Physik (Berlin)* ***526****, 372 (2014). Theoretical support was provided by* ***Henrique Pereira Coutada Miranda****,* ***Alejandro Molina-Sánchez*** *and* ***Ludger Wirtz****, all from the Physics and Materials Science Research Unit, University of Luxembourg, Luxembourg.*

2.1 Phonon Dispersion Relation of Graphene on Ir(111)

The dynamical properties of carbon materials have been shown to severely influence their electron transport properties. For instance, electron scattering from optical phonons leads to a collapse of the ballistic electron transport in carbon nanotubes [41, 42]. Likewise, the transport properties of graphene in the high-current limit are affected by the interaction between electrons and optical phonons [45]. In addition, exploring phonon spectra of graphene may provide valuable information on the bonding of graphene with the substrate [148], the persistence of the Dirac cone [149], and the electron-phonon coupling [150]. Therefore, the precise knowledge of the phonon band structure of graphene on a metal surface is highly desirable for the understanding of the graphene–metal interaction and its underlying physics. However, the dynamical properties of graphene on metal surfaces with weak interaction have scarcely been addressed so far. Raman spectroscopy has been used to determine characteristic graphene phonon modes at $\bar{\Gamma}$ on two rotational variants of epitaxial, single-layer graphene on Ir(111) [151]. The phonon dispersion relations of graphene on Pt(111) have been determined by electron energy loss spectroscopy along the $\bar{\Gamma}\bar{\mathrm{K}}$ direction of the surface Brillouin zone [152]. The similarity with the phonon dispersion of graphite has been interpreted in terms of a weak graphene–Pt interaction.

Here, the dispersion of all acoustic and optical phonons of graphene on Ir(111) along high symmetry directions of the surface Brillouin zone is determined using angle-resolved inelastic electron scattering. The experimental data are in very good agreement with accompanying density functional calculations.

Experiment and Theory

The experiments were performed in ultrahigh vacuum with a base pressure of 10^{-9} Pa. The single-crystalline Ir(111) surface was cleaned by repeated cycles of Ar^+ bombardment and annealing at 1200 K. Graphene was grown by thermal decomposition of C_2H_4. Exposure of clean Ir(111) to C_2H_4 (purity 99.9 %, 5×10^{-4} Pa, 120 s) at 1500 K leads to a single layer of highly ordered and singly oriented graphene as revealed by low-energy electron diffraction [108]. Angle-resolved electron energy loss spectra were measured at room temperature using an Ibach spectrometer [127]. To check the cleanliness of the prepared surfaces, specular electron energy loss spectra were acquired with impact electron energies ranging between 6 and 11 eV. In specular scattering geometries the incident monochromatic electron beam enclosed an angle of 64° with the surface normal. The energy resolution of the spectrometer was set to 2.5 meV. Dispersion curves of graphene on Ir(111) were determined in off-specular scattering geometries with impact electron energies in the range of 111 to 192 eV. The transfer of high electron momentum

parallel to the surface was achieved by increasing the angle of the incident electron beam with respect to the surface normal to 74–78°. Parallel wave vectors were determined with an accuracy below 0.05 Å^{-1}. In some off-specular measurements the energy resolution was set to 4 meV to increase the current at the detector. Depending on the signal-to-noise ratio dwell times up to 1 s per data point were used. The presented data are averages over 50 to 250 individual spectra. STM experiments were performed at 78 K. STM images were recorded in the constant-current mode with the bias voltage applied to the sample.

The phonon dispersion relations of graphene on Ir(111) were calculated using density functional perturbation theory [153–155] with the local density approximation (LDA) to the exchange-correlation functional.[1] A periodic unit cell containing three layers of Ir with the graphene honeycomb center located above face-centered cubic Ir(111) sites[2] on both sides of the slab was used [149]. The vacuum distance between graphene layers of neighboring supercells[3] was 6 Å. The lattice constant of Ir(111) was adapted to the experimentally determined lattice constant of graphene on Ir(111) (2.452 Å, Ref. 31) in order to avoid a large moiré supercell, which would render the *ab initio* calculations of phonons unfeasible. Troullier-Martins pseudopotentials were used with an energy cut-off of 30 Ha. The first Brillouin zone is sampled by a $12 \times 12 \times 1$ **k**-point grid. Geometry optimization under these conditions leads to a graphene–Ir distance of 3.64 Å, which is in reasonable agreement with the experimental value of 3.38 Å [27]. The resulting graphene buckling is less than 0.002 Å. In the dynamical matrix the Ir atoms were assigned a large mass to obtain Ir phonon energies close to zero, which facilitates their discrimination from graphene phonons.

Results and Discussion

Figure 2.1(a) shows a specular electron energy loss spectrum of graphene on Ir(111) acquired with an impact electron energy of 11 eV. The absence of energy loss features in the wide energy range demonstrates the cleanliness of the prepared graphene layer. The peak at zero energy reflects elastically scattered electrons. It is surrounded by features at −7 and 7 meV [inset to Fig. 2.1(a)] which are the spectroscopic signatures of the out-of-plane acoustic (ZA) graphene phonon at the $\bar{\Gamma}$ point of the surface Brillouin zone. In

[1] Local functionals neglect van der Waals forces. However, the LDA to the exchange functional gives reasonable results for the geometry and for the energies of interlayer phonon modes [149].

[2] Calculations with the graphene honeycomb center residing at hexagonal close-packed and on-top Ir(111) sites lead to essentially identical results.

[3] Graphene remains flat in the sandwich configuration. This configuration is different from a previous report, where the presence of Ir nano-islands on one side of the graphene layer leads to a strong corrugation of graphene [156].

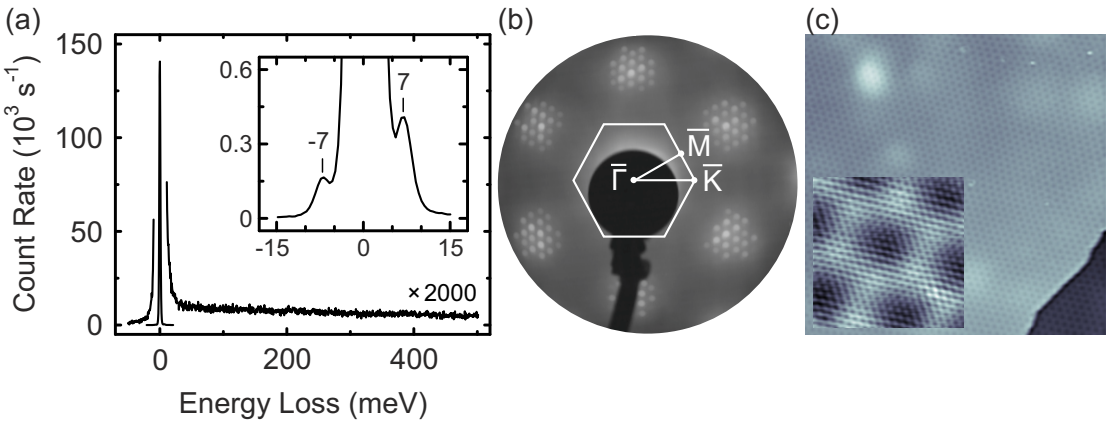

Fig. 2.1: (a) Specular electron energy loss spectrum of graphene on Ir(111) acquired with an impact electron energy of 11 eV. The peak at zero energy reflects elastically scattered electrons. Inset: Close-up view around zero energy. The peak at −7 meV (7 meV) is due to the energy gain (loss) of electrons scattered from ZA graphene phonons. **(b)** Low-energy electron diffraction pattern of graphene-covered Ir(111) recorded with a kinetic energy of incident electrons of 147 eV. The surface Brillouin zone with high symmetry points is indicated. The diffraction spots are due to Ir(111) and the long-range moiré pattern of graphene. **(c)** Constant-current STM image of single-layer graphene on Ir(111) acquired at 78 K (20 nA, 0.1 V, $100 \times 100\,\mathrm{nm}^2$). The gray scale ranges from 0 (black) to 500 pm (white). Inset: Atomically resolved STM image showing the moiré-induced superstructure (20 nA, 0.1 V, $5 \times 5\,\mathrm{nm}^2$). The gray scale ranges from 0 (black) to 30 pm (white). Both STM images were processed with WSxM [157].

addition, specular spectra of graphene on Ir(111) remain virtually unchanged even after several days of data acquisition, which confirms the previously reported chemical inertness of the graphene film [158]. Low-energy electron diffraction patterns [Fig. 2.1(b)] prove the crystalline quality of the graphene layer. An extended hexagonal array of satellite spots, which surrounds each Ir(111) diffraction spot is due to the moiré superlattice [108]. The absence of additional diffraction spots in the indicated $\bar{\Gamma}\bar{K}$ directions shows that densely packed graphene $\langle 11\bar{2}0\rangle$ orientations are aligned with crystallographic $\langle 1\bar{1}0\rangle$ directions of Ir(111) [50]. The representative STM image in Fig. 2.1(c) shows the atomic cleanliness and the single orientation of the graphene film.

Based on the structural homogeneity, the phonon dispersion relation of graphene on Ir(111) can be determined with high precision. Figure 2.2(a) shows the experimental (dots) and calculated (dashed lines) phonon dispersion.[4] Dispersion branches of the out-of-plane acoustic (ZA), out-of-plane optical (ZO), transverse acoustic (TA), longitudinal acoustic (LA), transverse optical (TO), and longitudinal optical (LO) phonons are indicated. Each data point of the measured phonon dispersion has been extracted from

[4] For clarity we initially do not show graphene phonon branches that are related to the moiré superstructure, nor do we include the dispersion curves of Ir(111). Moiré-induced replica of graphene phonons are discussed in detail in Section 2.3.

individual off-specular vibration spectra, an example of which is shown in Fig. 2.2(b) for a wave vector transfer of $q_{\parallel} = 0.6\,\text{Å}^{-1}$ along the $\bar{\Gamma}\bar{\text{M}}$ direction. Experimental and calculated phonon dispersion relation curves are in excellent agreement. Moreover, the dispersion curves are very similar to the dispersion curves of pristine graphene [159, 160] and graphite [159–162], which confirms the reported weak graphene–Ir interaction [29]. However, some deviations occur which are presented and discussed in the following sections. Examining these deviations more closely enables new insights into the graphene–substrate interaction.

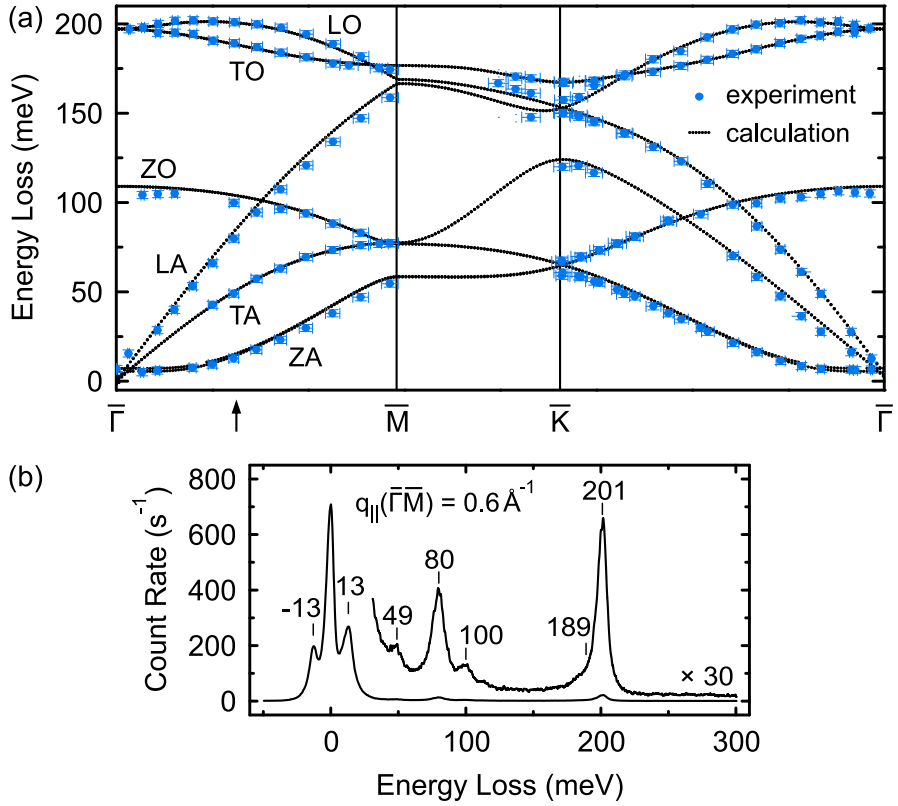

Fig. 2.2: (a) Phonon dispersion of graphene on Ir(111). Dispersion branches of the out-of-plane acoustic (ZA), out-of-plane optical (ZO), transverse acoustic (TA), longitudinal acoustic (LA), transverse optical (TO), and longitudinal optical (LO) phonons are indicated. Experimental (calculated) data appear as blue dots (black dotted lines). The distances between the high symmetry points of the surface Brillouin zone of graphene ($\bar{\Gamma}$, $\bar{\text{M}}$, $\bar{\text{K}}$) are $\bar{\Gamma}\bar{\text{M}} = 2\pi/(\sqrt{3}a) = 1.48\,\text{Å}^{-1}$ and $\bar{\Gamma}\bar{\text{K}} = 4\pi/(3a) = 1.71\,\text{Å}^{-1}$ with $a = 2.452\,\text{Å}$ the lattice constant of graphene on Ir(111). The arrow indicates the parallel wave vector at which the spectrum in (b) was acquired. **(b)** Off-specular electron energy loss spectrum acquired with an impact electron energy of 111 eV and a wave vector transfer of $0.6\,\text{Å}^{-1}$ along the $\bar{\Gamma}\bar{\text{M}}$ direction. Loss features at 13, 49, 80, 100, 189, 201 meV are due to electron scattering from ZA, TA, LA, ZO, TO, LO phonons, respectively. The peak at −13 meV reflects the energy gain of electrons scattered from ZA phonons.

2.2 Screening of Electron-Phonon Coupling

The first deviation to be discussed concerns the Kohn anomalies of the highest optical phonon branches. The Kohn anomaly [163] is one of the key signatures of electron-phonon coupling, which has been reported for a variety of examples [102, 164, 165]. It describes the softening of phonons with wave vectors that coincide with $\mathbf{k}_1 - \mathbf{k}_2 \pm \mathbf{g}$ where $\mathbf{k}_1$, $\mathbf{k}_2$ are wave vectors of electrons at the Fermi level and $\mathbf{g}$ denotes a reciprocal lattice vector. The Fermi surface of pristine graphene consists of two equivalent points at $\bar{\mathrm{K}}$ and $\bar{\mathrm{K}}'$, which reflect the apexes of the Dirac cones. Thus, Kohn anomalies are expected at $\bar{\Gamma}$ and $\bar{\mathrm{K}}$ [166]. Indeed, inelastic X-ray data obtained from the highest optical phonon branches of graphite [161] have been interpreted in terms of the Kohn anomaly [150]. Indications of Kohn anomalies of graphene on Pt(111) have recently been provided [167].

Here, we show that investigations into the dynamics of graphene on a metal surface reveal subtle aspects of electron-phonon coupling, electron correlations, and the graphene–metal interaction. As the main finding we report the weakened Kohn anomaly of the highest optical phonon branch around $\bar{\mathrm{K}}$. This observation is rationalized in terms of a reduced electron-phonon interaction due to screening of electron correlations in graphene by the metal electron gas.

Results and Discussion

Figure 2.3 shows a close-up view of the dispersion relations of the LO phonon around $\bar{\Gamma}$ [Fig. 2.3(a)] and of the TO phonon around $\bar{\mathrm{K}}$ [Fig. 2.3(b)], both depicted as dots. Calculations for graphene on Ir(111) appear as black dashed lines. For comparison, inelastic X-ray scattering data of graphite around $\bar{\Gamma}$ [161] and around $\bar{\mathrm{K}}$ [162] are shown as squares. Calculated dispersion curves [160] for pristine graphene and graphite have been added as gray and light gray dashed lines, respectively. Around $\bar{\Gamma}$ [Fig. 2.3(a)] all data sets exhibit good agreement. In particular, the experimental dispersion of the LO phonon can be very well reproduced by LDA density functional calculations, which neglect the long-range character of the electron-electron interaction. Consequently, for the LO phonon of graphene on Ir(111) correlation effects play a minor role, which is in line with observations from the LO phonon of pristine graphene and graphite [160]. The calculations reveal that the LO dispersion curve around $\bar{\Gamma}$ (black dashed line) exhibits a parabolic minimum rather than a kink, which is expected for pristine graphene (gray dashed line). The shift of the Fermi level due to p-doped graphene [29] and the temperature-induced broadening of the Fermi-Dirac distribution function are the reasons for this observation. Apart from these minor deviations, we conclude that the Kohn anomaly of the highest optical phonon branch at $\bar{\Gamma}$ persists in graphene on Ir(111).

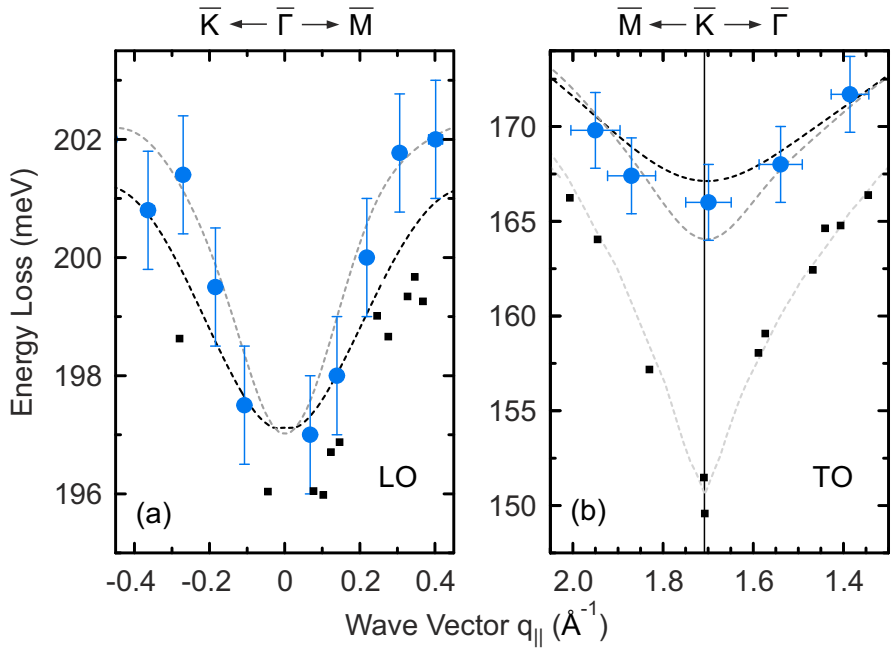

Fig. 2.3: Dispersion of **(a)** the LO phonon in the vicinity of $\bar{\Gamma}$ and of **(b)** the TO phonon close to $\bar{\mathrm{K}}$. Dots represent our data for graphene on Ir(111), squares are inelastic X-ray data obtained from graphite around $\bar{\Gamma}$ [161] and around $\bar{\mathrm{K}}$ [162], black (gray) dashed lines show LDA density functional calculations for graphene on Ir(111) (pristine graphene), and the light gray dashed line in (b) represents *GW* calculations for graphite[162]. The vertical line in (b) indicates the boundary of the surface Brillouin zone at $\bar{\mathrm{K}}$.

The situation is markedly different for the TO phonon dispersion close to $\bar{\mathrm{K}}$ [Fig. 2.3(b)]. Compared with inelastic X-ray data (squares) and *GW* calculations for graphite (light gray dashed line) the indentation of the TO dispersion of graphene on Ir(111) is less pronounced. For instance, the TO phonon energy at $\bar{\mathrm{K}}$ is $\approx 16\,\mathrm{meV}$ ($129\,\mathrm{cm}^{-1}$) higher than observed for graphite. A hint to the driving mechanism is given by the good agreement between the experimental dispersion data and LDA calculations (black dashed line). In contrast, for graphite density functional theory within the LDA failed in describing the dispersion of the highest optical phonon branch at $\bar{\mathrm{K}}$ [160, 162]. Rather, *GW* calculations that take electron correlations explicitly into account were required to adequately model experimental data. Therefore, it appears that correlation effects for the TO phonon of graphene on Ir(111) are less important than observed for pristine graphene and graphite. Electron correlations in graphene may be reduced by the screening of the Ir(111) electronic system.

To corroborate this scenario the coupling between TO phonons and π electrons is analyzed for pristine graphene and for graphene on Ir(111). The electron-phonon coupling may be obtained from $\langle D^2 \rangle = \Delta E^2/(8d^2)$ where ΔE describes the gap of π bands that

Tab. 2.1: Band gap (ΔE) and electron-phonon coupling ($\langle D^2 \rangle$) for the graphene TO phonon at $\bar{\mathrm{K}}$. Calculations were performed for pristine graphene and graphene on Ir(111). The displacement of C atoms is $d = 0.53\,\mathrm{pm}$. Results from LDA and GW calculations are compared.

		pristine graphene	graphene on Ir(111)
ΔE (eV)	LDA	0.142	0.142
	GW	0.2158	0.1747
$\langle D^2 \rangle$ (eV^2/Å^2)	LDA	90.11	90.11
	GW	207.88	131.75

arises due to the displacement d of C atoms according to the TO phonon pattern at $\bar{\mathrm{K}}$ [160]. Results for ΔE and $\langle D^2 \rangle$ which were obtained from density functional and GW calculations[5] are summarized in Table 2.1. While density functional calculations give the same results for pristine graphene and graphene on Ir(111), the GW calculations yield an electron-phonon coupling for graphene on Ir(111) that is $\approx 37\,\%$ lower than the value obtained for pristine graphene. This effect is preponderantly due to the screening of electron correlations in graphene by the metal substrate. The calculations even underestimate the screening effect since metal intraband contributions to the dielectric function are missing [169]. To a lesser extent charge transfer between graphene and Ir(111) may be responsible for the reduction of the electron-phonon coupling [170]. As a result, the metallic substrate reduces the electron-phonon coupling by screening of electron correlations. In the case of isolated graphene and graphite, correlation effects are responsible for a strong Kohn anomaly at $\bar{\mathrm{K}}$. Thus, screening of correlation effects by the metallic substrate leads to a reduction of the Kohn anomaly compared to the cases of isolated graphene and graphite. These observations are in stark contrast to findings reported from graphene on Ni(111) [171, 172], where the strong hybridization between graphene π bands and Ni d bands causes a destruction of the linear crossing of the π and π^* bands at the Fermi level, which in turn leads to the elimination of both graphene Kohn anomalies [149]. For graphene on Ir(111), however, the Dirac cones remain essentially intact [29] and both Kohn anomalies persist. The weakening of the $\bar{\mathrm{K}}$ point Kohn anomaly, however, has not been expected and requires the aforementioned screening mechanism.

[5] In order to render the calculations feasible, the equivalence of the two C atoms in the graphene unit cell is ensured by attaching three layers of Ir in the face-centered cubic stacking to each side of the graphene sheet. The GW calculations were performed with YAMBO [168] using a $18 \times 18 \times 1$ **k**-point grid.

2.3 Moiré-Induced Phonon Replica

The second deviation to be discussed concerns the influence of the moiré superstructure on the phonon dispersion relation. On, *e. g.*, Ni(111) and Co(0001) the mismatch between graphene and surface lattice constants is less than 2 %, which leads to commensurate graphene superstructures [173, 174]. In contrast, graphene on, *e. g.*, Ir(111) [31], Pt(111) [49], and Ru(0001) [48] exhibits a lattice mismatch on the order of 10 %. As a consequence, a moiré superlattice is formed whose periodicity depends on the lattice mismatch and on the rotation angle enclosed by crystallographic directions of graphene and of the substrate surface. The moiré superstructure has been demonstrated to act as a template for the growth of metal nanoclusters [175, 176] and two-dimensional molecular networks [95, 177]. Moreover, the moiré pattern represents an electronic superlattice, *i. e.*, graphene electrons are subject to an additional potential that exhibits the periodicity of the moiré superstructure. Consequently, replica of the Dirac cone and energy gaps at the intersection between these replica and the Dirac cone evolve [29, 178]. Furthermore, a highly anisotropic mobility and density of charge carriers have been predicted as a result of the moiré-induced potential [51].

In this section we show that the moiré pattern of graphene on Ir(111) induces replica of graphene phonon branches, which can be clearly observed throughout the surface Brillouin zone. Using a linear chain of C atoms coupled to a rigid substrate shows that phonon replica occur when a periodic variation of C–C and C–substrate interactions is imposed.

Results and Discussion

The moiré superstructure leaves its fingerprints in the phonon dispersion of graphene on Ir(111), as shown in Fig. 2.4 for the ZA and ZO phonon branch along the $\bar{\Gamma}\bar{\mathrm{K}}$ [Fig. 2.4(a)] and $\bar{\Gamma}\bar{\mathrm{M}}$ [Fig. 2.4(b)] directions of the surface Brillouin zone. In addition to the dispersion curves of the ZA and ZO phonons (blue dots) replica of these curves (gray dots) appear at lower and higher wave vectors. A typical off-specular spectrum that leads to dispersion data at a specific wave vector is depicted in Fig. 2.4(c). The peaks at ≈ 47 meV and ≈ 81 meV are spectroscopic signatures of ZA and ZO phonons, respectively [180]. According to the shifted dispersion curves [Fig. 2.4(a)] peaks at 20, 34, 57 meV are assigned to replica of ZA phonons with wave vectors $q_{\parallel} - g_{\mathrm{K}}$, $q_{\parallel} + g_{\mathrm{K}}$, $q_{\parallel} + 2\,g_{\mathrm{K}}$, respectively. Peaks at 71 and 90 meV are attributed to replica of ZO phonons with wave vectors $q_{\parallel} - g_{\mathrm{K}}$ and $q_{\parallel} + g_{\mathrm{K}}$. Similar arguments hold for the $\bar{\Gamma}\bar{\mathrm{M}}$ direction [Fig. 2.4(b)], where replica phonon bands are obtained by shifting the ZA, ZO phonon dispersion curves by $\pm g_{\mathrm{M}}$ and $2\,g_{\mathrm{M}}$. Here, g_{K} and g_{M} represent the projections of a moiré

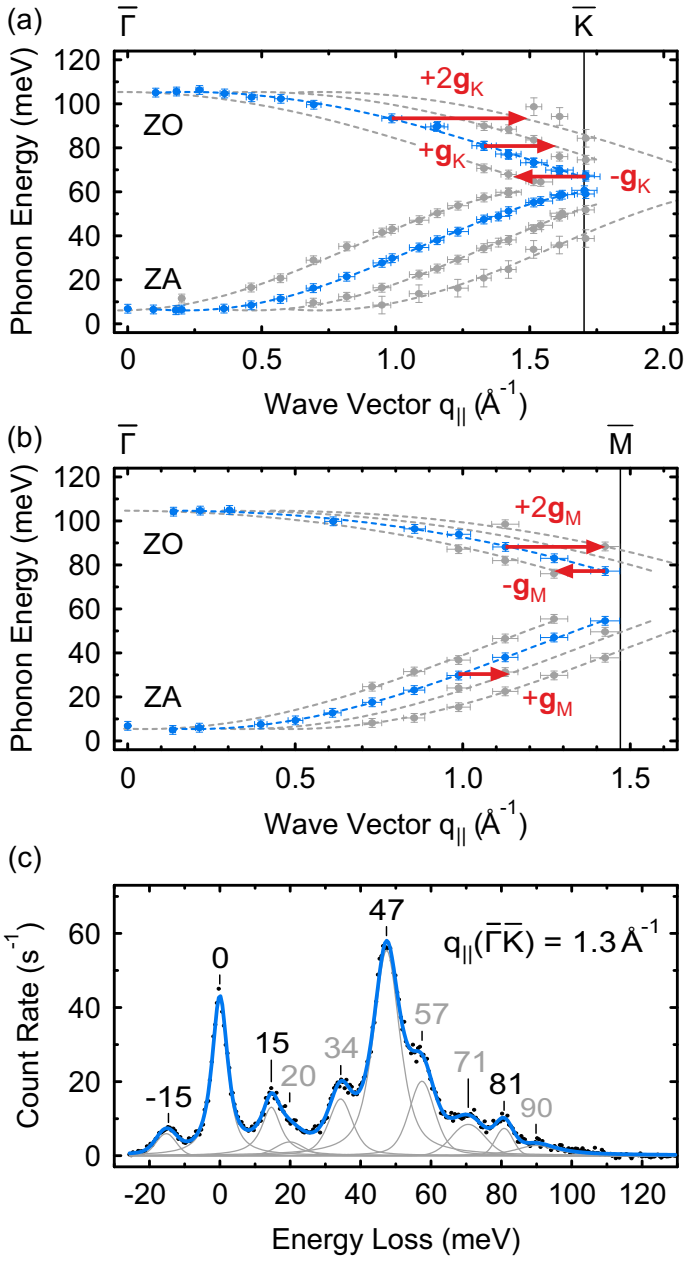

Fig. 2.4: Dispersion of graphene ZA and ZO phonons (blue dots) on Ir(111) along **(a)** $\bar{\Gamma}\bar{\mathrm{K}}$ and **(b)** $\bar{\Gamma}\bar{\mathrm{M}}$. Replica of dispersion data appear as gray dots. Dashed lines are guides to the eye. The replica are obtained by shifting the ZA and ZO branches by $\pm g_{\mathrm{K}}$, $2\,g_{\mathrm{K}}$ in (a) and by $\pm g_{\mathrm{M}}$, $2\,g_{\mathrm{M}}$ in (b). g_{K}, g_{M} represent the projections of the moiré reciprocal lattice vector onto $\bar{\Gamma}\bar{\mathrm{K}}$, $\bar{\Gamma}\bar{\mathrm{M}}$ [Fig. 2.5(a)]. **(c)** Off-specular electron energy loss spectrum obtained with a primary energy of impinging electrons of 192 eV and a parallel wave vector transfer of $q_{\parallel} = 1.3\,\text{Å}^{-1}$ along $\bar{\Gamma}\bar{\mathrm{K}}$. Electron energy losses of 47, 81 meV are due to scattering from ZA and ZO phonons. Maxima at 20, 34, 57 meV (71, 90 meV) indicate energy losses due to electron scattering from replicated ZA (ZO) phonons. Peaks at −15, 15 meV reflect the energy gain, loss of electrons scattered from acoustic Ir(111) surface phonons [179].

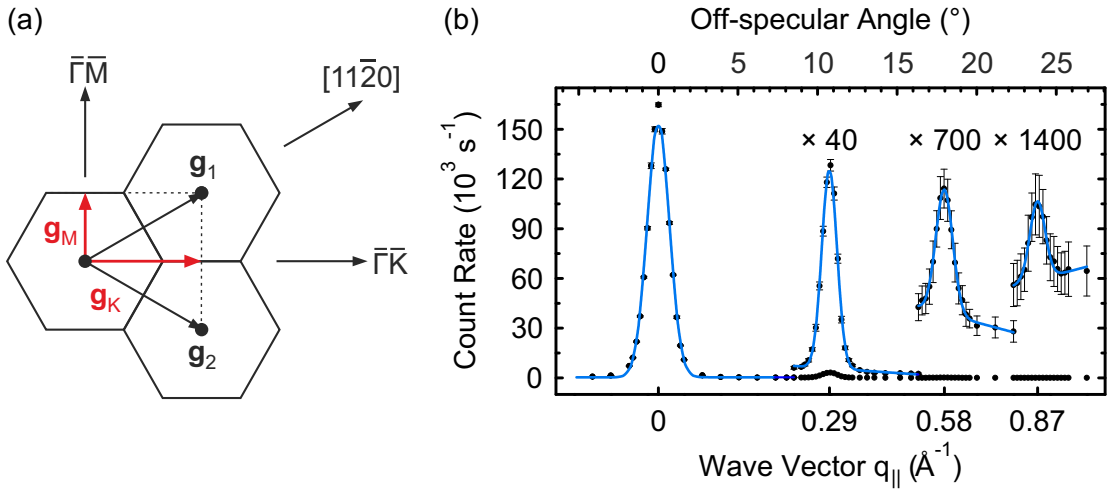

Fig. 2.5: (a) Moiré-induced surface Brillouin zones spanned by $\mathbf{g}_1$, $\mathbf{g}_2$ with magnitude $|\mathbf{g}_1| = |\mathbf{g}_2| = g = 4\pi/(\sqrt{3}a)$ (a: spatial periodicity of the graphene moiré superlattice along $\langle 11\bar{2}0\rangle$). The projections (red arrows) of $\mathbf{g}_1$ onto $\bar{\Gamma}\bar{K}$ and $\bar{\Gamma}\bar{M}$ directions are $g_K = 2\pi/a$ and $g_M = 2\pi/(\sqrt{3}a)$, respectively. **(b)** Evolution of the intensity of the diffuse elastic peak with the off-specular angle. The off-specular angle is referred to the angle of specular electron reflection (0°). The sagittal plane was oriented along the $\bar{\Gamma}\bar{M}$ direction. Intensity maxima occur at Bragg angles that were converted into parallel wave vectors.

reciprocal lattice vector onto the $\bar{\Gamma}\bar{K}$ and $\bar{\Gamma}\bar{M}$ directions of the surface Brillouin zone, respectively [Fig. 2.5(a)]. The moiré lattice exhibits a spatial periodicity of $a = 25.3\,\text{Å}$ along $\langle 11\bar{2}0\rangle$ graphene directions [31], which implies a reciprocal lattice vector with magnitude $g = 4\pi/(\sqrt{3}a) \approx 0.29\,\text{Å}^{-1}$. The projection of this reciprocal vector onto the $\bar{\Gamma}\bar{K}$ and $\bar{\Gamma}\bar{M}$ direction [Fig. 2.5(a)] is $g_K = \sqrt{3}g/2 \approx 0.25\,\text{Å}^{-1}$ and $g_M = g/2 \approx 0.14\,\text{Å}^{-1}$, respectively. This periodicity is reflected by the intensity evolution of the diffuse elastic peak with the off-specular angle [Fig. 2.5(b)]. The sagittal plane was oriented along the $\bar{\Gamma}\bar{M}$ direction and intensity maxima occur at integer multiples of g, which are due to Bragg-reflected electrons.

Replica of dispersion curves have also been observed for the LA and the LO phonons, as shown in Fig. 2.6. However, for the highest optical branches it was more difficult to discern replica. This difficulty may be explained by the weak dispersion and the similar energies of transverse optical (TO) and LO phonons throughout the surface Brillouin zone [180].

To capture the basic physics of the out-of-plane phonon replica and their intensity in electron energy loss spectra the dispersion of a transverse acoustic phonon has been calculated for an infinitely long linear chain of C atoms which is coupled to an infinitely heavy substrate by adapting the semi-empirical model of Aizawa *et al.* [181]. Here, an angle-bending spring constant γ tries to maintain the 180° C–C bond angle [inset to

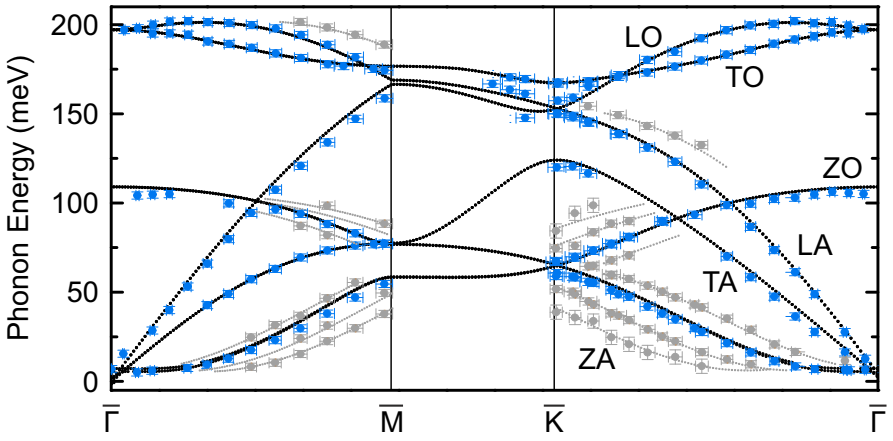

Fig. 2.6: Dispersion of graphene ZA, LA, TA, ZO, TO, and LO phonons (blue dots) on Ir(111). Black dots represent calculated data. Replica of dispersion data appear as gray dots. Gray dashed lines are guides to the eye. The replica in $\bar{\Gamma}\bar{\mathrm{M}}$ and $\bar{\Gamma}\bar{\mathrm{K}}$ direction are obtained by shifting the corresponding phonon branches by $\pm g_{\mathrm{M}}$, $2\,g_{\mathrm{M}}$ and by $\pm g_{\mathrm{K}}$, $2\,g_{\mathrm{K}}$, respectively.

Fig. 2.7(a)]. From γ one obtains the nearest (1) and next-nearest (2) neighbor force constants $C_1 = 4\gamma/a^2$ and $C_2 = -\gamma/a^2$ (a: C–C equilibrium distance). In addition, a spring constant α simulates the coupling to the substrate [inset to Fig. 2.7(a)]. By assuming one C atom per primitive unit cell, the dispersion relation for the transverse acoustic phonon[6] results as

$$\omega(q) = \sqrt{\frac{4\gamma}{ma^2}[1-\cos(qa)]^2 + \frac{\alpha}{m}} \tag{2.1}$$

with m the mass of a C atom. The corresponding dispersion curve appears as a full line in Fig. 2.7(a). In accordance with previous publications the chain–substrate interaction leads to a finite phonon energy at $q = 0$, *i. e.*, $E_1 = \hbar\sqrt{\alpha/m}$ [180, 181].

We have extended the one-dimensional model to account for the moiré superstructure. To this end modulations of α and γ with the spatial periodicity of Na ($N = 10$), *i. e.*, $\alpha_n = \alpha + \Delta\alpha\cos^2(n\pi/N)$ and $\gamma_n = \gamma + \Delta\gamma\cos^2(n\pi/N)$, have been introduced. The resulting $N \times N$ dynamical matrix[7] has been diagonalized numerically. The spatial modulation of α and γ is motivated by the previously reported impact of the graphene moiré pattern on C–C as well as C–Ir chemical bonds [27]. We assume that the regions of lower bonding distance (moiré valleys) lead to a locally enhanced value of α. Similarly, charge transfer from the substrate to graphene is not isotropic. Rather, charge accumulates in the moiré valleys and therefore leads to a local decrease of the spring

[6] For a detailed derivation, please refer to Appendix C, Section C.1.
[7] The dynamical matrix is specified in Appendix C, Section C.2.

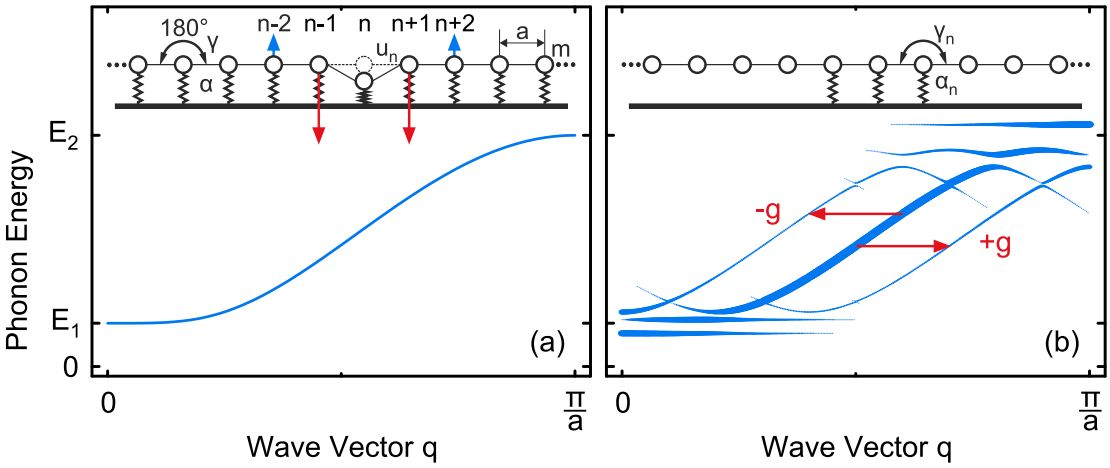

Fig. 2.7: (a) Dispersion of the transverse acoustic phonon [Eq. (2.1)] of a supported linear chain of C atoms (full line). At $q = 0$ ($q = \pi/a$) the phonon energy is $E_1 = \hbar\sqrt{\alpha/m}$ ($E_2 = \hbar\sqrt{16\gamma/(ma^2) + \alpha/m}$). Inset: Sketch of the one-dimensional chain of C atoms with mass m and equilibrium mutual distance a. The coupling of C atoms to the infinitely heavy substrate is modeled by springs with uniform spring constants α. The angular spring constant γ tries to maintain a 180° bond angle. The displacement u_n of atom n induces displacements of nearest and next-nearest neighbors as indicated by the vertical arrows. **(b)** Like (a) with periodically varying spring constants $\alpha_n = \alpha_{n+N}$ and $\gamma_n = \gamma_{n+N}$ ($N = 10$). Replica (thin lines) of the original dispersion curve (thick line) appear due to the additional superlattice. With respect to the original dispersion curve they are shifted by $\pm j \cdot g$ [$j \in \mathbb{N}$, $g = 2\pi/(Na)$], which reflects the magnitude of a reciprocal superlattice vector. The line thickness describes the absolute value of the projection $\langle u'(q)|u(q)\rangle$ divided by $\sqrt{N}$. Inset: Sketch of the supported one-dimensional chain of C atoms with site-dependent spring constants α_n and γ_n.

constant γ. The absolute values of α and γ have been chosen such as to render the phonon replica visible.[8] As a measure for the visibility we use the absolute value of the projection $\langle u'(q)|u(q)\rangle$. Here, $|u(q)\rangle = |(u_1(q), \ldots, u_N(q)\rangle$ describes the displacement of each atom in the linear chain without a superstructure, *i. e.*, $u_n(q) = u_0 \exp(inqa)$ ($1 \le n \le N$). The vector $|u'(q)\rangle$ comprises numerically calculated displacements of atoms in the linear chain with a superstructure. For $\Delta\alpha = 0$ and $\Delta\gamma = 0$ it reads $u'_n(q) = u_0 \exp[in(q+j\cdot g)a]$ ($1 \le j \le N$), with $g = 2\pi/(Na)$ the magnitude of a reciprocal superlattice vector. The projection may then be cast to $\langle u'(q)|u(q)\rangle = |u_0|^2 \sum_{n=1}^{N} \exp(2\pi inj/N)$, which vanishes unless j is an integer multiple of N, *i. e.*, g is the magnitude of a reciprocal lattice vector. This observation is in accordance with the absence of phonon replica in Fig. 2.7(a). In comparison, Fig. 2.7(b) shows the dispersion curves resulting from the extended model

[8] In principle, $\Delta\alpha$ and $\Delta\gamma$ may be determined from *ab initio* calculations of phonons in the moiré supercell. However, this requires the reliable inclusion of van der Waals forces and seems, at present, out of reach for phonon calculations in large supercells. For the current model the following dimensionless parameters were used: $m = 1$, $a = 2.4$, $\gamma = 0.25$, $\Delta\gamma = 0.5$, $\alpha = 0.045$, $\Delta\alpha = 0.01$.

with modulations of α and γ. While the original dispersion curve of the transverse acoustic phonon exhibits the largest projection, the replica at $q \pm g$ attain a finite albeit weak value of the projection. Replica at $q \pm j \cdot g$ ($j > 1$) exhibit a virtually vanishing projection.

While our simple model describes the experimental observation of phonon replica [Figs. 2.4(a),(b)] and their reduced intensity in energy loss spectra [Fig. 2.4(c)] it contains some features that deviate from experimental findings. The actual intensity ratio of spectroscopic signatures of the phonon and its replica [Fig. 2.4(c)] has not been reproduced by the model. Since the calculations do not consider the efficiency of electron scattering from phonons we cannot expect that the projection $\langle u'(q)|u(q)\rangle$ alone will adequately describe the intensity ratio. Indeed, to obtain sufficiently large values of the projection rather large values of α and γ had to be chosen. As a consequence, the phonon energy at $q = 0$ shifts to a value E_1 [Figs. 2.7(a),(b)] that is larger than the experimental energy and dispersionless branches close to $q = 0$ and in the vicinity of $q = \pi/a$ occur. With increasing values of the corrugation parameters $\Delta\alpha$ and $\Delta\gamma$ the number of these branches increases and the central dispersive energy region shrinks. The presence of the dispersionless branches is an artifact of the simplified model and calls for a future refinement. However, our model shows that by introducing a periodic modulation of force constants phonon replica occur at wave vectors that reflect the periodicity of the supercell. In addition, the spectroscopic weight of replicated phonons depends on the actual size of the modulation amplitude.

2.4 Graphene–Iridium Interaction

The third deviation to be discussed concerns the dispersion of ZA, ZO, LA, LO graphene phonons in specific regions of the surface Brillouin zone. The dispersion of these phonons deviates from the corresponding dispersion of pristine graphene. First, the deviations around the $\bar{\Gamma}$ point of the surface Brillouin zone will be addressed and, subsequently, those around the $\bar{\mathrm{K}}$ point.

Close to and at $\bar{\Gamma}$ the ZA phonon of graphene on Ir(111) exhibits non-zero energy [dots in Fig. 2.8(a)]. Density functional calculations with the local density approximation (upper black dashed line) and the general gradient approximation (lower black dashed line) to the exchange-correlation functional reproduce this behavior. Our observations are in clear contrast to the ZA phonon dispersion of pristine graphene [159] [gray dashed line in Fig. 2.8(a)] and of graphite [182], which both show zero energy at zero wave vector. At $\bar{\Gamma}$ the ZA phonon energy of graphene on Ir(111) is $\approx 7\,\mathrm{meV}$ [inset to Fig. 2.1(a)]. In a simple harmonic oscillator model for the C vibrations [181] the observed ZA phonon

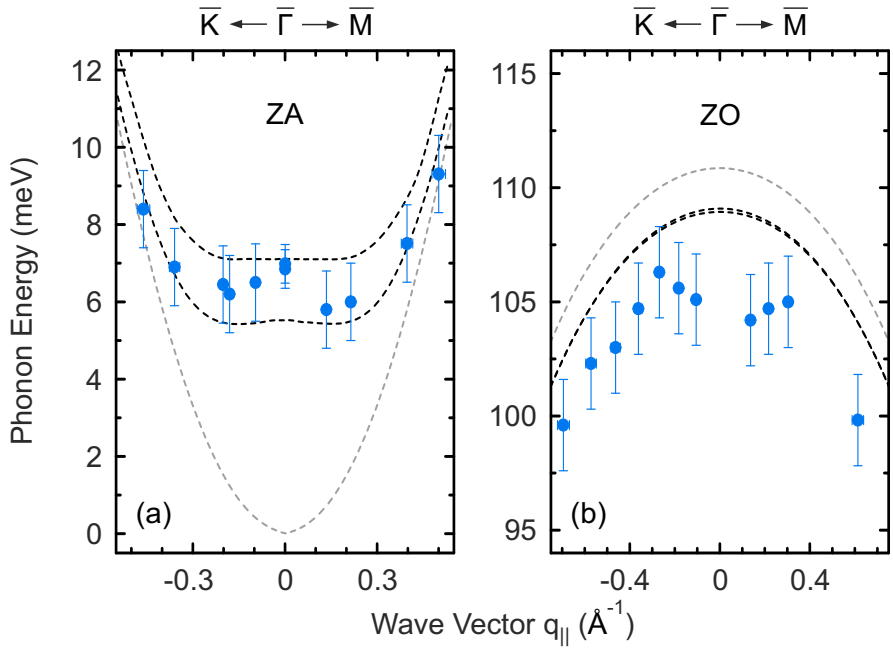

Fig. 2.8: Experimental dispersion data (dots) of **(a)** the ZA and **(b)** the ZO phonon of graphene on Ir(111) around the $\bar{\Gamma}$ point of the surface Brillouin zone. Black dashed lines represent results of density functional calculations with the local density approximation [upper curve in (a)] and the general gradient approximation [lower curve in (a)] to the exchange-correlation functional. In (b) both approximations nearly coincide. The gray dashed line depicts calculated data for pristine graphene [159].

energy can be translated into a spring constant, $m\omega^2 \approx 2.2\,\mathrm{Nm}^{-1}$, with m the mass of a C atom and ω the angular frequency of the ZA phonon at $\bar{\Gamma}$. The spring constant serves as a rough estimate of the interaction between graphene and the metal surface. It is about a factor 18 lower than the one obtained for graphene on Ni(111) [149] and about a factor 4 lower than the spring constant for the interlayer coupling in graphite [159]. Therefore, the dynamical properties of graphene on Ir(111) support a weak but finite graphene–Ir interaction, which is in agreement with previous photoemission investigations into the electronic structure of graphene on Ir(111) [27].

Upon graphene adsorption to Ir(111) the ZO phonon dispersion of pristine graphene [gray dashed line in Fig. 2.8(b)] is likewise affected around $\bar{\Gamma}$. As shown in Fig. 2.8(b) the experimentally obtained ZO phonon dispersion (dots) is lower than the corresponding dispersion of pristine graphene. It is also lower than the calculated dispersion curves for graphene adsorbed on Ir(111), which appear as black dashed lines in Fig. 2.8(b). The downshift of the ZO branch around $\bar{\Gamma}$ may likewise be explained by the interaction between graphene and Ir. In addition to physisorption over the entire interface, density functional calculations show a weak hybridization of graphene p_z orbitals with Ir d

orbitals at C atoms residing on top of Ir atoms [27]. Due to this hybridization, charge is transferred from nearest-neighbor C atoms to Ir [27], which causes a reduced overlap of p_z orbitals, *i. e.*, π bonds between adjacent C atoms are weakened [181]. Around $\bar{\Gamma}$, the ZO displacement pattern consists of antiparallel oscillations of nearest-neighbor C atoms perpendicular to the basal plane of graphene [182]. Since these oscillations involve the weakened π bonds between adjacent C atoms a lowering of the ZO phonon energy at $\bar{\Gamma}$ with respect to pristine graphene is expected and observed experimentally [Fig. 2.8(b)]. These results are compatible with observations from graphene on Ni(111) where a charge transfer of 0.21 e per C atom [183] leads to a softening of the ZO phonon at $\bar{\Gamma}$ by ≈ 23 meV [171, 172]. In the case of graphene on Ir(111) a charge transfer of 0.01 e [27] leads to a reduction of the ZO phonon energy of ≈ 5 meV, which is comparable to the energy downshift observed from graphite [182]. Our interpretation may also explain the observation that the experimental data are lower than calculated values since in the density functional calculations graphene was assumed to be commensurate with the Ir(111) lattice. The calculations, therefore, do not consider the moiré superstructure and the concomitant spatial variation of C–Ir couplings.

Furthermore, the experimental data of the ZO branch close to $\bar{\Gamma}$ [blue dots in Fig. 2.8(b)] deviate from a nearly parabolic dispersion curve. The indentation of the ZO dispersion close to $\bar{\Gamma}$ could be a possible hint to a further Kohn anomaly, *i. e.*, a coupling between π electrons and ZO phonons. Recently, such a ZO Kohn anomaly has been demonstrated for graphene on Pt(111) [184]. For graphene on Ir(111), the apexes of the Dirac cones are shifted by $\Delta E \approx 0.10$ eV from the Fermi energy [29]. Therefore, a ZO Kohn anomaly could be observed at parallel wave vectors of $q_{\parallel} = 2(\Delta E)/\hbar v_{\mathrm{F}} \approx 0.03\,\text{Å}^{-1}$, with $v_{\mathrm{F}} \approx 0.95 \times 10^6\,\mathrm{ms}^{-1}$ the Fermi velocity of graphene on Ir(111) [35]. The calculated value of $q_{\parallel}$ coincides with the observed indentation. However, an indisputable proof of the ZO Kohn anomaly for graphene on Ir(111) is still pending. It could be obtained by acquiring the dispersion relation with a higher wave vector resolution close to $\bar{\Gamma}$.

2.5 Phonon Energy Gaps at $\bar{\mathrm{K}}$

At the $\bar{\mathrm{K}}$ point of the surface Brillouin zone ZA, ZO [Figs. 2.9(a),(b)] and LA, LO [Figs. 2.9(c),(d)] phonons exhibit a splitting of their energies. To see this splitting most clearly, representative off-specular energy loss spectra acquired at $\bar{\mathrm{K}}$ are shown in Figs. 2.9(b),(d). The energy difference between the ZA [59 meV, Fig. 2.9(b)] and ZO [68 meV, Fig. 2.9(b)] phonon is 9 meV, while LA [150 meV, Fig. 2.9(d)] and LO [158 meV, Fig. 2.9(d)] phonon energies differ by 8 meV. This experimental observation is not reproduced by the density functional calculations. Indeed, for pristine graphene

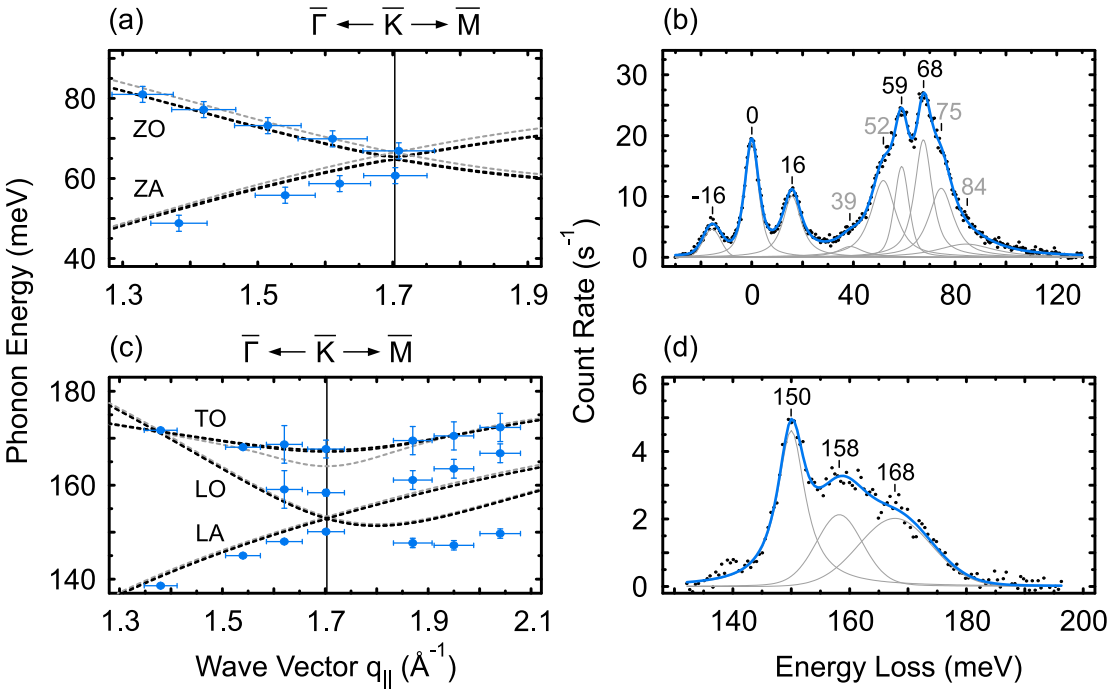

Fig. 2.9: Dispersion curves of **(a)** ZA, ZO and **(c)** LA, LO phonons of graphene on Ir(111). Dots represent experimental data, black and gray dashed lines show calculated results for graphene on Ir(111) and pristine graphene, respectively. **(b)** Off-specular energy loss spectrum acquired at $\bar{K}$ with an impact electron energy of 192 eV. The blue line is the superposition of Voigt profiles (gray lines) that were used to fit experimental data. Loss features at 59 meV and 68 meV are due to electron scattering from ZA and ZO phonons, respectively. Features at 39 meV, 52 meV and at 75 meV, 84 meV are assigned to spectroscopic signatures of replica of ZA and ZO phonons, respectively. Peaks at 16 meV (−16 meV) are attributed to the energy loss (gain) of electrons scattered from Ir(111) surface phonons [179]. The maximum at zero energy reflects quasi-elastically scattered electrons. **(d)** Off-specular energy loss spectrum acquired at $\bar{K}$ with an impact electron energy of 111 eV. The blue line is the superposition of Voigt profiles (gray lines) that were used to fit experimental data. Loss features at 150 meV, 158 meV, 168 meV are due to electron scattering from LA, LO, TO phonons, respectively.

dispersion curves of ZA and ZO phonons as well as of LA and LO phonons intersect at $\bar{K}$, which reflects their degeneracy due to the same E'' and E' symmetry, respectively [182]. Considering the weak interaction between graphene and Ir(111) calculations arrive at marginally different energies between the phonon branches at $\bar{K}$ [180]. For ZA and ZO phonons the calculated energy splitting is less than 0.5 meV while for LA and LO phonons energies differ by less than 0.1 meV at $\bar{K}$.

At present, the origin of this discrepancy between experimental and calculated data is unclear. In the following we first rule out sources for experimental uncertainties and then suggest possible explanations to the deviation of experimental from calculated data. Experimentally, a misalignment of the sample can be excluded. Adjusting the

$\bar{\Gamma}\bar{\mathrm{K}}$ direction has been achieved by rotating the sample and simultaneously controlling the low-energy electron diffraction pattern. We estimate an orientation accuracy of $\approx 1°$. Within this accuracy margin phonon modes with a calculated energy difference of 2 meV may be detected around $\bar{\mathrm{K}}$, which is much lower than the observed energy differences. Further, the correct rotation angle of the spectrometer analyzer in off-specular experiments is ensured by following the intensity of the diffuse elastic peak as a function of the analyzer rotation angle [Fig. 2.5(b)]. Intensity maxima reflect Bragg diffractions of the electrons and occur at integer multiples of the moiré reciprocal lattice vector [Fig. 2.5(a)]. The periodicity of the intensity maxima is in agreement with the moiré superstructure.

A hint to a possible explanation to the discrepancy between experiment and theory is the adaption of the graphene lattice constant to the Ir(111) lattice constant in the *ab initio* calculations. As a consequence all C atoms reside at equivalent Ir(111) adsorption sites, *i. e.*, the moiré superstructure is not considered in the calculations. The moiré superstructure, however, reflects the incommensurability of both lattices and implies a corrugation of graphene on Ir(111), *i. e.*, the C atoms are located at different adsorption sites and adsorption heights. These different adsorption geometries may lead to different symmetries of ZA, ZO and LA, LO phonons at $\bar{\mathrm{K}}$, which in turn may lift their degeneracy and result in a larger energy splitting. Indeed, in a refined version of the aforementioned linear chain model a two-atom basis may be considered in order to reflect the inequivalent adsorption sites of C atoms. The relative strengths of the springs connecting both atoms to the substrate vary periodically within the moiré supercell. Preliminary calculations reveal that in such a model an energy gap occurs at the Brillouin zone boundary. An additional contribution to the energy splitting may result from an avoided crossing of the phonon dispersion curves with their replica at $\bar{\mathrm{K}}$. A similar observation has been reported from the electronic bandstructure of graphene on Ir(111) [29], where the intersection of the Dirac cone with its moiré-induced replica was avoided by the opening of energy gaps. This scenario may hold for phonon dispersion curves, too. In this case the moiré superstructure would represent an additional potential for the graphene phonons.

Summary and Conclusions

The phonon dispersion relation of graphene on Ir(111) is determined by angle-resolved inelastic electron scattering. This dispersion relation is very similar to the dispersion curves of pristine graphene. However, the adsorption of graphene to Ir(111) leaves its clear fingerprints in the graphene phonon dispersion despite the large graphene–metal distance. First, graphene on Ir(111) is archetypical in revealing subtle aspects of electron-

phonon coupling and electron correlations in graphene. The modified Kohn anomaly of the highest optical phonon branch around $\bar{\mathrm{K}}$ is a signature of the reduced electron-phonon coupling, which is induced by the screening of the electron-electron interaction in graphene by the metal electron gas. This screening efficiently damps correlations effects that are not captured by density functional calculations. It renders standard local exchange-correlation functionals precise enough for modeling phonon dispersions of graphene on metal surfaces with a weak graphene–metal interaction. Secondly, the lattice mismatch between graphene and Ir(111) imposes a moiré superstructure to graphene which influences its dynamical properties. As a result, phonon bands of adsorbed graphene are replicated by multiples of the superstructure lattice vector. Finally, deviations of phonon energies from values predicted for pristine graphene have been traced to the weak but finite graphene–Ir interaction. The experimental observation of an appreciable energy splitting for transverse as well as for longitudinal phonons at a high-symmetry point of the surface Brillouin zone challenges state-of-the-art calculations and may spark future simulations that take van der Waals interactions and the moiré superstructure into account.

CHAPTER 3

Decoupling of Phthalocyanines from Ir(111) Surfaces

The results presented have been published in The Journal of Chemical Physics ***141****, 184308 (2014). Scanning tunneling microscopy images were obtained by* ***Sandra Gozdzik*** *and* ***Nicolas Néel****, both members of our group. Theoretical support was provided by* ***Andreia Luisa da Rosa****,* ***Thomas Frauenheim*** *and* ***Tim Oliver Wehling****, all from the Bremen Center for Computational Materials Science, University Bremen, Germany.*

The vacuum properties of organic molecules are modified to different extents upon adsorption to metal surfaces. In order to preserve these properties we explore the suitability of graphene as a buffer layer that decouples phthalocyanines from Ir(111).

3.1 Metal-Free Phthalocyanines

Metal-free phthalocyanines [$C_{32}H_{18}N_8$, H_2Pc, Fig. 3.1(a)] are aromatic macrocyclic compounds that are widely used in dyeing owing to their intense blue color. They are outstanding in terms of stability and availability [185], which is certainly a reason for their frequent use in surface chemistry. Owing to their chemical reactivity, optoelectronic conductance, optical absorbance, and their application as electron donors and acceptors these molecules are conceived as promising building blocks for molecular electronics [185, 186]. Upon adsorption to a surface the mentioned properties depend on the specific arrangement of the molecules [187–190] and their hybridization with the substrate [64, 191–197]. Therefore, it is not surprising that various surface science techniques — in particular scanning tunneling microscopy — have been employed to unravel structural aspects of phthalocyanine assemblies on metal surfaces [64, 198] and, very recently, on graphene [95, 177, 199–202].

The question whether graphene on Ir(111) acts as a buffer layer that efficiently decouples molecules from the metallic substrate represented the impetus to this work. Very often successful decoupling is identified by the similarity of the electronic properties of the adsorbed molecule with those of the free, *i. e.*, non-supported, molecule [64, 191–197]. Recently, the line shape of features in vibrational spectra of molecules adsorbed to graphene has been used to gain information about the degree of decoupling [99]. Here we followed a different idea. Does the molecule retain its vacuum geometric structure upon adsorption to the buffer layer? To observe possible effects of adsorption most clearly we compared the adsorption behavior of H_2Pc on Ir(111) and on Ir(111) covered with a single graphene layer. Graphene on Ir(111) exhibits the largest graphene–metal distance ($\approx 340\,\mathrm{pm}$) [27] reported to date and, therefore, may be expected as an appropriate buffer layer. For H_2Pc on Ir(111) and on graphene-covered Ir(111) STM images of the molecule look similar and potential differences in the adsorption geometries are difficult to discern. In contrast, the comparison of vibrational spectra obtained from angle-resolved inelastic electron scattering in specular and off-specular scattering geometries clearly hints at a strongly deformed H_2Pc on Ir(111) and at a planar adsorption geometry on graphene. These findings are corroborated by density functional calculations and reveal that graphene on Ir(111) acts as an interjacent layer that strongly reduces the molecule–metal hybridization.

Experimental

Experiments were performed with a scanning tunneling microscope operated in ultrahigh vacuum (10^{-9} Pa) and at 78 K (6 K) for H_2Pc on Ir(111) [H_2Pc on graphene-covered Ir(111)]. Clean Ir(111) surfaces were obtained after several cycles of Ar^+ bombardment and annealing at 1200 K. A single layer of graphene on Ir(111) was prepared by thermal decomposition of C_2H_4 [108]. Clean sample surfaces at room temperature were exposed to H_2Pc sublimated from a heated Ta crucible. The deposition rate was monitored by a quartz microbalance. STM images were recorded at constant current with the bias voltage applied to the sample. Vibrational spectroscopy was performed with an Ibach spectrometer [127] at room temperature. The incident monochromatic electron beam enclosed an angle of 64° with the surface normal.

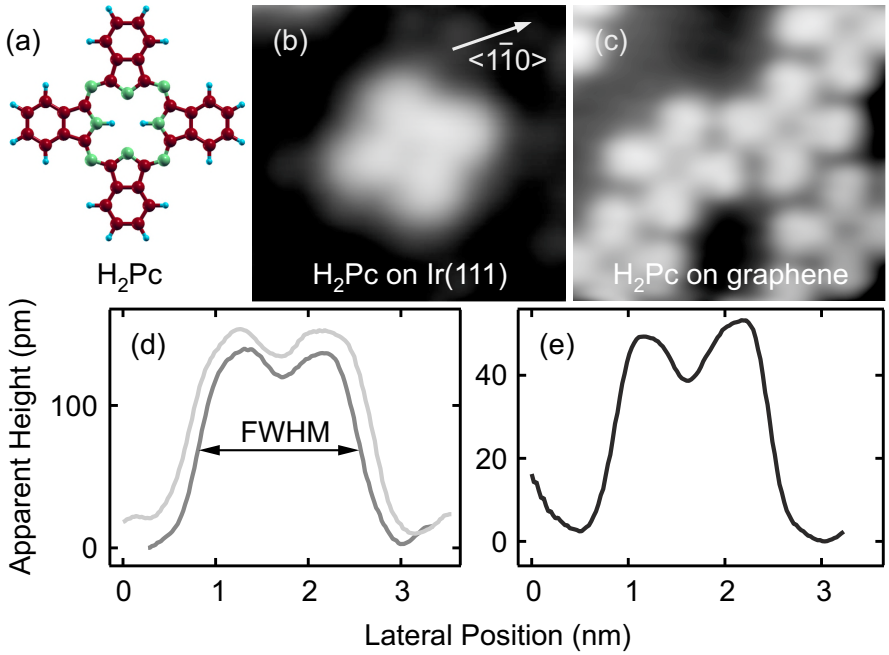

Fig. 3.1: **(a)** Relaxed vacuum structure of H_2Pc with H, C, N atoms appearing as blue, red, green spheres, respectively. **(b)** Constant-current STM image of H_2Pc on Ir(111) (50 pA, 0.1 V, $3.7 \times 3.5\,nm^2$). The gray scale ranges from 0 (black) to 150 pm (white). **(c)** Constant-current STM image of H_2Pc on graphene-covered Ir(111) (10 pA, 1.0 V, $3.7 \times 3.5\,nm^2$). The gray scale ranges from 0 (black) to 53 pm (white). **(d)** Cross-sectional profiles of H_2Pc on Ir(111) parallel (gray) and perpendicular (dark gray) to $\langle 1\bar{1}0 \rangle$ crystallographic directions [indicated as an arrow in (b)]. The top profile has been shifted vertically by 15 pm for clarity. The full width at half maximum (FWHM) is indicated. **(e)** Cross-sectional profiles of H_2Pc adsorbed to graphene on Ir(111). Only a single profile is plotted since profiles along perpendicular directions across the molecule are virtually identical. STM data were processed using WSxM [157]. Apparent height and FWHM are summarized in Table 3.1.

Results and Discussion

Figure 3.1 shows constant-current STM images of H_2Pc adsorbed to Ir(111) [Fig. 3.1(b)] and to graphene on Ir(111) [Fig. 3.1(c)]. The characteristic cross shape of H_2Pc [Fig. 3.1(a)] as well as a central depression is visible in both images. To avoid the dominant contribution of a specific molecular orbital to constant-current STM images, bias voltages have been chosen in the gap between the signatures of the highest occupied and the lowest unoccupied molecular orbitals in spectra of the differential conductance. The rather high bias voltage and low tunneling current in case of H_2Pc on graphene were required for stable imaging conditions. Even at low temperatures translations of H_2Pc were easily induced by the presence of the STM tip. The enhanced mobility of molecules on graphene is likewise reflected by the exclusive occurrence of molecule assemblies rather than single molecules. From cross-sectional profiles acquired across the molecules [Figs. 3.1(d),(e)] lateral extensions and apparent heights were extracted and summarized in Table 3.1. One isoindole-isoindole axis of H_2Pc molecules on Ir(111) is aligned with crystallographic $\langle 1\bar{1}0 \rangle$ directions [Fig. 3.1(b)]. Cross-sectional profiles acquired along these directions exhibit a larger full width at half maximum (FWHM) than along perpendicular directions. The widths differ by $\approx 0.2\,\mathrm{nm}$ (Table 3.1). According to cross-sectional profiles of H_2Pc on graphene acquired along a direction defined by opposite isoindole groups molecules on graphene appear symmetric and smaller than molecules on Ir(111). However, inferring the actual geometric structure of the molecule from STM images alone is difficult. Therefore, the aforementioned deviations in cross-sectional profiles are not necessarily related to structural differences.

Tab. 3.1: Full width at half maximum (FWHM) and apparent height of H_2Pc on Ir(111) and on graphene determined from cross-sectional profiles presented in Figs. 3.1(d),(e).

	FWHM (nm)	Height (pm)
H_2Pc on Ir(111)	2.0	135
	1.8	
H_2Pc on graphene	1.6	53
	1.6	

In contrast, strong differences occur in vibrational spectra. Figures 3.2(a),(b) show specular electron energy loss spectra obtained from H_2Pc adsorbed on Ir(111) [Fig. 3.2(a)] and from H_2Pc on graphene-covered Ir(111) [Fig. 3.2(b)]. Quartz microbalance readings and deposition times show that the coverages in both cases are similar and in the submonolayer range. While energy ranges $53\,\mathrm{meV} < E < 84\,\mathrm{meV}$ and $E > 117\,\mathrm{meV}$

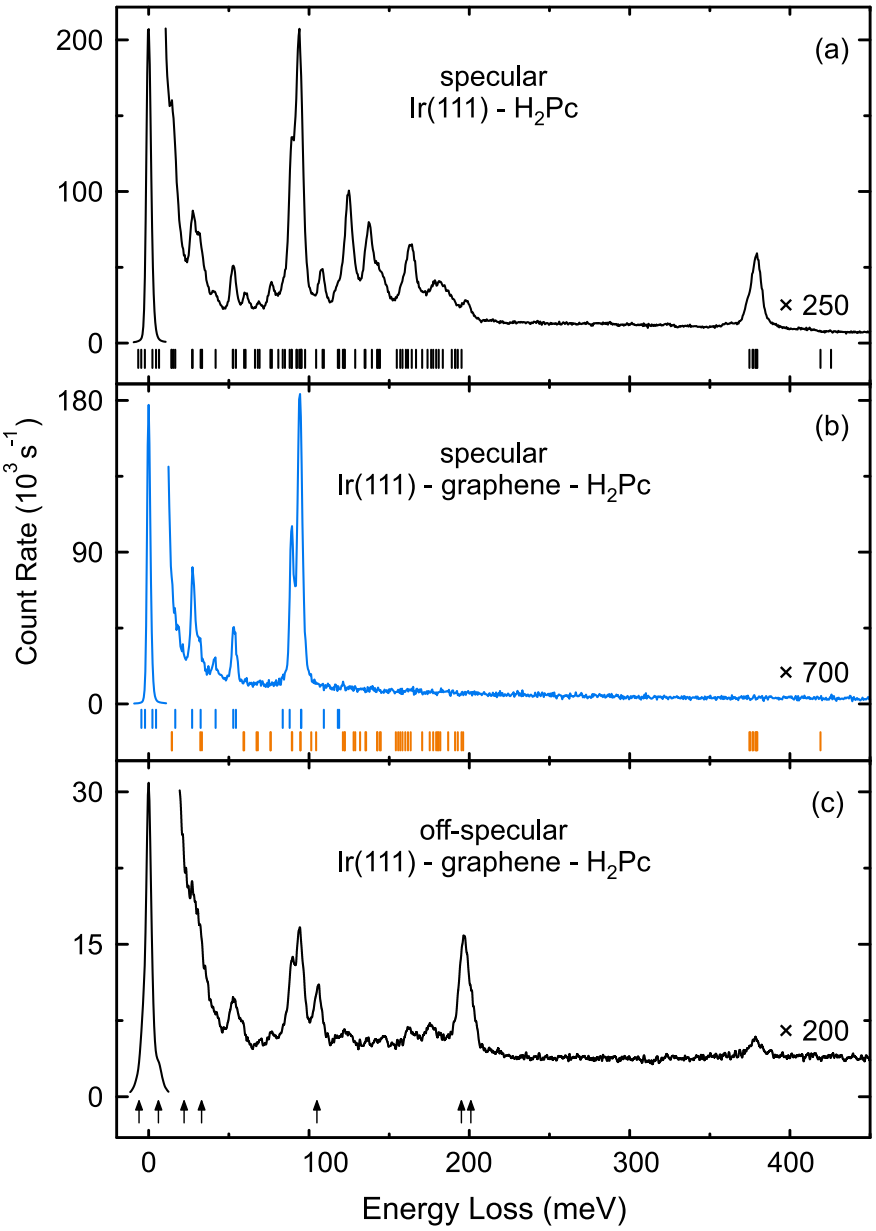

Fig. 3.2: Specular electron energy loss spectra acquired from H_2Pc molecules adsorbed **(a)** to Ir(111) and **(b)** to graphene on Ir(111) with an energy resolution of 2.5 meV and an impact electron energy of 6 eV. The peaks at zero energy reflect elastically scattered electrons while the other features represent spectroscopic signatures of molecule vibrations. In (a) vertical bars at the bottom indicate calculated vibrational energies of infrared-active out-of-plane modes of H_2Pc that are compatible with C_s symmetry. Blue and orange vertical lines in (b) correspond to calculated energies of infrared-active vibrational modes with an out-of-plane and in-plane oscillating dipole moment, respectively, for H_2Pc with D_{2h} symmetry. **(c)** Off-specular spectrum of H_2Pc on graphene acquired with an impact electron energy of 11 eV and a momentum transfer of $q_{\parallel} = 0.25\,\text{Å}^{-1}$. Arrows indicate spectroscopic signatures which could be affected or caused by graphene phonons [180].

show various loss features in specular spectra of H_2Pc on Ir(111), these energy intervals are depleted of spectroscopic signatures in specular spectra of H_2Pc of graphene. Several impact electron energies between 3 and 11 eV were used to explore a possible effect of the scattering cross section on the presence or absence of vibrational features in the spectra. However, apart from intensity variations of the peaks that are already present in Fig. 3.2(b) spectroscopic signatures in the aforementioned energy intervals remained absent from specular spectra of H_2Pc on graphene. The molecule coverage neither plays a role in the observed effect. While increasing coverages lead to a gradual rise of the loss peaks visible in Fig. 3.2(b) additional spectroscopic signatures do not appear.[1] They do occur as soon as off-specular scattering geometries are employed [Fig. 3.2(c)].

Based on the presented spectroscopic results we suggest a strong interaction between H_2Pc and Ir(111), which leads to a deformation of the molecular plane. We further propose that H_2Pc on graphene, in contrast, retains its planar structure owing to an efficient decoupling of the molecule from Ir(111) by the interjacent graphene layer. The suggested molecule configurations were corroborated, first, by calculating the symmetry and energy of all H_2Pc vibrational modes and, second, by simulating the relaxed adsorption geometries.

In specular scattering geometries only infrared-active vibrational modes with an oscillating dipole moment oriented perpendicular to the surface (out-of-plane modes) can be detected while modes with a parallel oscillating dipole moment (in-plane modes) remain absent from specular loss spectra [129]. The presence or absence of specific loss features in specular spectra thus reflects the symmetry of the adsorbate complex. Density functional theory calculations [203] using Gaussian09 [204] with the hybrid functional B3LYP [205] and the Gaussian basis set $6-311G$ [206, 207] were performed to find the complete set of H_2Pc vibrational modes. These calculations were restricted to the free molecule.

While the free molecule may be a good approximation to H_2Pc on graphene the comparison of calculated vibrational energies with experimental data for H_2Pc on Ir(111) requires further discussion. The line shapes of spectroscopic signatures appearing in specular spectra of H_2Pc on Ir(111) are symmetric. Therefore, the corresponding vibrational modes do not couple strongly to the substrate. Asymmetric Fano profiles are expected for an appreciable interaction between vibrational modes and substrate electronic states [99, 101, 102, 208–212]. In addition, Table 3.2 shows that vibrational energies obtained from specular spectra of H_2Pc on Ir(111) [Fig. 3.2(a)] virtually coincide with energies of loss features in specular [Fig. 3.2(b)] and off-specular [Fig. 3.2(c)] spectra

[1] For detailed specular electron energy loss spectra showing the influence of the impact electron energy and the H_2Pc coverage, please refer to Appendix D.

Tab. 3.2: Energies, E_{vib}, of H_2Pc vibrational modes on Ir(111) (top row) and on graphene-covered Ir(111) (bottom row). Values for Ir(111)-H_2Pc were obtained from specular spectra while vibrational energies for graphene-H_2Pc were determined from specular (s) and off-specular (o) spectra. Underlined data indicate that corresponding loss features appear as a shoulder to adjacent spectroscopic signatures. An energy loss of H_2Pc on graphene at ≈ 198 meV is most likely dominated by the strong spectroscopic signature of an optical graphene phonon.

Ir(111)-H_2Pc E_{vib} (meV)	15	27	31	40	53	61	69
	77	<u>85</u>	89	94	108	<u>118</u>	125
	137	<u>145</u>	163	180	198	379	
graphene-H_2Pc E_{vib} (meV)	<u>18</u> (s)	28 (s)	32 (s)	41 (s)	53 (s)	<u>62</u> (o)	71 (o)
	77 (o)	84 (s)	89 (s)	94 (s)	108 (s)	117 (s)	123 (o)
	136 (o)	147 (o)	161 (o)	175 (o)	/	378 (o)	

of H_2Pc adsorbed on graphene-covered Ir(111). Therefore, a potential chemical shift between corresponding loss features of the two surfaces is difficult to identify. In particular, a uniform increase of vibrational energies, which may be expected for chemisorbed molecules [99] has not been observed.

The H_2Pc molecule contains 58 atoms and, thus, 168 fundamental vibrational modes. Due to the D_{2h} symmetry of H_2Pc these vibrational modes may be further grouped into 13 A_u modes with no optical activity, 71 infrared-active modes (15 B_{1u}, 28 B_{2u}, 28 B_{3u}), and 84 Raman-active modes (29 A_g, 28 B_{1g}, 14 B_{2g}, 13 B_{3g}). We refer the reader to Appendix E, Section E.1, which contains character and symmetry correlation tables, a complete list of vibrational energies together with the assignment of vibrational modes to atom displacement patterns. The calculated energies were multiplied by 0.955 to match the experimental data for H_2Pc on both surfaces[2], which reflects the essentially identical vibrational energies (Table 3.2). The resulting energies of infrared-active modes appear as blue and orange vertical lines in Fig. 3.2(b) and Fig. 3.3 for out-of-plane and in-plane vibrations, respectively. The dominant energy losses at 89 meV and 94 meV are the spectroscopic signatures of up and down motions of H atoms at the periphery of the benzene groups. At 89 meV the inner porphyrazine ring exhibits some vertical displacements while it is virtually at rest for the vibrational mode at 94 meV. The loss feature at ≈ 379 meV is due to in-plane C–H stretch modes.

A comparison of calculated and experimental data reveals a good agreement of calculated out-of-plane mode energies and all experimentally observed loss energies in specular spectra of H_2Pc on graphene. We therefore suggest that in-plane modes are

[2] The factor $c = 0.955$ results from a linear fit $E_{\mathrm{vib}}^{\mathrm{exp}} = cE_{\mathrm{vib}}^{\mathrm{calc}}$, with $E_{\mathrm{vib}}^{\mathrm{exp}}$ selected experimental signatures of H_2Pc on graphene and $E_{\mathrm{vib}}^{\mathrm{calc}}$ the corresponding calculated vibrational modes of free H_2Pc.

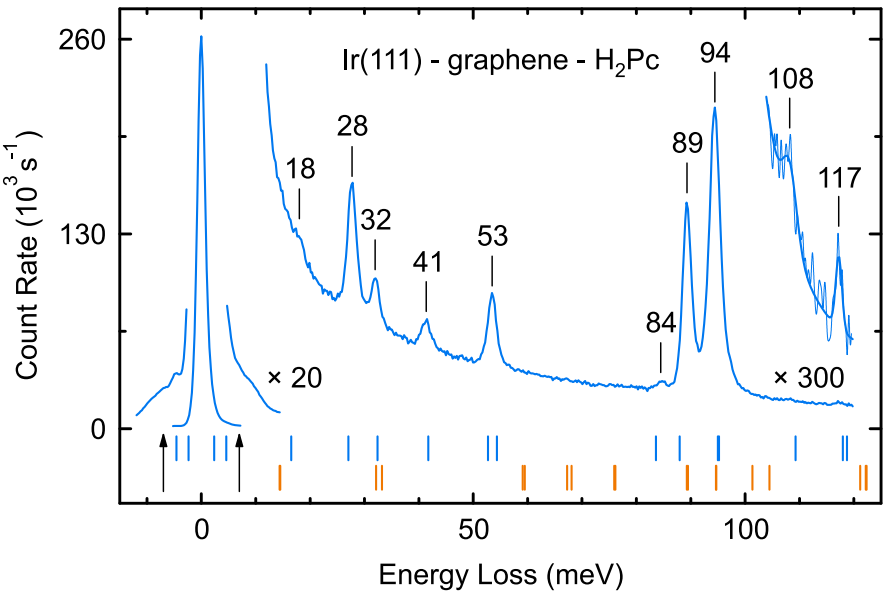

Fig. 3.3: Specular electron energy loss spectrum of H_2Pc adsorbed to graphene on Ir(111) acquired with an energy resolution of 1 meV and an impact electron energy of 3.5 eV. The absence of spectral features between 53 and 84 meV is clearly visible. The spectral range $E > 104$ meV has been magnified to see the weak losses at 108 meV and 117 meV more clearly. Vertical lines in the bottom indicate calculated energies of infrared-active out-of-plane (blue) and in-plane (orange) vibrational modes of H_2Pc with D_{2h} symmetry. Arrows indicate spectroscopic signatures at $\approx \pm 7$ meV which are most likely due to graphene out-of-plane acoustic phonons [Fig. 2.1(a)].

absent from these spectra.[3] To see the absence of in-plane vibrational modes in the energy range from 53 meV to 84 meV more clearly Fig. 3.3 shows a specular spectrum acquired from H_2Pc on graphene with high energy resolution. The depleted spectroscopic range between 53 and 84 meV is obvious. In off-specular scattering geometries a finite momentum parallel to the surface is transferred from the scattered electron to H_2Pc and in-plane modes may be efficiently excited [Fig. 3.2(c)]. Consequently, a planar adsorption geometry of H_2Pc on graphene is likely and hints at graphene acting as a buffer layer.

Upon adsorption of H_2Pc on Ir(111) additional vibrational modes compared to H_2Pc on graphene are observed from specular spectra [Fig. 3.2(a)]. In part, a deformation of the molecular plane may be the origin to this observation. Due to the distortion in-plane vibrational modes may now exhibit a perpendicular component of the oscillating dipole moment, which gives rise to their observation in specular spectra. Further, the

[3] Some in-plane vibration energies are virtually identical with out-of-plane vibration energies [Fig. 3.2(b)]. As a consequence, the potential contribution from in-plane vibration modes to specular energy loss spectra would not be resolvable. However, due to the nearly perfect coincidence of the entire set of calculated out-of-plane mode energies with loss energies in specular H_2Pc spectra the excitation of in-plane mode can be safely excluded.

suggested covalent bond of H_2Pc to Ir(111), which will be discussed below, leads to a reduction of the D_{2h} symmetry of the free H_2Pc molecule upon adsorption. Indeed, STM images [Fig. 3.1(b)] and cross-sectional profiles [Fig. 3.1(d)] hint at a reduced symmetry of H_2Pc adsorbed to the threefold symmetric Ir(111) surface. Similar adsorption-induced symmetry reductions of phthalocyanines have been observed [64, 213–215]. According to our calculations of relaxed adsorption geometries (see below), the relevant symmetry of the adsorbate complex, *i. e.*, H_2Pc on a two-layer Ir(111) slab, is C_s symmetry. Consequently, A_g, B_{2g} and B_{3u} vibrational modes, which are forbidden to occur in specular spectra of H_2Pc with D_{2h} symmetry become observable due to the symmetry reduction. In Fig. 3.3(a) the vertical lines indicate vibrational energies of infrared-active out-of-plane modes that are compatible with a C_s symmetry. Similar results were reported previously [214].

In addition to the comparison of experimental and calculated vibrational energies we performed density functional theory calculations to determine the preferred adsorption geometry of H_2Pc on both Ir(111) and on free graphene. The supercells were built using the bulk lattice constants, *i. e.*, 0.384 nm for Ir and 0.244 nm for graphene. We have employed the Projected Augmented Wave method [216] as implemented in the Vienna *Ab initio* Simulation Package [217, 218]. The generalized gradient approximation was applied to the exchange-correlation functional using the Perdew-Burke-Ernzerhof (PBE) [219] parameterization. Van der Waals interactions were taken into account through the Tkatchenko-Scheffler method [220]. The adsorption on Ir(111) was modeled by a 7×7 supercell with a two-layer slab containing 98 Ir atoms and a single H_2Pc. The molecule on graphene was modeled by a 9×9 supercell containing 162 C atoms and a single H_2Pc molecule. Only the Γ point has been used for Ir(111). Charge density integration for graphene was performed on a $8 \times 8 \times 1$ **k**-point mesh. Tests with larger cells and numbers of **k**-points have shown that the most stable adsorption geometries and corresponding adsorption energies are similar. The kinetic energy has been curtailed at 400 eV in all calculations. All atoms were allowed to relax until the forces were smaller than 10 meV nm^{-1}. The unit cell included a vacuum size of 1.3 nm, which is large enough to render interactions between molecules in neighboring cells negligibly small.

Our calculations show that the ground-state configuration of H_2Pc on Ir(111) is characterized by a strongly distorted molecule with aromatic rings of the molecule close to the surface and the molecular center containing the pyrrole-like subunits moved upwards. In Figs. 3.4(a),(b) we show this configuration, where all aromatic rings bent down to the Ir surface. The H atoms which belong to the aromatic rings relax upwards suggesting that the C atoms are involved in the molecule–substrate binding. These C atoms are separated from nearest Ir atoms by 0.23 nm, which shows the covalent character

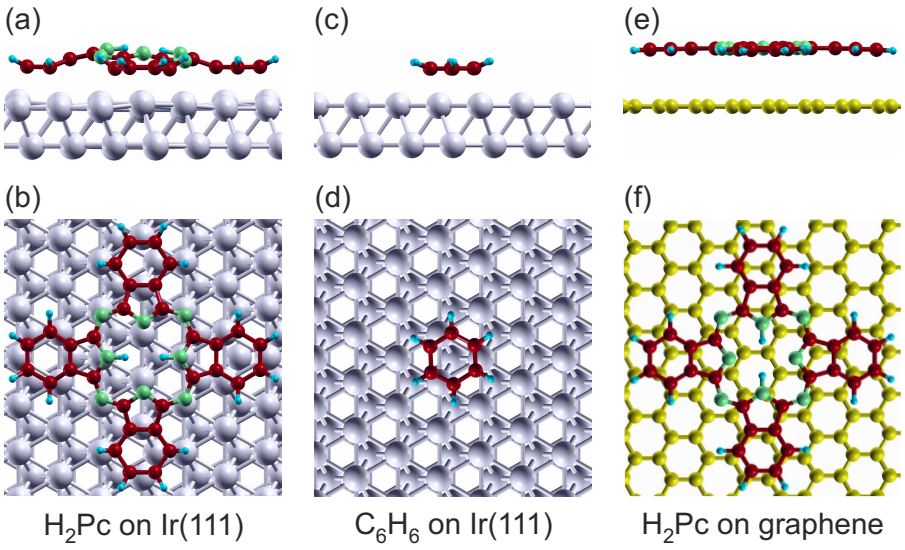

Fig. 3.4: Side and top views of calculated adsorption geometries of **(a)**, **(b)** H_2Pc on Ir(111) and **(c)**, **(d)** C_6H_6 on Ir(111) as well as **(e)**, **(f)** H_2Pc on free graphene.

of the C–Ir bonds with an adsorption energy of 2.2 eV. The simulated relaxed adsorption configuration gives a hint to the absence of a chemical shift of some vibrational modes for H_2Pc on Ir(111) compared with H_2Pc on graphene-covered Ir(111). The dominant double-peak structure (89 meV, 94 meV) is visible in specular spectra of H_2Pc on both surfaces [Figs. 3.2(a),(b)]. This loss feature is the spectroscopic signature of the out-of-plane motion of peripheral H atoms (89 meV, 94 meV) and of the inner porphyrazine ring (89 meV). According to the calculations the peripheral H atoms as well as the inner porphyrazine ring relax upwards [Figs. 3.4(a),(b)] and thus show a reduced coupling to Ir(111) due to their larger distance from the surface. The benzene groups, in contrast, take an active role in the covalent bonding of H_2Pc on Ir(111). Vibrational modes that involve vertical motions of the whole benzene group exhibit energies below 20 meV and are thus difficult to access in specular spectra [Fig. 3.2(a)].

In order to understand the adsorption geometry of H_2Pc on Ir(111) in more detail investigations into the relaxed structure of a benzene (C_6H_6) molecule on Ir(111) were performed [Figs. 3.4(c),(d)]. Similar to observations from H_2Pc adsorption to Ir(111), the H atoms of C_6H_6 are lifted while the C atoms are closest to Ir with akin C–Ir bond lengths. The covalent binding of aromatic rings to Ir is thus a rather general phenomenon. We find that the most stable configuration is obtained when the C_6H_6 center resides above a Ir(111) hexagonal close-packed hollow site [Fig. 3.4(d)]. In this adsorption geometry the six C atoms are located in the vicinity of Ir(111) on-top positions [Fig. 3.4(d)]. A single C_6H_6 molecule can always reach this configuration. In the case of

H_2Pc molecules, however, a compression of the molecule and a concomitant bending of its plane is required to obtain the aforementioned registry of the isoindole rings with Ir(111).

On graphene the H_2Pc adsorption geometry changes drastically [Figs. 3.4(e),(f)]. The molecule adsorbs at an average distance of 0.34 nm above the graphene, which is compatible with physisorption. In addition, the molecule virtually retains its relaxed vacuum structure, *i. e.*, it remains planar. We have performed calculations both for a fixed [Figs. 3.4(e),(f)] and for a relaxed graphene lattice. In both cases the molecule configurations are virtually identical, while in the second case graphene slightly bends downwards below the molecule center. This slight distortion of the graphene layer reflects its reported flexibility [221].

As a result, the calculations corroborate the experimental findings based on vibrational spectroscopy. H_2Pc experiences substantial deformations of its molecular structure upon adsorption on Ir(111), while it retains its planar vacuum structure on graphene. These structural properties of adsorbed molecules have been inferred from laterally averaging spectroscopy of vibrational excitations rather than from STM images. In a previous report scanning tunneling spectroscopy of the electronic structure has been used to unravel geometrical aspects of a molecular switch [222], which likewise demonstrates the importance of spectroscopy in clarifying structural properties.

3.2 Manganese Phthalocyanines

Along with H_2Pc there is a large variety of phthalocyanines where the basic phthalocyanine skeleton forms coordination complexes with, *e.g.*, transition metal atoms. One of these phthalocyanines is manganese phthalocyanine ($C_{32}H_{16}MnN_8$, MnPc), a planar molecule with an average magnetic moment of 4.33 μ_B (μ_B: Bohr magneton) [223]. Such single molecule magnets attract rising attention in molecular spintronics [224]. Recent investigations have been shown that the spin of MnPc can be reversibly switched between two states by hydrogen adsorption and desorption [225] and that MnPc is a nearly perfect spin filter [226]. However, the magnetic moment of free MnPc is reduced to different extents upon adsorption to surfaces [227, 228]. Here, we will demonstrate that the suggested decoupling in Section 3.1 due to an interjacent graphene layer is not restricted to H_2Pc, but also applicable to MnPc. To this end, clean Ir(111) and graphene-covered Ir(111) surfaces at room temperature were exposed to MnPc sublimated from a heated Ta crucible.

Figures 3.5(a),(b) show specular electron energy loss spectra obtained from MnPc adsorbed on Ir(111) [Fig. 3.5(a)] and from MnPc on graphene-covered Ir(111) [Fig. 3.5(b)],

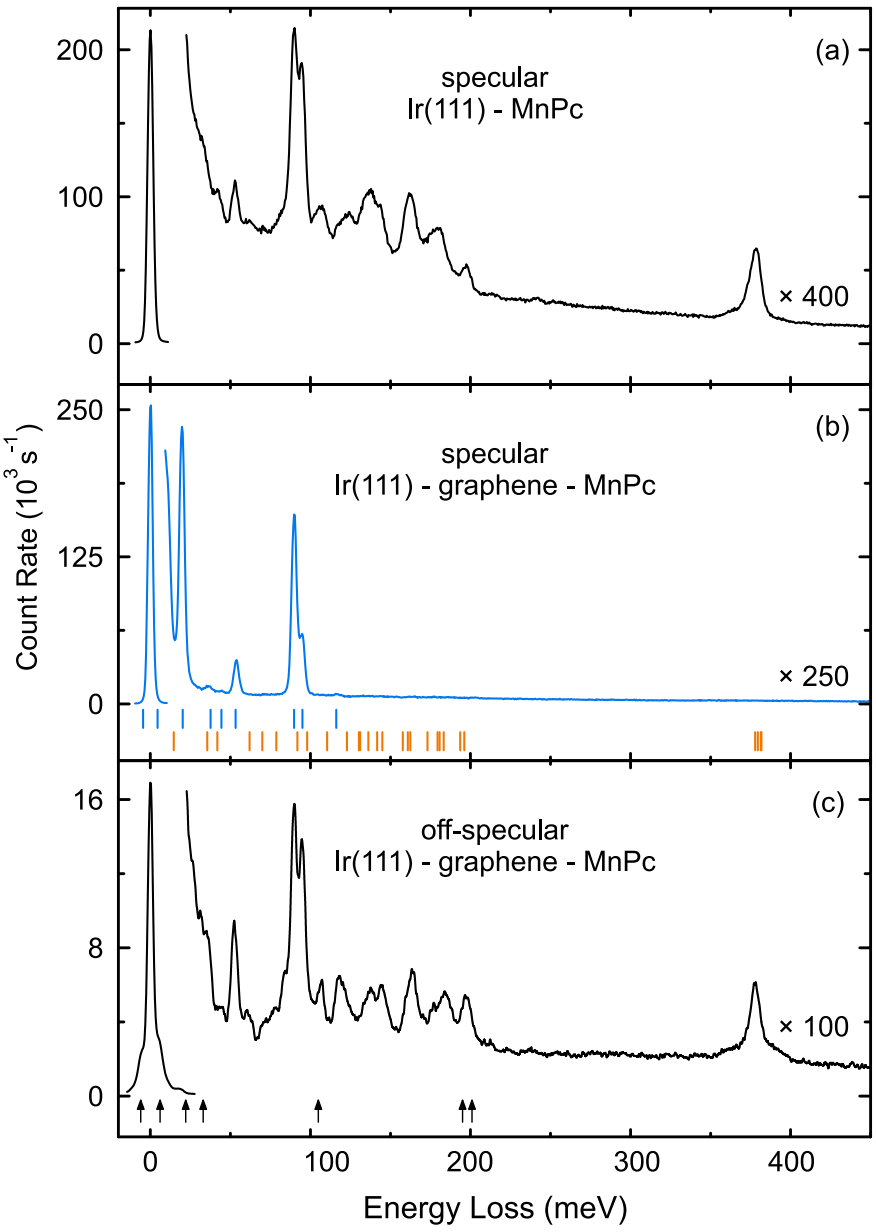

Fig. 3.5: Specular electron energy loss spectra acquired from MnPc molecules adsorbed **(a)** to Ir(111) and **(b)** to graphene on Ir(111) with an energy resolution of 2.5 meV and an impact electron energy of 6 eV. The peaks at zero energy reflect elastically scattered electrons while the other features represent spectroscopic signatures of molecule vibrations. Blue and orange vertical lines in (b) correspond to calculated energies of infrared-active vibrational modes with an out-of-plane and in-plane oscillating dipole moment, respectively, for MnPc with D_{4h} symmetry. **(c)** Off-specular spectrum of MnPc on graphene acquired with an impact electron energy of 6 eV and a momentum transfer of $q_{\parallel} = 0.24\,\text{Å}^{-1}$. Arrows indicate spectroscopic signatures which could be affected or caused by graphene phonons [180].

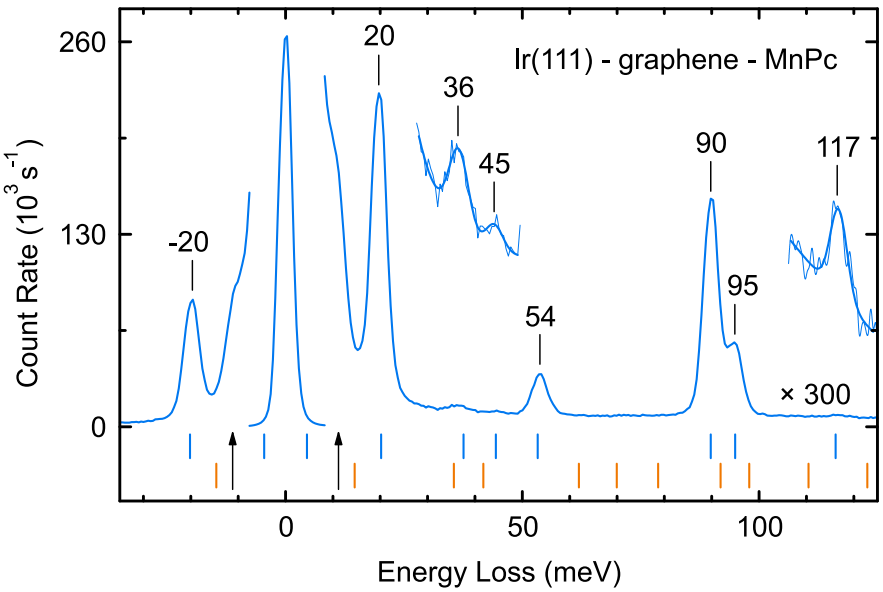

Fig. 3.6: Specular electron energy loss spectrum of MnPc adsorbed to graphene on Ir(111) acquired with an energy resolution of 1 meV and an impact electron energy of 6 eV. The absence of spectral features between 54 meV and 90 meV is clearly visible. The spectral ranges 28 meV $< E <$ 50 meV and $E >$ 106 meV have been magnified to see the weak losses at 36 meV, 45 meV and 117 meV more clearly. Vertical lines in the bottom indicate calculated energies of infrared-active out-of-plane (blue) and in-plane (orange) vibrational modes of MnPc with D_{4h} symmetry. Arrows indicate spectroscopic signatures which are probably due to graphene out-of-plane acoustic phonons.

both with a similar coverage below one monolayer. While energy ranges between 54 meV and 90 meV as well as above 117 meV exhibit various loss features in specular spectra of MnPc on Ir(111), these energy intervals are depleted of spectroscopic signatures in specular spectra of MnPc on graphene. However, the loss features occur in off-specular spectra of MnPc on graphene [Fig. 3.5(c)]. Based on these results we propose a similar adsorption behavior as for H_2Pc, *i.e.*, chemisorption of MnPc on Ir(111), which leads to a considerable deformation of the free molecule structure, and physisorption of MnPc on graphene, where the adsorbed molecules retain their planar vacuum structure.

To confirm this assumption the symmetry and energy of all MnPc vibrational modes were determined by DFT calculations [203] using Gaussian09 [204] with the hybrid functional B3LYP [205] and the Gaussian basis set 6 − 311G(2d,2p) [206, 207, 229–231]. The calculations were restricted to the free MnPc molecule which contains 57 atoms and, thus, 165 fundamental vibrational modes. The vibrational modes were calculated in the harmonic approximation with the molecule symmetry fixed to D_{4h}. A complete list of vibrational energies together with their mode symmetries, the assignment of vibrational modes to atom displacement pattern as well as character and symmetry correlations

tables are listed in Appendix E, Section E.2. In order to facilitate a comparison between experimental and theoretical data, calculated vibrational energies were multiplied by a factor of 0.962.[4]

In Fig. 3.5(b), calculated infrared-active out-of-plane vibrational modes (blue lines) coincide with all vibrational signatures of MnPc on graphene, while at loss energies of calculated infrared-active in-plane modes (orange lines) no vibrational signatures are discernible. This becomes particularly apparent in specular energy loss spectra of MnPc on graphene acquired with a high energy resolution [Fig. 3.6]. The absence of spectral features between 54 meV and 90 meV clearly indicates that in-plane modes are not excited. These modes are not observable until off-specular spectra are measured [Fig. 3.5(c)] where a finite momentum parallel to the surface is transferred between the impinging electrons and the MnPc molecules. Using the same argumentation as for H_2Pc, the results presented hint at a planar adsorption of MnPc on graphene, *i. e.*, also MnPc can be efficiently decoupled from Ir(111) by means of an interjacent graphene layer.

In contrast, specular spectra of MnPc on Ir(111) [Fig. 3.5(a)] exhibit additional features in comparison to those of MnPc on graphene [Fig. 3.5(b)]. The appearance of additional features suggests a deformation of the free MnPc geometry due to chemisorption of MnPc on Ir(111). The resulting adsorbate complex, which consists of MnPc and at least two Ir layers, has a reduced symmetry in comparison to the D_{4h} symmetry of free MnPc.[5] As a consequence, additional modes of MnPc are dipole-allowed and become visible in specular spectra of MnPc on Ir(111) [Fig. 3.5(a)].

Summary and Conclusions

Spectroscopic rather than microscopic data contain valuable structural information on the molecular adsorption geometry. Due to chemisorption of H_2Pc on Ir(111) a considerable deformation of the free-molecule structure and a reduction of the molecular symmetry in vacuum occur. In contrast, H_2Pc retains its planar vacuum structure upon physisorption on graphene. The same arguments hold for MnPc. As a consequence, graphene on Ir(111) acts as an interjacent buffer layer that efficiently reduces the H_2Pc–Ir and MnPc–Ir hybridization. The additional metal atom in MnPc does not seem to affect the decoupling effect of graphene. Therefore, graphene on Ir(111) can most probably serve as buffer layer for other phthalocyanines and similar organic molecules, too.

[4] The factor $c = 0.962$ results from a linear fit $E_{\mathrm{vib}}^{\mathrm{exp}} = cE_{\mathrm{vib}}^{\mathrm{calc}}$, with $E_{\mathrm{vib}}^{\mathrm{exp}}$ the experimental signatures of MnPc on graphene and $E_{\mathrm{vib}}^{\mathrm{calc}}$ the corresponding calculated vibrational modes of free MnPc.

[5] Actually, there is no indication of the exact symmetry of the adsorbate complex in the literature. However, the symmetry of the MnPc–Ir adsorbate complex can be determined, for example, by future DFT calculations.

CHAPTER 4

CO as a Probe for Electrostatic Dipole Interactions on Surfaces

The results presented have been published in The Journal of Physical Chemistry C ***120****, 11490 (2016). Measurements were performed in part with* ***Jan Hildisch****, a former member of our group. Theoretical support was provided by* ***Anja Michl*** *and* ***Stefan Müller****, both from the Institute of Advanced Ceramics, Hamburg University of Technology, Germany.*

The energy of an atomic or molecular vibrational mode may serve as a subtle probe for the interaction of the atom or molecule with its environment. On surfaces the adsorbate often exhibits an electrostatic dipole due to charge transfer upon adsorption. The electric dipole is then subject to interactions with the electric field of neighboring dipoles, which usually leads to changes in, *e. g.*, adsorption and vibrational energies [232–236]. A prominent example is the adsorption of alkali metals. Frustrated translations and perpendicular stretch modes were reported to change their energy with varying alkali metal coverage [237]. At very low and increasing coverages the energy increase of alkali metal vibrational modes was assigned to the long-range Lau-Kohn interaction mediated by the substrate electronic structure [238], while at intermediate coverages the electric dipole coupling between neighboring alkali metal atoms became more important [211, 239–241]. The coadsorption of alkali metals and CO was characterized by a reduction of the C–O stretch mode energy with increasing alkali metal coverage [242–244]. These observations were traced in part to the weakening of the C–O bond due to filling of the antibonding $2\pi^*$ CO orbital by substrate electrons [243] according to the Blyholder model [245]. Additionally, electrostatic interactions between the CO dipole and the modified surface dipole played an important role in the decrease of the CO vibrational energy [243].

In a more recent work the influence of H, NO, CO, O on the vibrational properties of CO adsorbed on Ru(0001) was investigated [246]. All coadsorbed molecules induced an increase of the C–O stretch mode energy, rather than a decrease as observed from coadsorbed alkali metals [242–244]. The Ru–CO stretch mode, however, decreased its energy with codeposition of H, NO, CO, O [246]. These observations were largely understood within the Blyholder model. In contrast to coadsorbed alkali metals the presence of H, NO, CO, O induced a depletion of the CO $2\pi^*$ orbital [246]. For the adsorption of CO and NO on Pt(111) adsorption-induced dipoles, bond lengths and changes in vibrational energies due to coverage-dependent dipolar interactions were calculated [236].

According to the aforementioned reports and to similar experiments changes in vibrational energies of a molecular probe are due to a complex combination of different interactions. It would be highly desirable to single out the effect of only a few coupling mechanisms. Here we show the impact of electrostatic dipole coupling on the vibrational properties of CO in a combined experimental and theoretical study. To this end H_2Pc molecules were adsorbed on Ir(111) precovered with a small amount of CO, which served as probe molecules. Increasing H_2Pc coverages led to a gradual decrease of the C–O stretch mode energy. Supporting DFT calculations reproduced the experimental findings and rationalized them in terms of electrostatic dipole interaction. Other possible causes

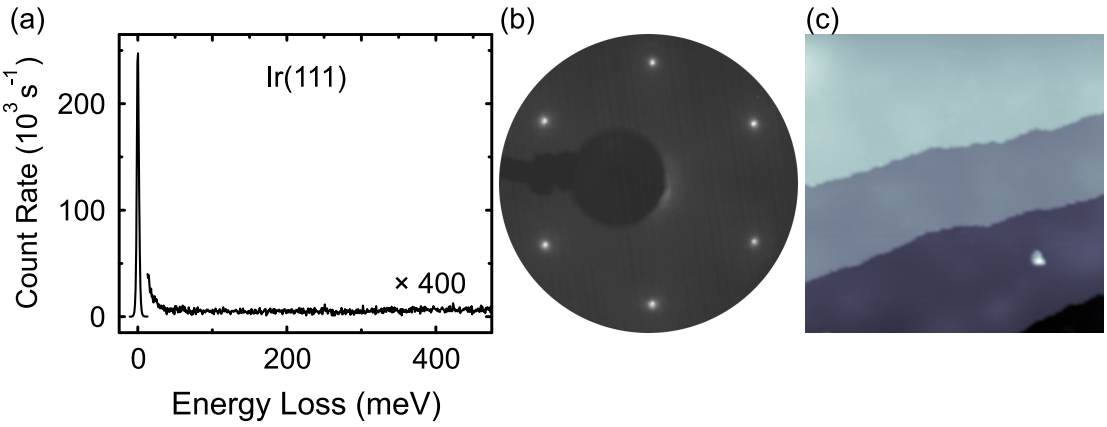

Fig. 4.1: (a) Specular energy loss spectra of clean Ir(111). **(b)** Low-energy electron diffraction pattern of Ir(111) (electron kinetic energy: 147 eV). **(c)** STM image showing four Ir(111) terraces (tunneling current: 0.2 nA, bias voltage: 0.5 V, $70 \times 70\,\mathrm{nm}^2$). STM data were processed with WSxM [157].

of the decrease of the C–O stretch mode energy were considered in the calculations and could be ruled out. Furthermore, the spectroscopic signature of the C–O stretch mode exhibited a characteristic asymmetric line shape starting from the lowest H_2Pc coverages. This line shape is consistent with the characteristic distance dependence of the electrostatic dipole interaction. Model calculations that take all allowed CO on-top adsorption sites at a given H_2Pc coverage on Ir(111) into account can reproduce the experimental line shape of the C–O stretch mode.

Experimental Methods

Vibrational spectra were acquired in ultrahigh vacuum (10^{-9} Pa) at room temperature by electron energy loss spectroscopy using an Ibach spectrometer [127]. Specular electron energy loss spectra were obtained with an impact electron energy of 6 eV and an energy resolution set to 2.5 meV. The incident monochromatic electron beam enclosed an angle of 64° with the surface normal. Investigations with the STM were performed at 78 K. STM images were recorded at constant current with the bias voltage applied to the sample. The surface of Ir(111) was prepared by Ar^+ bombardment and annealing at 1200 K. Cleanliness was inferred from featureless specular vibrational spectra [Fig. 4.1(a)] and STM images [Fig. 4.1(c)]. Crystalline quality was ensured by sharp Ir(111) low-energy electron diffraction patterns [Fig. 4.1(b)]. Clean Ir(111) surfaces were exposed to H_2Pc (purity 99.99 %) sublimated from a heated Ta crucible at room temperature while CO was adsorbed from the residual gas.

Theoretical Methods

To model experimental data and to keep calculations computationally feasible at the same time, coadsorption of C_6H_6, rather than H_2Pc, and CO on Ir(111) was investigated.[1] Structural, electronic and vibrational properties of selected superstructures were obtained by density functional calculations using the Projector Augmented Wave method [216, 218] as implemented in the Vienna *Ab initio* Simulation Package [248–251] with the dipole correction for the electrostatic potential [252]. The Ir(111) sample was modeled by a five-layer slab. Different C_6H_6 coverages were realized on p(4×4) and p(5×5) Ir(111) unit cells, which both contained a single CO molecule (Appendix F, Section F.1). Each supercell included a vacuum region with a thickness of ≈ 16 Å to ensure negligibly small interactions between neighboring supercells. The Brillouin zones were sampled by $5 \times 5 \times 1$ **k**-point meshes. In order to take van der Waals interactions explicitly into account all calculations were performed with the optB88-vdW exchange correlation functional [253, 254]. The optimization of the geometric structure was performed by freezing the bottom two Ir layers in their bulk positions and by relaxing all other atoms until forces were smaller than 10 meV Å^{-1}. The plane-wave kinetic energy cut-off was 550 eV in all calculations. The Methfessel-Paxton method [255] was employed for performing Brillouin-zone integration with a smearing width of 0.15 eV. Harmonic vibrational energies were calculated using a finite-displacement scheme and the diagonalization of the dynamical matrix. Only adsorbate degrees of freedom were taken into account while Ir atoms were fixed.

4.1 Decrease of the C–O Stretch Mode Vibrational Energy

CO adsorption on Ir(111) from the residual gas led to vibrational spectra as shown in Fig. 4.2(a). In agreement with previous experiments and calculations the loss peaks at 61 meV and 252 meV were assigned to, respectively, Ir–CO and C–O stretch modes for CO residing at Ir(111) on-top sites [256, 257]. Using the energies of the vibrational modes the CO coverage was estimated as ≈ 0.05 ML (ML: monolayer)[2]. Exposing the

[1] Calculations with H_2Pc in periodic structures are computationally expensive. In a first approximation, each H_2Pc molecule may be mimicked by four C_6H_6 molecules which are arranged as the four isoindole groups of H_2Pc. Upon adsorption on Ir(111), the C_6H_6 rings of these isoindole arms chemisorb with the metal substrate [247]. Therefore, adsorption-induced electrostatic dipole moments are most likely located at the C_6H_6 rings. Since this approximation still leads to large supercells, our density functional theory calculations were performed for homogeneously distributed C_6H_6 molecules on Ir(111) to determine the main trends.

[2] One monolayer (ML) of CO is defined by the occupation of all Ir(111) on-top sites with a single CO molecule. The H_2Pc-covered Ir(111) surface reaches 1 ML when the C–O stretch mode spectroscopic signature disappears from specular spectra.

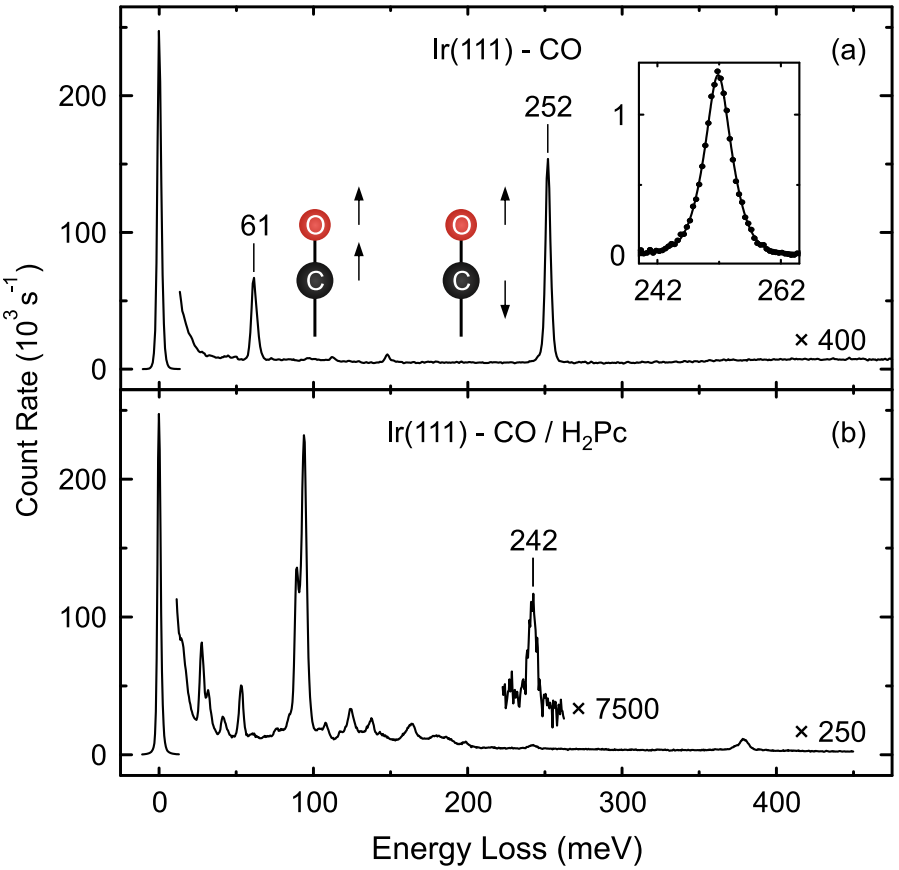

Fig. 4.2: **(a)** Specular electron energy loss spectrum of CO-covered Ir(111). Signatures at 61 meV and 252 meV are due to Ir–CO and C–O stretch modes, respectively [256, 257]. Inset: Close-up view of the C–O stretch mode spectroscopic signature revealing its symmetric line shape. A single Voigt profile was used to fit the raw data from which a linear background had been subtracted. **(b)** Specular electron energy loss spectrum of H_2Pc-covered Ir(111) with coadsorbed CO. The signature at 242 meV is assigned to the shifted C–O stretch mode energy. All other features are due to H_2Pc vibrational modes [247].

CO-covered Ir(111) surface to H_2Pc led to a gradual redshift, *i. e.*, decrease, of the C–O stretch mode energy. Figure 4.2(b) shows a specular loss spectrum of Ir(111)-CO covered with ≈ 1 ML of H_2Pc.[2] According to a previous report H_2Pc vibrations exhibited energies between 0 meV and ≈ 200 meV as well as at ≈ 380 meV [247]. Consequently the Ir–CO stretch mode was hardly discernible from the H_2Pc spectrum. The C–O stretch mode, in contrast, was clearly visible at 242 meV. Its shift from 252 meV observed for the CO-covered Ir(111) surface to 242 meV upon H_2Pc deposition will be discussed next. Moreover, the transition from a symmetric line shape of the C–O stretch mode spectroscopic signature at zero H_2Pc coverage [inset to Fig. 4.2(a)] to an asymmetric profile at higher H_2Pc coverages will be addressed.

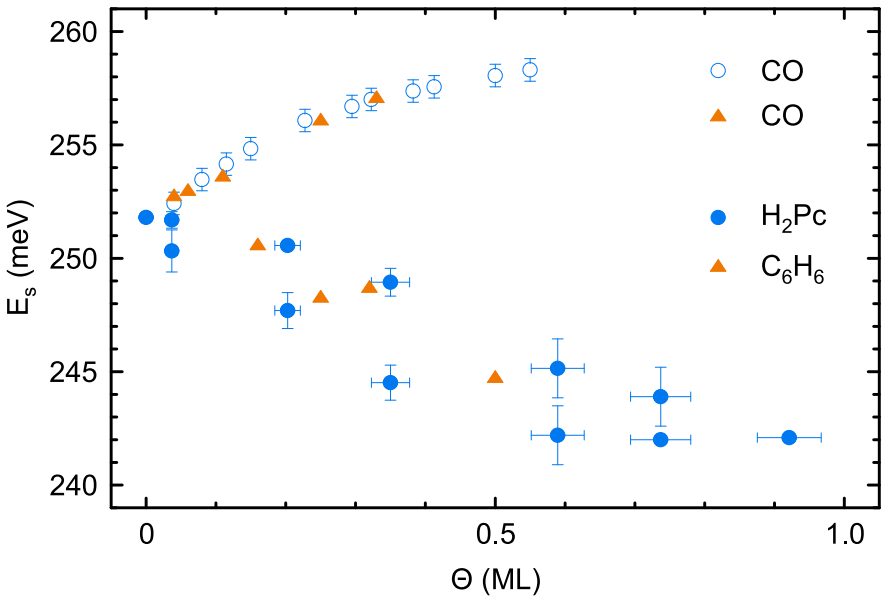

Fig. 4.3: Filled symbols: Variation of C–O stretch mode energy (E_s) with H_2Pc and C_6H_6 coverage (Θ). The CO coverage is ≈ 0.05 ML. Experimental H_2Pc data appear as circles, calculated C_6H_6 data are depicted as triangles. Open symbols: Variation of E_s with CO coverage. Experimental (calculated) data are shown as circles (triangles). Experimental data were adopted from a previous report [256].

Figure 4.3 shows the experimentally observed gradual decrease of the C–O stretch mode energy, E_s, from 252 meV at a H_2Pc coverage of $\Theta = 0$ ML to 242 meV at almost 1 ML (filled circles). For coverages $0\,\text{ML} < \Theta < 1\,\text{ML}$ two data points for E_s appear. They reflect the peak positions of two Voigt profiles, which were necessary to fit the asymmetric line shape of the C–O stretch mode spectroscopic signature (see Section 4.2). Two possible origins to the observed redshift can be excluded. First, the CO coverage during the experiments with increasing exposure of Ir(111) to H_2Pc was ≈ 0.05 ML and almost constant. Therefore, a variation of E_s due to a changing CO coverage is not the origin of the observed redshift. Indeed, increasing CO coverages on a purely CO-covered Ir(111) surface were previously shown to increase E_s (open circles in Fig. 4.3) due to the coupling of CO dynamic dipoles [256]. Our density functional calculations (open triangles in Fig. 4.3) corroborated this scenario. Second, a change in the CO adsorption site may likewise be excluded since previously reported [258] C–O stretch mode energies at Ir(111) bridge (225 meV) and hollow (214 meV) sites are appreciably lower than E_s plotted in Fig. 4.3. In contrast, calculations of E_s for C_6H_6-covered Ir(111) surfaces with coadsorbed CO (filled triangles in Fig. 4.3) coincide with the experimental data. They revealed that the interaction of adsorption-induced electric dipoles causes the observed decrease of E_s.

Tab. 4.1: Calculated dipole moments p_z of C_6H_6 and CO on Ir(111) depending on the adsorbate coverage Θ. The dipole moment of C_6H_6 was determined on Ir(111) covered with a single CO molecule per simulated supercell[3], the dipole moment of CO in the absence of C_6H_6.

C_6H_6		CO	
Θ (ML)	p_z (e Å)	Θ (ML)	p_z (e Å)
0.16	0.734	0.04	-0.050
0.25	0.701	0.06	-0.051
0.32	0.646	0.11	-0.050
0.50	0.552	0.25	-0.045
-	-	0.33	-0.047

In order to elaborate on this scenario, electric dipole moments, p_z, of C_6H_6 and CO were determined using the Helmholtz equation, $\Delta\Phi = -ep_z/(\varepsilon_0 A)$, where $\Delta\Phi$ denotes the adsorbate-induced work function change, e the elementary charge, ε_0 the vacuum permittivity and A the supercell area (Appendix F, Section F.2). The work function changes were determined by comparing the calculated work functions for clean Ir(111), 5.83 eV, with those of Ir(111) covered with C_6H_6, CO and both adsorbates. Positive (negative) p_z are oriented parallel (antiparallel) to the surface normal. According to Tab. 4.1 the C_6H_6 dipole moment[3] is positive and appreciably larger than the CO dipole moment for all considered coverages. In addition, p_z of C_6H_6 decreases strongly with increasing coverage while CO exhibits a virtually constant negative dipole moment. The total electric field of all C_6H_6 dipole moments at a given CO site was evaluated as

$$F_z(\Theta) = -\frac{\Sigma(\Theta)}{4\pi\varepsilon_0} \tag{4.1}$$

using the dipole sum

$$\Sigma(\Theta) = p_z(\Theta)\sigma \tag{4.2}$$

and the lattice sum

$$\sigma = \sum_i r_i^{-3} \tag{4.3}$$

with r_i the lateral distance between a given CO dipole and the ith surrounding C_6H_6 dipole.

[3] In order to determine the dipole moments of C_6H_6 in the coadsorption structure the dipole moments of C_6H_6 on Ir(111) are correlated with their Bader charges. Using a linear fit to the data the dipole moments of C_6H_6 in the coadsorption structure can be evaluated by means of their molecular Bader charges.

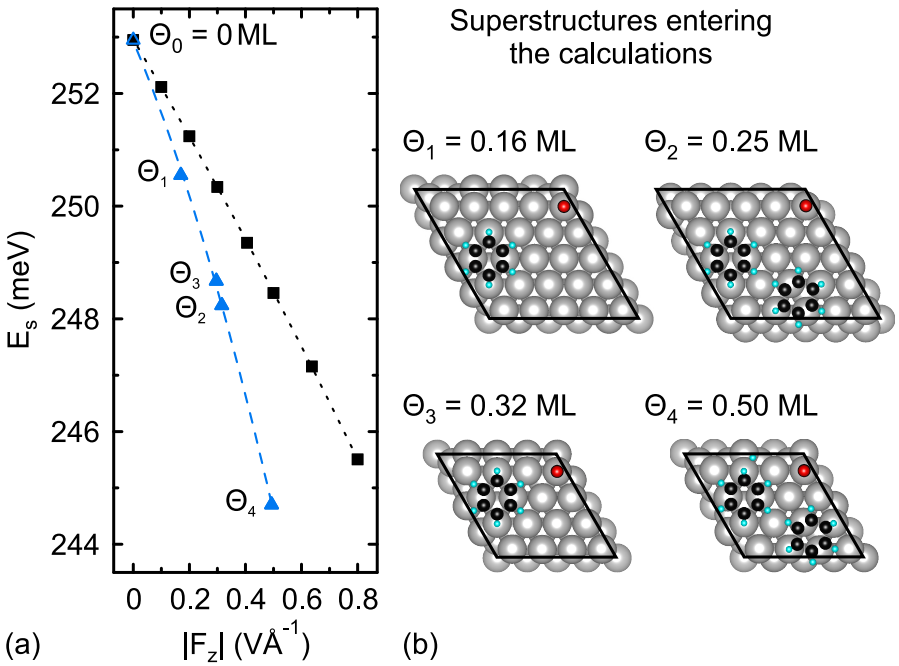

Fig. 4.4: (a) Triangles depict the variation of the C–O stretch mode energy (E_s) as a function of the electric field, F_z, at the CO site for different C_6H_6 coverages Θ_i ($i = 0 \ldots 4$). The electric field was calculated from the coverage-dependent dipole sum [Eq. (4.1)]. It points towards the surface at the CO site. The triangle at Θ_0 corresponds to E_s for one CO on a p(4×4) supercell. Squares show the calculated variation of E_s with an external homogeneous electric field for one CO on a p(4×4) supercell. Dashed and dotted lines present parabolic fits to the data according to Eq. (4.4). **(b)** Sketches of supercell geometries entering the calculations. Supercells are indicated by rhombi. The CO coverage is 0.04 ML (0.06 ML) in the p(5×5) [p(4×4)] supercells. Different C_6H_6 coverages [Θ_i ($i = 0 \ldots 4$)] were considered. All calculated structures were visualized using VESTA [261].

Plotting the calculated E_s as a function of F_z led to the evolution depicted as triangles in Fig. 4.4. The dashed line represents a parabola,

$$E_\mathrm{s}(F_z) = E_\mathrm{s}(0) + \alpha F_z + \beta F_z^2 \tag{4.4}$$

with $E_\mathrm{s}(0)$ the field-free C–O stretch mode energy and α, β two fit parameters. The parabolic behavior of E_s was predicted for CO on Cu(100) in external homogeneous electric fields [259] and confirmed theoretically for CO on (111) surfaces of Pt, Ir, Pd [260]. For CO on Ir(111) our calculations likewise revealed a parabolic behavior (squares and dotted line in Fig. 4.4).

In additional calculations we went beyond the approximation of the C_6H_6 dipole as a point dipole and took the lateral extension of the molecule into account. To this end, the C_6H_6-induced change in the electrostatic potential was determined by

$\Delta V(x,y,z) = V_{\mathrm{Ir(111)+C_6H_6}} - V_{\mathrm{Ir(111)}}$, with $V_{\mathrm{Ir(111)+C_6H_6}}$ the electrostatic potential of C_6H_6 adsorbed on Ir(111) and $V_{\mathrm{Ir(111)}}$ that of the clean Ir(111) surface. The corresponding electric field was evaluated as $-\partial\left[\Delta V(x_{\mathrm{CO}}, y_{\mathrm{CO}}, z)\right]/\partial z$ at the lateral position $(x_{\mathrm{CO}}, y_{\mathrm{CO}})$ of CO in the coadsorbate structure. We found that the electric field at the CO center yielded a similar F_z as derived from the sum of point dipoles [Eq. (4.1)].

According to previous calculations [259, 262] the dominant contribution to the change in $E_{\mathrm{s}}(F_z)$ is due to the field-induced variation of the C–O equilibrium distance, which is adopted at $F_z = 0$. This result could also be confirmed for our system. Calculating E_{s} with the geometry of the coadsorption structure but in the absence of C_6H_6 and without further relaxation led to virtually identical C–O stretch mode energies, which differ by less than 0.1 meV from those of the complete coadsorption systems. According to a Bader charge analysis [263, 264] the C (O) atom of adsorbed CO possesses a positive (negative) partial charge of +1.0 e (−1.1 e). Therefore, the electric field of C_6H_6 which points towards the surface at the CO site exerts a force on the positively charged C atom that is directed towards the surface and an oppositely directed force on the negatively charged O atom. As a result the C–O bonding distance is increased and thus the C–O stretch mode energy is decreased. An increase of the C–O bond length by 1 pm is accompanied by a decrease of E_{s} by ≈ 8 meV. This scenario is compatible with the Badger rule, which states the decrease (increase) of the bond force constant in a diatomic molecule with the increase (decrease) of the intermolecular distance [265].

Other possible origins to the decrease of E_{s} with increasing C_6H_6 coverages were considered in the calculations. In Appendix F, Section F.3, we show that the coupling of dynamic dipole moments, the intermolecular charge transfer and the C_6H_6-induced deformations of the Ir(111) surface exhibit minor impact on E_{s} compared with the static dipole interaction. Therefore, the presented findings evidence the major role of electrostatic dipole interactions in decreasing the C–O stretch mode energy.

4.2 Asymmetry of the C–O Stretch Vibrational Mode

The second experimental result, *i. e.*, the occurrence of an asymmetric line shape of the C–O stretch mode spectroscopic signature in the presence of H_2Pc on Ir(111), is consistent with the static dipole interaction, too. Without adsorbed H_2Pc the C–O stretch mode spectral feature appeared with a symmetric line shape [inset to Fig. 4.2(a)]. Adsorption of H_2Pc led to an asymmetric line shape as shown in Figs. 4.5(a)–(c) for different coverages. The experimental data were best described by a fit with two Voigt profiles, which indicated the presence of additional vibrational features in a narrow energy range below 252 meV. Since the maxima of the Voigt profiles were separated

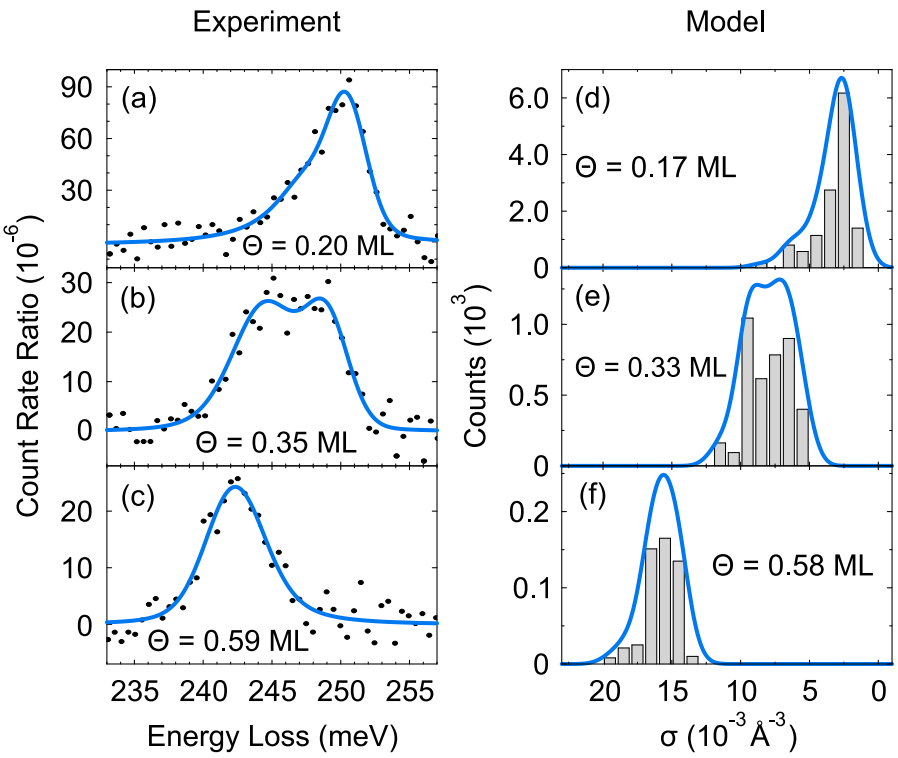

Fig. 4.5: (a)–(c) Specular spectra of the C–O stretch mode at the indicated H_2Pc coverages. Raw data were divided by the count rate of the elastic peak. The full lines represent fits to the data by two Voigt profiles. **(d)–(f)** Histograms of lattice sums, σ [Eq. (4.3)], for the indicated C_6H_6 coverages. Full lines represent continuous distributions of σ according to Eq. (4.5).

by less than 5 meV different CO adsorption sites can be excluded as the origin to the additional vibrational modes (see Section 4.1). Rather, we propose that different H_2Pc–CO distances at a given H_2Pc coverage in the submonolayer regime cause the asymmetric line shape. The probing electron beam in electron energy loss spectroscopy covers a good part of the sample surface and gives rise to laterally averaged spectra. In particular, vibrational energies of CO molecules with different distances to H_2Pc molecules are measured. Different H_2Pc–CO distances correspond to different electric dipole fields at the CO sites. Therefore, we attribute the asymmetric line shapes observed in vibrational spectra of the C–O stretch mode to the lateral average of vibrational features with different energies.

To test this proposal histograms of the lattice sum, σ, were calculated for different C_6H_6 coverages [Figs. 4.5(d)–(f)]. In the calculations the static dipole field of H_2Pc was simulated by the superposition of dipole fields originating from 4 C_6H_6 molecules, which were arranged on Ir(111) to mimic the 4 isoindole groups of H_2Pc. In addition, the rotational degree of freedom, *i. e.*, the occurrence of H_2Pc molecules rotated by

60° with respect to each other was included in the calculations. The CO molecule was positioned at on-top sites of Ir(111). For different C_6H_6 coverages $\sigma(r_i)$ was then calculated. Here, r_i denotes the lateral distance between the CO site and the center of C_6H_6 molecules. All r_i were chosen such as to guarantee C–CO distances larger than 4.7 Å. Our density functional calculations (Appendix F, Section F.1) revealed that distances between CO and the closest C atom of a C_6H_6 molecule lower than 4.7 Å were energetically unfavorable. Depending on the C_6H_6 coverage different histograms of σ were found [Figs. 4.5(d)–(f)]. These histograms are directly comparable with the experiment since our calculations suggested a linear correlation between E_s and σ (not shown).[4] In order to facilitate the comparison with the experimental spectra, continuous distributions of σ, $C(\sigma)$ [blue lines in Figs. 4.5(d)–(f)], were determined by

$$C(\sigma) = \sum_i 2\frac{c_i}{\sqrt{2\pi}} \exp\left[-\frac{(\sigma-\sigma_i)^2}{2\delta^2}\right] \tag{4.5}$$

with c_i (σ_i) the counts (lattice sum) of the ith bin of the histogram and $\delta = 0.85\times10^{-3}$ Å^{-3} a broadening parameter. These distributions exhibit the same characteristic line shape as the spectroscopic signature of the C–O stretch mode [Figs. 4.5(a)–(c)] at a similar coverage. In particular, asymmetric distributions at 0.17 ML [Fig. 4.5(d)] and at 0.58 ML [Fig. 4.5(f)] were calculated as well as a double-peak structure at 0.33 ML [Fig. 4.5(e)]. At higher coverages $C(\sigma)$ as well as the line profile of the C–O stretch mode signature became symmetric again. This evolution is expected since the number of allowed CO sites for evaluating σ decreases with increasing C_6H_6 coverage. Concomitantly, the distances of CO to adjacent C_6H_6 (H_2Pc) molecules become similar.

Summary and Conclusions

In this study, CO molecules serve as subtle probes for dipole interactions on Ir(111). From the energy variation and the spectroscopic line shape of the C–O stretch mode electrostatic dipole coupling to H_2Pc molecules on Ir(111) is singled out as the dominant interaction mechanism. In addition, the influence of dynamic dipole coupling, intermolecular charge transfer and adsorbate-induced substrate deformations on the C–O stretch mode energy is quantified. Functionalizing tips with a single CO molecule in forthcoming STM experiments and detecting changes in CO vibrational energies via inelastic tunneling spectroscopy may serve as a sensitive force sensor.

[4] While E_s varies quadratically with the dipole sum $\Sigma(\Theta)$ [Eqs. (4.1)–(4.4), Fig. 4.4] the evolution of E_s with the lattice sum σ [Eq. (4.3)] may deviate from the quadratic behavior due to the missing factor of the coverage-dependent electric dipole moment [Eq. (4.2)].

Conclusion and Perspectives

The present thesis was devoted to the exploration of the dynamical properties of phthalocyanines and graphene on Ir(111) surfaces. The first part of the studies was aimed at investigating the phonons properties of graphene on Ir(111). For this purpose, a single layer of graphene was epitaxially grown on Ir(111) with a high structural homogeneity and with a single rotation domain. The high crystalline quality has been demonstrated by low-energy electron diffraction pattern. Here, each Ir(111) diffraction spot was surrounded by an extended hexagonal array of satellite spots which are due to the moiré superstructure. In addition, the high quality could be confirmed by representative scanning tunneling microscopy images which show atomic resolution at liquid helium temperatures. Due to the well-defined homogeneity in all crystallographic directions the dynamical properties of graphene could be determined with high precision. To this end, the phonon dispersion relation of graphene on Ir(111) has been acquired by means of angle-resolved inelastic electron scattering. In the course of the experiments, the electron impact energy was varied to enhance the scattering cross section for specific phonon branches. The resulting dispersion relation shows a high degree of similarity to the dispersion curves of free graphene. However, the adsorption of graphene on Ir(111) leaves its clear fingerprints in the phonon dispersion relation. From experiments and supporting density functional theory calculations two remarkable and new scientific insights could be derived, which will be summarized below.

(a) Screening of Electron-Phonon Coupling in Graphene on Ir(111)
As in the case of pristine graphene and graphite, the phonon dispersion relation of graphene on Ir(111) shows Kohn anomalies at the $\bar{\Gamma}$ and $\bar{\mathrm{K}}$ point of the surface Brillouin zone. Unexpectedly, however, the Kohn anomaly of the highest optical phonon branch at $\bar{\mathrm{K}}$ is weaker than observed for pristine graphene or graphite. This observation is rationalized in terms of a reduced electron-phonon coupling. The reduction originates from a screening of graphene electron correlations due to the presence of the metal substrate. Furthermore, such a screening mechanism efficiently damps correlations effects that are not captured by standard density functional calculations. As a result, it renders local exchange-correlation functionals precise enough for modeling phonon dispersion relations of graphene on metal surfaces with a weak graphene–metal interaction.

(b) Moiré-Induced Replica of Graphene Phonons on Ir(111)
The second finding is related to the moiré superstructure of graphene on Ir(111) which is, for instance, reflected in scanning tunneling microscopy images by a periodic variation of the surface topography. However, the superstructure not only leaves its fingerprints in the topographical but also in the dynamical properties. Our investigations into the phonon dispersion of graphene on Ir(111) uncovered additional phonon branches that had not been reported by experiments or calculations so far. Calculations for a linear chain of C atoms attached to an infinitely heavy substrate revealed that imposing a superstructure by periodically varying the C–C interaction and the C–substrate coupling induces replicated phonons. The phonon replica occurred at wave vectors of the moiré superstructure, *i. e.*, their reciprocal distance to the original phonon branches depends on the considered high symmetry direction. In other systems, where the superstructure is strongly coupled to the substrate, backfolding of phonon branches could be observed [266–268]. Here, the existing range is extended by a system, where the superstructure is weakly coupled to the substrate and, thus, the phonon branches are replicated.

The presented results suggested a weak but finite graphene–Ir interaction. In this context the second part of the studies was dedicated to the question whether graphene on Ir(111) acts as a buffer layer that efficiently decouples molecules from the metallic substrate. To demonstrate a possible decoupling most clearly, metal-free and manganese phthalocyanines were deposited both on pristine and on graphene-covered Ir(111) surfaces. From a combination of scanning tunneling microscopy and vibrational spectroscopy two further exciting and new scientific insights could be derived.

(c) Decoupling of Phthalocyanines from Ir(111) by Interjacent Graphene
From a comparison of scanning tunneling microscopy images of individual phthalocyanine molecules adsorbed to the different surfaces alone it was difficult to discern potential differences in the molecular adsorption geometry. However, spectroscopic rather than microscopic data contained valuable structural information. Vibrational spectroscopy using inelastic electron scattering unequivocally hinted at considerable deformations of the free-molecule structures on Ir(111) and at a reduction of their molecular symmetry. In contrast, phthalocyanines adsorbed to graphene retained their planar vacuum structure. This behavior has been demonstrated both for metal-free phthalocyanines and manganese phthalocyanines. Density functional theory calculations confirmed the suggested scenario and revealed a chemisorption of phthalocyanines on Ir(111) and a physisorption on graphene. As a consequence, graphene on Ir(111) acts as an interjacent buffer layer that efficiently reduces the phthalocyanine–Ir hybridization.

(d) CO as a Molecular Probe for Electrostatic Dipole Interactions at Surfaces
Furthermore, using vibrational spectroscopy, we showed that carbon monoxide from the residual gas adsorbs on clean Ir(111) surfaces at room temperature. The Ir–C and C–O stretch vibrational modes left spectroscopic signatures at 61 meV and 252 meV, respectively. By coadsorbing increasing coverages of metal-free phthalocyanine molecules, the C–O stretch vibrational energy exhibited a gradual decrease of 10 meV. Supporting density functional theory calculations rationalized the experimental observation in terms of static electric dipole interactions between CO and phthalocyanines dipoles. In contrast to previous investigations we were able to single out the effect of solely a single interaction on the vibrational properties of CO. Our calculations revealed that changes in the vibrational energy due to dynamic dipole coupling, charge transfer processes and adsorbate-induced atomic relaxations of the substrate are negligible compared to the static dipole-dipole interaction. Moreover, for phthalocyanine coverages in the submonolayer range the spectroscopic signature of the C–O stretch mode exhibited an asymmetric line shape. This observation is consistent with the suggested electrostatic dipole interaction and reflects its distance dependence. So, carbon monoxide on Ir(111) can act as molecular probe for electrostatic dipole fields originating from organic molecules. In the rapidly growing field of scanning probe experiments, subtle probes are relevant for various interactions at surfaces. Functionalizing the tip of a scanning tunneling microscope with a single CO molecule and determining its vibrational energies by inelastic electron tunneling may be used to probe interactions at the atomic scale.

Among the presented studies further exciting experiments and calculations are conceivable to explore the dynamical properties of atoms, molecules and two-dimensional layers on surfaces. In our investigations regarding graphene on Ir(111), a weak graphene–Ir interaction was inferred from the phonon dispersion relation around $\bar{\Gamma}$. Lately, it has been demonstrated that the graphene–Ir interaction can be further reduced by oxygen intercalation [269, 270]. Furthermore, intercalation has been utilized to vary the doping level of graphene on Ir(111) [271–276]. These specific manipulations of the chemical environment of graphene might not only have an impact on the geometrical and electrical properties, but also on the dynamical properties. Phonons, for example, play a crucial role in the predicted superconductivity of lithium-covered graphene [277], which has been demonstrated experimentally quite recently [278]. Therefore, further research into the dynamics of graphene in dependence of the intercalated species would be highly desirable. Likewise, the extension of the linear chain model, which was used for the rationalization of the phonon replica, provides an incentive. A two-dimensional model or *ab initio* calculations could lead to new insights.

Another possible field of research is associated with the interaction between graphene and adsorbed molecules. Using ion bombardment, single carbon vacancies can be created in graphene on metal surfaces [279, 280]. Here, the question arises whether these vacancies are preferred adsorption sites for phthalocyanines which are deposited on graphene. For clarification, scanning tunneling microscopy studies are suitable. If the phthalocyanines primarily adsorb at the vacancies, experiments with vibrational spectroscopy could be performed to identify a possible alteration of the spectroscopic lines shapes of the molecular vibrations. In addition, exciting effects could also occur between the postulated magnetic moment of the vacancies in the graphene lattice [281, 282] and the molecular magnetic moment of manganese phthalocyanines [223]. For this, experiments with spin-resolved scanning tunneling microscopy and spectroscopy at liquid helium temperatures are appropriate. Research into the magnetic properties of graphene attracts rising attention since layered carbon materials could be alternative materials for improved spintronic devices [281].

Appendix

A Mass Spectra

In order to verify the cleanliness of the ultrahigh vacuum chambers and to analyze the composition of the residual gas mass spectra were acquired with a quadrupole mass spectrometer. Figure A.1 shows the mass spectra of the preparation [Fig. A.1(a)] and the analysis chamber [Fig. A.1(b)] which were recorded at a chamber base pressure of 10^{-9} Pa. In addition, the purity of the gases used for the Ar^+ bombardment and for the growth of graphene was checked. The corresponding mass spectra of argon [Fig. A.2(a)] and ethene [Fig. A.2(b)] were obtained at partial pressures of 5×10^{-4} Pa and 3×10^{-5} Pa, respectively. In all spectra, mass-to-charge ratios are given in units of the unified atomic mass $u = 1/12 \cdot m(^{12}C)$ divided by the elementary electric charge e.

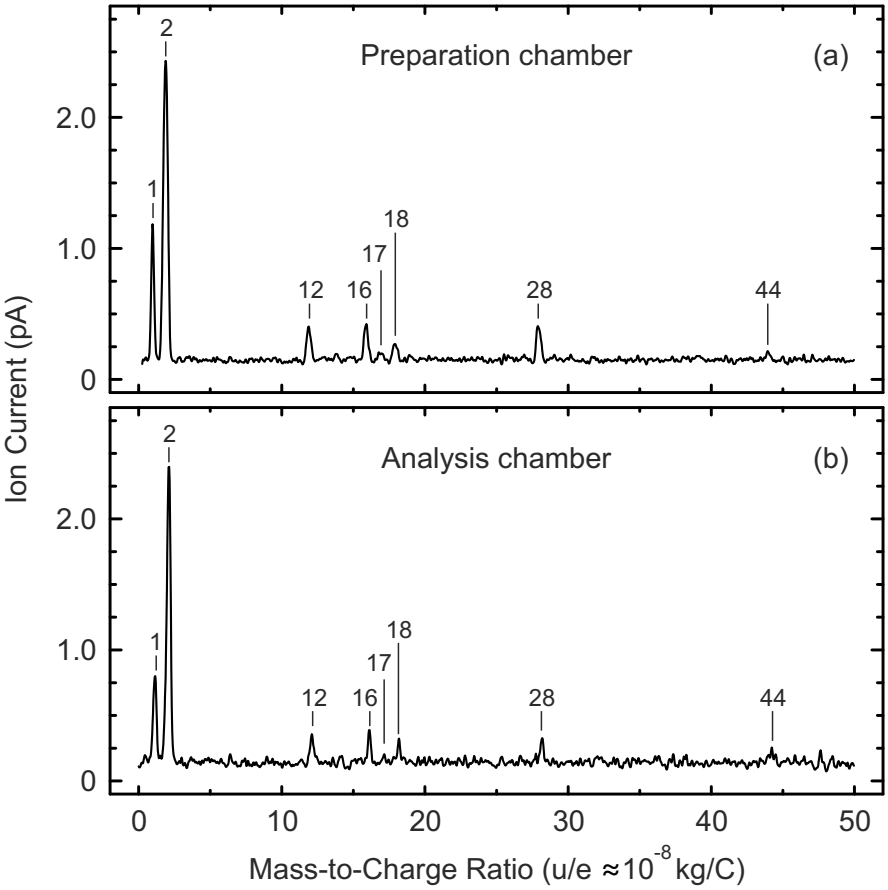

Fig. A.1: Mass spectra of **(a)** the preparation chamber and **(b)** the analysis chamber, both acquired at a chamber base pressure of 10^{-9} Pa. Spectroscopic signatures at mass-to-charge ratios of 1 (2, 12, 16, 17, 18, 28, 44) are due to H^+ (H_2^+, C^+, O_2^+, OH^+, H_2O^+, CO^+, CO_2^+) indicating residuals of hydrogen and extremely low amounts of water, carbon monoxide, and carbon dioxide.

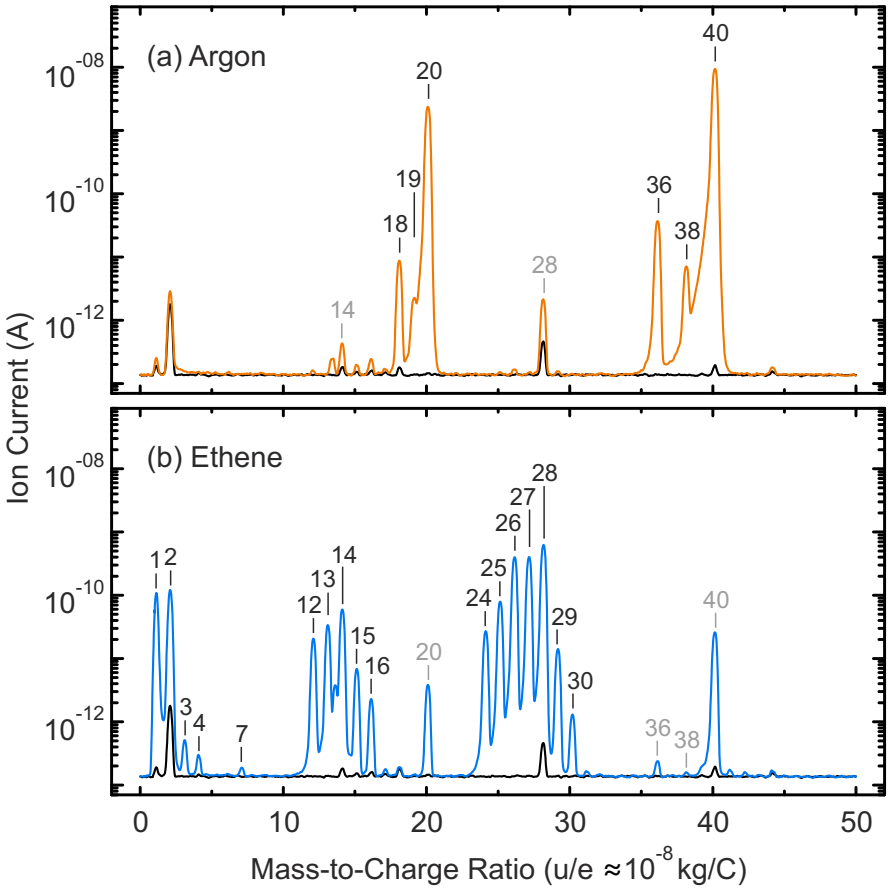

Fig. A.2: Mass spectra of **(a)** argon (orange) and **(b)** ethene (blue) acquired at partial pressures of 5×10^{-4} Pa and 3×10^{-5} Pa, respectively. For the purpose of comparison, the mass spectrum of the preparation chamber (black) acquired at chamber base pressure is shown. Spectroscopic signatures in (a) at mass-to-charge ratios of 18, 19, 20, 36, 38, 40 are due to $^{36}Ar^{++}$, $^{38}Ar^{++}$, $^{40}Ar^{++}$, $^{36}Ar^{+}$, $^{38}Ar^{+}$, $^{40}Ar^{+}$ and reflect the natural isotope ratio of argon. Features at 14 and 28 indicate extremely small traces of nitrogen (N^+, N_2^+). Spectroscopic signatures in (b) at mass-to-charge ratios of 1–4, 7, 12–16, 24–30 are most probably due to $^{1}H^{+}$, $^{1}H_2^{+}$, $^{2}H^{+}$, $^{2}H_2^{+}$, $(^{12}CH_2)^{++}$, $(^{12}CH_y)^{+}$, $(^{13}CH_y)^{+}$, $(^{12}C_2H_y)^{+}$, $(^{13}C_2H_y)^{+}$ and reflect the typical fragments of ethene with natural isotope ratios of carbon and hydrogen. Features at 20, 36, 38, 40 indicate small traces of argon ($^{40}Ar^{++}$, $^{36}Ar^{+}$, $^{38}Ar^{+}$, $^{40}Ar^{+}$).

B Fine-Tuning of the Spectrometer

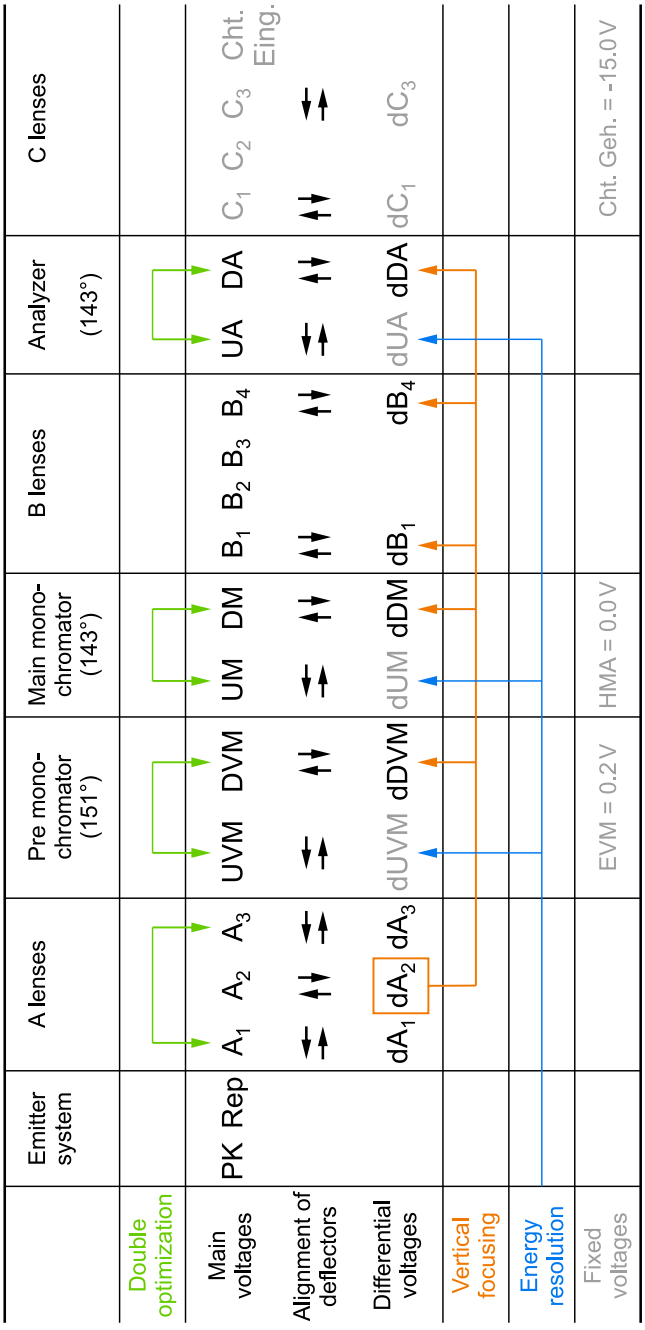

Fig. B.1: Simplified representation of the voltages of an Ibach spectrometer grouped by the spectrometer components. Black (grey) colored voltages are varied (remain constant) during a standard optimization. Specific optimization procedures and the adjustment of the energy resolution are indicated by green, orange and blue color, respectively. For further information, please refer to the text.

Figure B.1 shows the voltages of an Ibach spectrometer grouped by the spectrometer components. Prior to each measurement the majority of the voltages have to be optimized (black) while the others are typically fixed (gray). Below, some approaches and hints are listed which might be helpful during the fine-tuning of the spectrometer. These are intended to supplement previous findings [131] and are based on recent numerical simulations of H. Ibach [133] and on experience.

- During a **standard optimization** the black colored voltages in Fig. B.1 are varied starting with the voltages of the emitter system and ending with those of the analyzer. In the case of electrostatic lenses or deflectors which consist of a main and a differential voltage, first the main voltage is optimized. Here, optimization is equivalent to the variation of one voltage until the count rate reaches its maximum.

- In particular after bake-out, it may be advantageous to perform a **double optimization** which sometimes results in an increased count rate. This procedure refers to specific voltage pairs (indicated by green arrows in Fig. B.1). For the optimization, the first voltage of a pair is set to a lower or higher value and the second voltage is varied until the count rate reaches its maximum. The final voltage configuration can be adopted when the count rate is higher than before the double optimization procedure.

- The energy resolution of the spectrometer is adjusted by the voltages dUVM, dUM, and dUA (indicated by blue arrows in Fig. B.1). Appropriate 3-tuples along with the available resolution can be obtained from [131, p. 67]. In addition, the energy resolution depends on the **vertical focusing** of the electron beam. A possible improvement of the resolution can be achieved by reducing the voltage dA2 and a subsequent variation of dDVM, dDM, dB_1, dB_4, dDA (indicated by orange arrows in Fig. B.1) until the count rate reaches its maximum. The determination of the full width at half maximum after each optimization step is recommended.

- During the optimization of the B lenses, typically, a symmetrical lens adjustment is striven for, *i. e.*, $B_1 \approx B_4$ and $B_2 \approx B_3$. However, recent simulations [133] demonstrate that the count rate at the detector can be considerably increased by using (a) a new operation mode with higher lens voltages and (b) a specific asymmetrical lens adjustment. For further details, please refer to [133].

- Equivalent voltages of the main monochromator and the analyzer should also be symmetric, *i.e.*, UM ≈ UA, DM ≈ DA, and dDM ≈ dDA.

- The C lenses should be only optimized after a replacement of the channeltron.

C Linear Chain Model for Out-of-Plane Phonons

In Section 2.3, a simple one-dimensional force-constant model is presented for the calculation of an out-of-plane acoustic phonon. Here, some calculation steps regarding the basic model with spatially uniform spring constants and the extended model with periodically varying spring constants are explained in more detail.

C.1 Spatially Uniform Spring Constants

For the derivation of Eq. (2.1) we start with Newton's second law. Taking nearest $(n \pm 1)$ and next-nearest $(n \pm 2)$ neighbors into account, the equation of motion reads

$$m\frac{d^2u_n}{dt^2} = \frac{4\gamma}{a^2}\left[u_{n-1} + u_{n+1} - 2u_n\right] - \frac{\gamma}{a^2}\left[u_{n-2} + u_{n+2} - 2u_n\right] - \alpha u_n \tag{C.1}$$

with u_n the displacement of atom n and t the time. Substituting the plane-wave Ansatz $u_n(x,t) = u_0 \exp(iqx)\exp(i\omega t)$ into Eq. (C.1) results in

$$\begin{aligned} -m\omega^2 u_n(x,t) = &+ \frac{4\gamma}{a^2}\left[\exp(-iqa) + \exp(iqa) - 2\right] u_n(x,t) \\ &- \frac{\gamma}{a^2}\left[\exp(-2iqa) + \exp(2iqa) - 2\right] u_n(x,t) \\ &- \alpha u_n(x,t). \end{aligned} \tag{C.2}$$

Using the identities $\exp(i\tilde{x}) + \exp(-i\tilde{x}) = 2\cos(\tilde{x})$ and $\cos(2\tilde{x}) = 2\cos^2(\tilde{x}) - 1$, Eq. (C.2) can be simplified and the phonon dispersion $\omega(q)$ is given by

$$\begin{aligned} \omega^2(q) &= \frac{4\gamma}{ma^2}\left[-2\cos(qa) + 2\right] + \frac{\gamma}{ma^2}\left[2\cos(2qa) - 2\right] + \frac{\alpha}{m} \\ &= \frac{4\gamma}{ma^2}\left[1 - 2\cos(qa) + \cos^2(qa)\right] + \frac{\alpha}{m} \\ &= \frac{4\gamma}{ma^2}\left[1 - \cos(qa)\right]^2 + \frac{\alpha}{m}. \end{aligned} \tag{C.3}$$

C.2 Periodically Varying Spring Constants

To account for different C–C and C–Ir bond strengths within the supercell of graphene on Ir(111), modulations of α and γ, *i.e.*, α_n and γ_n, have been introduced. Consequently, the uniform spring constants C_1 and C_2 change to periodically varying spring constants

$$\begin{aligned} C_1 \rightarrow C_n^1 &= \frac{4}{a^2}\left[\gamma + \Delta\gamma\cos^2\left(\frac{\pi}{N}n\right)\right] \\ C_2 \rightarrow C_n^2 &= -\frac{1}{a^2}\left[\gamma + \Delta\gamma\cos^2\left(\frac{\pi}{N}n\right)\right]. \end{aligned} \tag{C.4}$$

In order to calculate the phonon dispersion we have to solve an eigenvalue problem, *i.e.*, we have to determine the solution of the equation $D(q) \cdot u_n(q) = \omega_n^2(q) \cdot u_n(q)$, where $D(q)$ is the $N \times N$ dynamical matrix, $u_n(q)$ the n-th eigenvector of length N, and $\omega_n^2(q)$ the n-th eigenvalue. Using Eq. (C.2) the elements of the dynamical matrix are given by

$$\begin{aligned} D_n^{-2} &= -\frac{1}{m} \cdot C_n^2 \cdot \exp(-2iqa) \\ D_n^{-1} &= -\frac{1}{m} \cdot C_n^1 \cdot \exp(-iqa) \\ D_n^0 &= -\frac{1}{m} \cdot \left(-2C_n^1 - 2C_n^2 - \alpha_n\right) \\ D_n^1 &= -\frac{1}{m} \cdot C_n^1 \cdot \exp(iqa) \\ D_n^2 &= -\frac{1}{m} \cdot C_n^2 \cdot \exp(2iqa) \end{aligned} \tag{C.5}$$

where D_n^0 includes the restoring forces that are exerted on atom n, and D_n^1, D_n^{-1} and D_n^2, D_n^{-2} those on the nearest and next-nearest neighbors, respectively. With these elements the dynamical matrix reads

$$D(q) = \begin{pmatrix} D_1^0 & D_1^1 & D_1^2 & 0 & 0 & 0 & 0 & 0 & D_1^{-2} & D_1^{-1} \\ D_2^{-1} & D_2^0 & D_2^1 & D_2^2 & 0 & 0 & 0 & 0 & 0 & D_2^{-2} \\ D_3^{-2} & D_3^{-1} & D_3^0 & D_3^1 & D_3^2 & 0 & 0 & 0 & 0 & 0 \\ 0 & D_4^{-2} & D_4^{-1} & D_4^0 & D_4^1 & D_4^2 & 0 & 0 & 0 & 0 \\ 0 & 0 & D_5^{-2} & D_5^{-1} & D_5^0 & D_5^1 & D_5^2 & 0 & 0 & 0 \\ 0 & 0 & 0 & D_6^{-2} & D_6^{-1} & D_6^0 & D_6^1 & D_6^2 & 0 & 0 \\ 0 & 0 & 0 & 0 & D_7^{-2} & D_7^{-1} & D_7^0 & D_7^1 & D_7^2 & 0 \\ 0 & 0 & 0 & 0 & 0 & D_8^{-2} & D_8^{-1} & D_8^0 & D_8^1 & D_8^2 \\ D_9^2 & 0 & 0 & 0 & 0 & 0 & D_9^{-2} & D_9^{-1} & D_9^0 & D_9^1 \\ D_{10}^1 & D_{10}^2 & 0 & 0 & 0 & 0 & 0 & D_{10}^{-2} & D_{10}^{-1} & D_{10}^0 \end{pmatrix} \tag{C.6}$$

The phonon dispersion relation in Fig. 2.7(b) was obtained by numerical diagonalization of $D(q)$ for all wave vectors $0 \leq q \leq \pi a^{-1}$ and with a step width of $\Delta q = (\pi a^{-1})/200$.

D Vibrational Spectra of Phthalocyanines on Graphene

According to Section 3.1, specular spectra of H_2Pc on Ir(111) show various loss signatures in energy ranges $53\,\text{meV} < E < 84\,\text{meV}$ and $E > 117\,\text{meV}$, while these energy intervals are depleted in specular spectra of H_2Pc adsorbed to graphene. Here, we will show that the absence of vibrational features does not arise from low scattering cross sections or from low scattering intensities.

D.1 Energy Dependence

In order to exclude a possible effect of the scattering cross section, in Fig. D.1 specular electron energy loss spectra of H_2Pc adsorbed to graphene have been acquired in dependence of the impact electron energy, *i. e.* at 3.5 eV (black line), at 6.0 eV (blue line), at 8.5 eV (green line), and at 11.0 eV (orange line). The H_2Pc coverage was identical in all spectra. However, apart from intensity variations which can be clearly discriminated in the inset to Fig. D.1, no spectroscopic signatures appear in the aforementioned energy intervals.

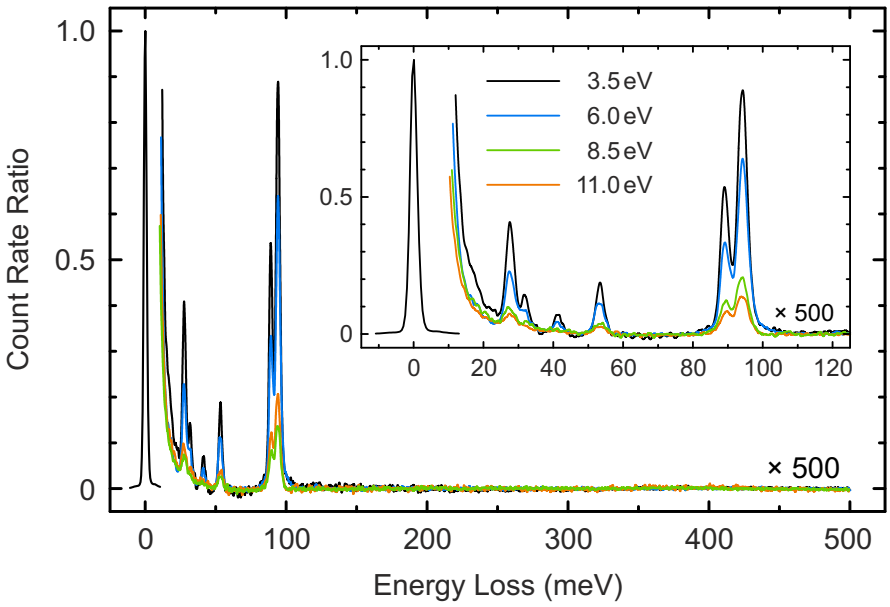

Fig. D.1: Specular electron energy loss spectra of H_2Pc adsorbed to graphene on Ir(111) in dependence of the impact electron energy, as indicated. All spectra were acquired at a constant coverage after a deposition time of 180 s. The energy resolution of the spectrometer was set to 2.5 meV. Data obtained with impact electron energies of 3.5 eV, 6.0 eV, 8.5 eV, 11.0 eV were divided by the count rate of the zero-energy peak, *i.e.*, by $190 \times 10^3\,\text{s}^{-1}$, $180 \times 10^3\,\text{s}^{-1}$, $260 \times 10^3\,\text{s}^{-1}$, $220 \times 10^3\,\text{s}^{-1}$, respectively. To ensure that vibrational signatures can be compared most clearly among the spectra, an exponential background has been subtracted from each spectrum. Inset: Close-up view of the energy loss range below 125 meV.

D.2 Coverage Dependence

Furthermore, to rule out a possible effect of the scattering intensity, in Fig. D.2 specular electron energy loss spectra of H_2Pc adsorbed to graphene have been obtained as a function of the H_2Pc coverage while the impact electron energy was set to 6.0 eV. Submonolayer coverages were grown by varying the deposition time in a range from 20 s (black line) to 180 s (blue line). An increase in the coverage results in a gradual rise of the existing loss features (inset to Fig. D.2), but no additional spectroscopic signatures emerge.

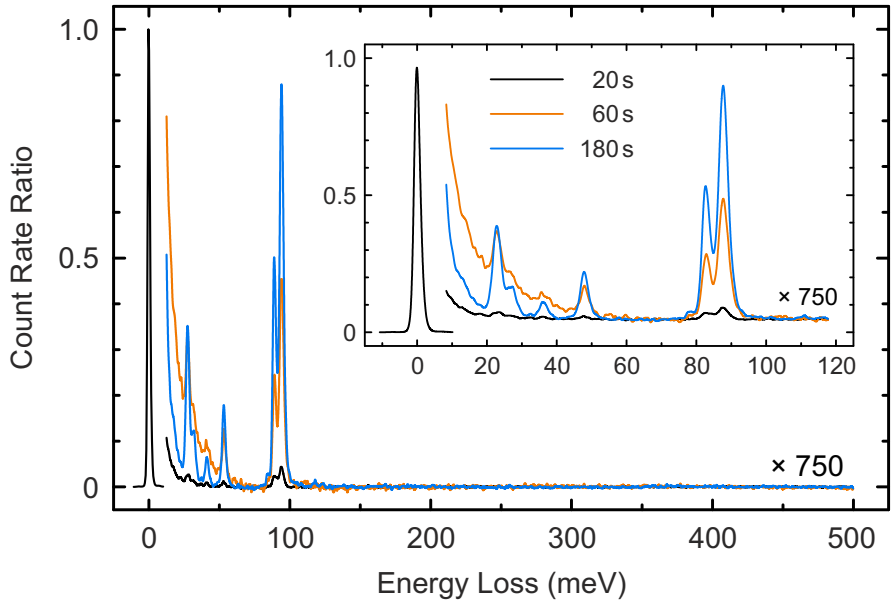

Fig. D.2: Specular electron energy loss spectra of H_2Pc adsorbed to graphene on Ir(111) in dependence of the H_2Pc deposition time, as indicated. All spectra were acquired with an impact electron energy of 6.0 eV and with an energy resolution of 2.5 meV. Data obtained with deposition times of 20 s, 60 s, 180 s were divided by the count rate of the zero-energy peak, *i.e.*, by $250 \times 10^3\,s^{-1}$, $250 \times 10^3\,s^{-1}$, $200 \times 10^3\,s^{-1}$, respectively. To ensure that vibrational signatures can be compared most clearly among the spectra, an exponential background has been subtracted from each spectrum. Inset: Close-up view of the energy loss range below 125 meV.

E Normal Modes of Free Phthalocyanines

In order to be able to assign spectroscopic signatures in experiments with phthalocyanines to concrete molecule vibrations, the normal modes of free H_2Pc [Fig. E.1(a)] and MnPc [Fig. E.1(b)] have been calculated. Along with the vibrational energies of all normal modes, their individual displacement pattern and irreducible representations are given.

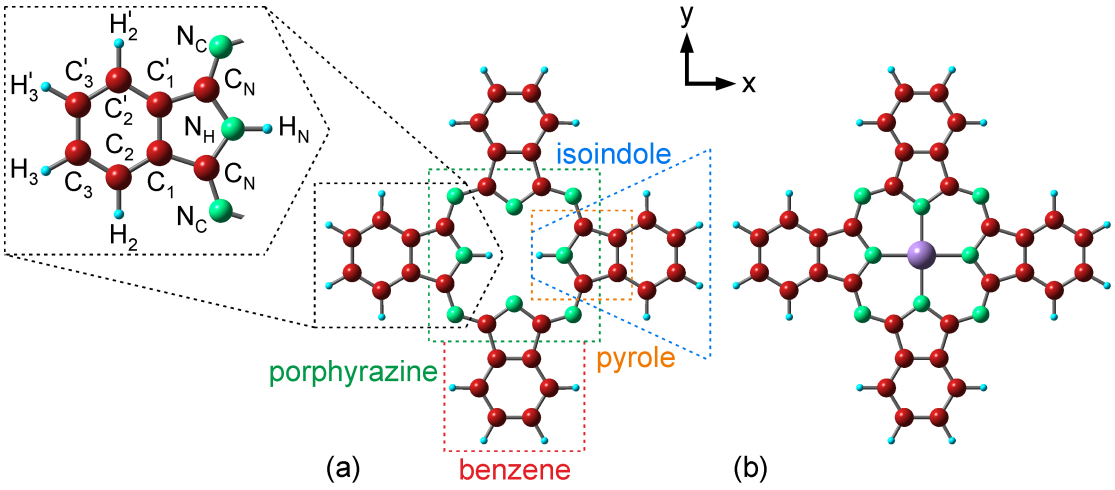

Fig. E.1: Relaxed geometries of **(a)** free H_2Pc and **(b)** free MnPc with indicated Cartesian axes x, y. The z-axis is oriented perpendicular to the xy-plane. H, C, N, Mn atoms appear as light blue, red, green, and violet spheres, respectively. Specific atoms and molecule groups are labeled.

To this end we will briefly introduce some basic concepts of group theory, which will be used in the following sections.

- A **symmetry element** is a point, line or plane about which a symmetry operation can be performed. Typical symmetry elements are identities, inversion centers, axes of rotation, mirror planes and rotation-reflection axes.
- A **symmetry operation** is a permutation of atoms which transforms the molecule arrangement in a state indistinguishable from the initial state. Typical symmetry operations are identities E, inversions I, proper (C_n^m) and improper (S_n^m) rotations[1], and reflections $\{\sigma_h, \sigma_v, \sigma_d\}$[2]. Each symmetry operation can be represented by a matrix.
- The **character** χ of such a matrix representation is the trace of the matrix, *i. e.*, the sum over all elements on the main diagonal.

[1] While the proper rotation consists only of a rotation, an improper rotation consists of a rotation followed by a reflection in a horizontal plane. The angle of rotation equals $m \cdot 2\pi/n$ with $m, n \in \mathbb{N}$.

[2] The indexes h, v and d denote reflections about a horizontal, vertical and dihedral mirror plane, respectively.

- A **symmetry class** or **conjugacy class** is the totality of all symmetry operations of a symmetry group which are conjugated to each other. Two symmetry operations A and B are called conjugate if $B = X^{-1}AX$ with X another symmetry operation in the same group.
- A **symmetry group** of an object such as a molecule is a collection of all symmetry operations under which the object is invariant.

For further details we refer the reader to relevant literature on group theory, such as the book of M. S. Dresselhaus, G. Dresselhaus and A. Jorio [283].

E.1 Metal-Free Phthalocyanine

The free H_2Pc molecule [Fig. E.1(a)] exhibits D_{2h} point group symmetry. The classification of the point group is based on the symmetry operations which are subject to H_2Pc: the identity, three two-fold proper rotations [Fig. E.2(a)], an inversion around the center of inversion [blue dot in Fig. E.2(a)], a horizontal [Fig. E.2(b)] and two vertical reflections [Fig. E.2(c)].

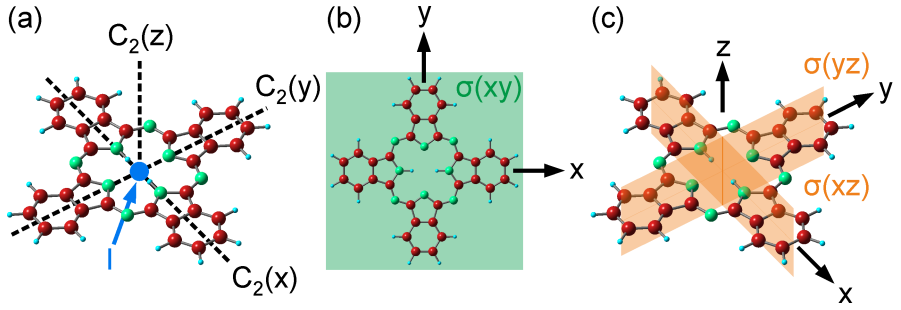

Fig. E.2: Symmetry operations of the D_{2h} point group. **(a)** Two-fold proper rotations, C_2, around fixed axes (dashed lines) whose orientations are given in parentheses. An inversion symmetry I is indicated by an inversion center (blue dot). **(b)** Horizontal reflection $\sigma(xy)$ about the green mirror plane. **(c)** Vertical reflections $\sigma(xz)$ and $\sigma(yz)$ about the orange mirror planes.

The symmetry classes, Q_j, of the D_{2h} point group together with the characters, $\chi^{red}(Q_j)$, of specific reducible representations of H_2Pc are summarized in Tab. E.1.

Tab. E.1: Reducible representation of H_2Pc. The top row denotes the symmetry classes, Q_j, of the D_{2h} point group, the bottom row lists the characters, $\chi^{red}(Q_j)$, of specific reducible representations of H_2Pc.

D_{2h}	E	$C_2(z)$	$C_2(y)$	$C_2(x)$	I	$\sigma(xy)$	$\sigma(xz)$	$\sigma(yz)$
$\chi^{red}(Q_j)$	168	2	0	−2	0	58	4	2

The number of times, a_i, a specific irreducible representation appears in the reducible representation may be calculated using the decomposition relation [283, p. 34],

$$a_i = \frac{1}{h} \sum_{j=1}^{h} N_j \cdot \left[\chi_i^{irr}(Q_j)\right]^* \cdot \chi^{red}(Q_j), \tag{E.1}$$

with h the number of symmetry classes in the group, N_j the number of symmetry operations in Q_j, $\chi^{red}(Q_j)$ the character of Q_j in the reducible representation and $\chi_i^{irr}(Q_j)$ the character of Q_j in the ith irreducible representation (Tab. E.2).

Tab. E.2: Character table of the D_{2h} point group. $A_g \ldots B_{3u}$ denote irreducible representations and $E \ldots \sigma(yz)$ symmetry classes Q_j of the group. The entries of the table are the characters $\chi_i^{irr}(Q_j)$ of Q_j in the ith irreducible representation.

D_{2h}	E	$C_2(z)$	$C_2(y)$	$C_2(x)$	I	$\sigma(xy)$	$\sigma(xz)$	$\sigma(yz)$
A_g	+1	+1	+1	+1	+1	+1	+1	+1
B_{1g}	+1	+1	−1	−1	+1	+1	−1	−1
B_{2g}	+1	−1	+1	−1	+1	−1	+1	−1
B_{3g}	+1	−1	−1	+1	+1	−1	−1	+1
A_u	+1	+1	+1	+1	−1	−1	−1	−1
B_{1u}	+1	+1	−1	−1	−1	−1	+1	+1
B_{2u}	+1	−1	+1	−1	−1	+1	−1	+1
B_{3u}	+1	−1	−1	+1	−1	+1	+1	−1

As a result, the symmetry of vibrational modes of free H_2Pc may be described by the irreducible representation summarized in Tab. E.3.

Tab. E.3: Irreducible representation of H_2Pc. The number of times, a_i, a specific irreducible representation appears in the reducible representation (Tab. E.1) is given.

D_{2h}	A_g	B_{1g}	B_{2g}	B_{3g}	A_u	B_{1u}	B_{2u}	B_{3u}
a_i	29	28	14	13	13	15	28	28

Upon adsorption of H_2Pc to Ir(111) the adsorbate complex exhibits C_s symmetry. The C_s character table is presented in Tab. E.4. To relate vibrational modes of the adsorbate complex to the modes of the gas-phase molecule, correlation tables may be used [129]. Table E.5 shows the correspondence of D_{2h} irreducible representations with those of C_s [129]. According to the selection rules for the dipole scattering regime, only those vibrational excitations from the ground state to the first excited state of an eigenmode will

Tab. E.4: Character table of the C_s point group [E: identity, $\sigma(xz)$: reflection at xz-plane]. A' and A'' denote irreducible representations of the C_s symmetry classes.

C_s	E	$\sigma(xz)$
A'	$+1$	$+1$
A''	$+1$	-1

be observed that belong to the totally symmetric representations A' [129]. Consequently, A_g, B_{2g} and B_{3u} vibrational modes will additionally become dipole active and visible in specular spectra upon symmetry reduction.

Tab. E.5: D_{2h} – C_s correlation table.

D_{2h}	A_g	A_u	B_{1g}	B_{1u}	B_{2g}	B_{2u}	B_{3g}	B_{3u}
C_s	A'	A''	A''	A'	A'	A''	A''	A'

The vibrational energies of modes belonging to the irreducible representations of free H_2Pc (Tab. E.2) were calculated within density functional theory [203] using Gaussian09 [204] with the hybrid functional B3LYP [205] and the Gaussian basis set $6-311G$ [206, 207]. The vibrational modes were calculated in the harmonic approximation with the molecule symmetry fixed to D_{2h}. The calculated energies together with the mode symmetry classes are listed in Tab. E.6. To compare calculations with experimental data the calculated energies were multiplied by 0.955, a factor that is similar to previous findings [284–286].

Tab. E.6: Calculated vibrational modes of free H_2Pc listed along with their symmetry. For infrared-active modes the direction of the oscillating dipole moment is indicated (∥: in-plane, ⊥: out-of-plane). The mode assignment identifies oscillating atoms (Fig. E.1) and refers to in-plane (out-of-plane) vibrations as stretching, scissoring, rocking, breathing (twisting, wagging).

No. & Symm.		Calc. energy $\begin{pmatrix}10^{-3}\\ \text{eV}\end{pmatrix}$	Infrared int. $\begin{pmatrix}10^{3}\\ \text{m/mol}\end{pmatrix}$	Raman int. $\begin{pmatrix}10^{27}\\ \text{A}^4/\text{kg}\end{pmatrix}$	Mode assignment
001	B_{1u}	2.632	0.003 (⊥)		twisting (all isoindole arms)
002	B_{1u}	5.035	1.938 (⊥)		wagging (whole molecule)
003	A_u	6.754			twisting (whole molecule)
004	B_{2g}	6.816		0.132	twisting (whole molecule)
005	B_{3g}	7.487		0.097	twisting (whole molecule)
006	B_{1g}	9.781		2.033	scissoring (whole molecule)
007	B_{2g}	14.881		5.388	twisting (all isoindole arms)
008	B_{2u}	15.158	3.504 (∥)		scissoring (2 opposite isoindole arms)
009	B_{3u}	15.285	4.461 (∥)		scissoring (2 opposite isoindole arms)
010	A_u	15.462			twisting (all isoindole arms)
011	B_{3g}	16.092		6.467	twisting (all isoindole arms)
012	A_g	16.389		18.845	asymm. stretching (whole molecule)
013	B_{1u}	17.506	0.414 (⊥)		twisting (all isoindole arms)
014	B_{1g}	22.017		17.094	asymm. stretching (whole molecule)
015	B_{1g}	26.197		0.939	rocking (whole molecule)
016	A_u	28.233			twisting (whole molecule)
017	B_{1u}	28.405	7.584 (⊥)		wagging (whole molecule)
018	A_g	28.419		42.435	symm. stretching (whole molecule)
019	B_{2g}	28.681		5.172	twisting (2 opposite isoindole arms)
020	B_{3g}	30.518		3.926	twisting (2 opposite isoindole arms)
021	B_{2u}	33.810	0.598 (∥)		scissoring (2 opposite isoindole arms) + asymm. stretching (other 2 isoindole arms)
022	B_{1u}	33.954	2.987 (⊥)		twisting (whole molecule)
023	B_{2g}	34.859		0.003	twisting (whole molecule)
024	B_{3u}	34.859	10.519 (∥)		scissoring (2 opposite isoindole arms) + asymm. stretching

No. & Symm.		Calc. energy $\left(\frac{10^{-3}}{\text{eV}}\right)$	Infrared int. $\left(\frac{10^{3}}{\text{m/mol}}\right)$	Raman int. $\left(\frac{10^{27}}{\text{A}^4/\text{kg}}\right)$	Mode assignment
025	B_{3g}	36.296		0.343	wagging (2 opposite isoindole arms + aza bridges)
026	B_{1u}	43.783	4.228 ($\perp$)		wagging (whole molecule)
027	A_u	53.911			twisting (all isoindole arms)
028	B_{2g}	55.032		0.010	twisting (C_2 + H_2 vs. $C_{1,3}$ + H_3 on opposite benzene rings)
029	B_{3g}	55.200		0.162	twisting (C_2 + H_2 vs. $C_{1,3}$ + H_3 on opposite benzene rings)
030	B_{1u}	55.366	0.005 ($\perp$)		twisting (C_2 + H_2 vs. $C_{1,3}$ + H_3 on all benzene rings)
031	B_{1u}	57.103	15.398 ($\perp$)		wagging (C_2 + H_2 vs. $C_{1,3}$ + H_3 on all benzene rings)
032	B_{1g}	60.951		71.853	scissoring (whole molecule)
033	B_{2u}	61.983	1.849 ($\parallel$)		scissoring (2 opposite isoindole arms + aza bridges)
034	B_{3u}	62.371	6.296 ($\parallel$)		scissoring (2 opposite isoindole arms + aza bridges)
035	B_{3g}	63.199		0.500	twisting (whole molecule)
036	B_{2g}	63.328		0.335	twisting (whole molecule)
037	A_u	66.462			twisting (whole molecule)
038	A_g	69.518		13.655	asymm. stretching (whole molecule)
039	B_{2u}	70.548	0.058 ($\parallel$)		asymm. stretching (whole molecule)
040	B_{3u}	71.382	3.896 ($\parallel$)		asymm. stretching (whole molecule)
041	A_g	72.517		40.179	breathing (whole molecule)
042	B_{1g}	73.105		0.749	rocking (whole molecule)
043	B_{1g}	76.495		0.046	rocking (whole molecule)
044	A_u	77.897			wagging (all isoindole arms)
045	B_{3u}	79.593	24.913 ($\parallel$)		scissoring (whole molecule)
046	B_{2u}	79.840	4.114 ($\parallel$)		scissoring (whole molecule
047	B_{3g}	80.019		0.556	twisting (whole molecule)
048	B_{2g}	80.523		0.574	twisting (whole molecule)

No. & Symm.		Calc. energy $\left(\begin{smallmatrix}10^{-3}\\ \text{eV}\end{smallmatrix}\right)$	Infrared int. $\left(\begin{smallmatrix}10^{3}\\ \text{m/mol}\end{smallmatrix}\right)$	Raman int. $\left(\begin{smallmatrix}10^{27}\\ \text{A}^4/\text{kg}\end{smallmatrix}\right)$	Mode assignment
049	A_g	84.802		239.222	symm. stretching (4 aza bridges + whole molecule)
050	A_u	85.907			twisting (whole molecule)
051	B_{1u}	87.639	0.016 ($\perp$)		wagging (whole molecule)
052	B_{1g}	88.198		5.482	scissoring (whole molecule)
053	B_{2g}	89.114		8.196	wagging (2 opposite C_N–$N_H$$H_N$–$C_N$ groups + H_2 + H_3)
054	B_{3g}	91.744		12.670	wagging (2 opposite C_N–N–C_N groups + H_2 + H_3)
055	B_{1u}	92.238	140.656 ($\perp$)		wagging [all C_N–N_H(H_N)–C_N groups + H_2 + H_3]
056	A_g	93.279		579.725	scissoring (porphyrazine)
057	B_{3u}	93.586	39.765 ($\parallel$)		rocking + scissoring (whole molecule)
058	B_{2u}	93.798	45.457 ($\parallel$)		scissoring + breathing (whole molecule)
059	A_u	96.288			twisting (all isoindole arms)
060	B_{2g}	96.547		1.117	twisting (2 opposite isoindole arms)
061	A_g	96.837		0.172	breathing (whole molecule)
062	B_{3g}	96.930		3.416	twisting (2 opposite isoindole arms)
063	A_u	96.941			twisting (all isoindole arms)
064	B_{2g}	98.532		0.036	twisting (H_N) + wagging (H_2 + H_3 at 2 opposite benzene rings)
065	B_{3u}	99.193	1.348 ($\parallel$)		rocking + scissoring (2 opposite isoindole arms)
066	B_{2u}	99.232	0.003 ($\parallel$)		rocking + scissoring (2 opposite isoindole arms)
067	B_{1u}	99.518	0.378 ($\perp$)		twisting (all H_2 + H_3)
068	B_{1u}	99.756	171.781 ($\perp$)		wagging (all H_2 + H_3 + H_N)
069	B_{3g}	99.810		4.396	twisting (H_2 + H_3 at 2 opposite benzene rings)
070	A_g	99.906		71.997	breathing (whole molecule)

No. & Symm.		Calc. energy $\left(\begin{smallmatrix}10^{-3}\\ \text{eV}\end{smallmatrix}\right)$	Infrared int. $\left(\begin{smallmatrix}10^{3}\\ \text{m/mol}\end{smallmatrix}\right)$	Raman int. $\left(\begin{smallmatrix}10^{27}\\ \text{A}^4/\text{kg}\end{smallmatrix}\right)$	Mode assignment
071	B_{2g}	102.381		2.889	twisting (2 opposite C_N–$N_H H_N$–C_N groups + H_2 + H_3)
072	B_{1g}	106.001		0.600	scissoring (whole molecule)
073	B_{2u}	106.274	1.906 (∥)		rocking + scissoring (2 opposite isoindole arms + porphyrazine)
074	B_{3u}	109.505	53.532 (∥)		rocking + scissoring (2 opposite isoindole arms + porphyrazine)
075	B_{1g}	111.410		0.144	rocking + scissoring (2 opposite isoindole arms + porphyrazine)
076	A_u	113.568			twisting (H_2 + H_3 at 2 opposite benzene rings)
077	B_{3g}	113.578		0.747	twisting (H_2 + H_3 at 2 opposite benzene rings)
078	A_u	113.807			twisting (H_2 + H_3 at 2 opposite benzene rings)
079	B_{2g}	113.821		1.099	twisting (H_2 + H_3 at 2 opposite benzene rings)
080	B_{1u}	114.960	156.957 (⊥)		wagging (H_N)
081	B_{3g}	123.744		0.393	twisting (H_2 + H_3 at 2 opposite benzene rings)
082	B_{1u}	123.744	2.781 (⊥)		twisting (H_2 + H_3 at 2 opposite benzene rings)
083	B_{2g}	124.520		0.009	twisting (H_2 + H_3 at 2 opposite benzene rings)
084	B_{1u}	124.524	2.719 (⊥)		twisting (H_2 + H_3 at 2 opposite benzene rings)
085	B_{3u}	126.960	305.914 (∥)		asymm. stretching (C_N–N–C_N) + symm. stretching (H_2 at 2 opposite benzene rings) + rocking (2 other benzene rings)
086	A_u	127.511			twisting (H_2 + H_3 at 2 opposite benzene rings)

No. & Symm.		Calc. energy $\left(\begin{smallmatrix}10^{-3}\\ \text{eV}\end{smallmatrix}\right)$	Infrared int. $\left(\begin{smallmatrix}10^{3}\\ \text{m/mol}\end{smallmatrix}\right)$	Raman int. $\left(\begin{smallmatrix}10^{27}\\ \text{A}^4\text{/kg}\end{smallmatrix}\right)$	Mode assignment
087	B_{2g}	127.512		0.011	twisting (H_2 + H_3 at 2 opposite benzene rings)
088	A_u	128.025			twisting (H_2 + H_3 at 2 opposite benzene rings)
089	B_{3g}	128.027		0.173	twisting (H_2 + H_3 at 2 opposite benzene rings)
090	A_g	128.052		151.543	symm. stretching (C_2–H_2 + C_3–H_3 at all benzene rings)
091	B_{2u}	128.066	12.066 (‖)		symm. stretching (C_2–H_2 + C_3–H_3 at 2 opposite benzene rings)
092	A_g	128.207		277.445	symm. stretching (C_2–H_2 + C_3–H_3 at all benzene rings)
093	B_{3u}	128.224	71.071 (‖)		symm. stretching (C_2–H_2 + C_3–H_3 at 2 opposite benzene rings)
094	B_{1g}	131.435		147.421	scissoring (whole molecule)
095	B_{2u}	133.998	16.762 (‖)		scissoring (2 opposite isoindole arms + H_2)
096	B_{3u}	134.924	25.904 (‖)		scissoring (2 opposite isoindole arms + H_2)
097	B_{1g}	138.050		0.362	asymm. stretching [opposite C_N–N_H(H_N)–C_N groups] + scissoring (whole molecule)
098	B_{2u}	138.225	195.341 (‖)		asymm. stretching [opposite C_N–N_H(H_N)–C_N groups] + scissoring (whole molecule)
099	B_{1g}	139.374		112.161	scissoring (opposite isoindole arms)
100	B_{1g}	140.969		222.390	scissoring (opposite isoindole arms)
101	A_g	141.154		668.426	symm. stretching (all N_H–H_N + N) + breathing (all isoindole arms)
102	B_{3u}	141.747	71.906 (‖)		scissoring (all H_2 + H_3)
103	B_{2u}	142.103	91.125 (‖)		scissoring (all H_2 + H_3 + N_H–H_N)

No. & Symm.		Calc. energy $\left(\begin{smallmatrix}10^{-3}\\ \text{eV}\end{smallmatrix}\right)$	Infrared int. $\left(\begin{smallmatrix}10^{3}\\ \text{m/mol}\end{smallmatrix}\right)$	Raman int. $\left(\begin{smallmatrix}10^{27}\\ \text{A}^4\text{/kg}\end{smallmatrix}\right)$	Mode assignment
104	A_g	145.872		1290.993	scissoring (all H_2 + H_3) + breathing (pyrrole rings)
105	B_{3u}	149.337	8.896 (‖)		scissoring (all H_2 + H_3)
106	B_{2u}	149.518	0.210 (‖)		symm. stretching (H_N) + scissoring (H_2 + H_3 at 2 opposite benzene rings)
107	A_g	149.887		58.136	scissoring (H_2 + H_3 at all benzene rings)
108	B_{1g}	150.234		325.062	scissoring (2 opposite isoindole arms) + asymm. stretching (H_N)
109	A_g	150.697		69.229	scissoring (2 opposite isoindole arms) + symm. stretching (H_N)
110	B_{3u}	151.125	0.670 (‖)		scissoring (H_3 at 2 opposite benzene rings)
111	B_{2u}	151.691	36.690 (‖)		scissoring (H_2 + H_3 at 2 opposite benzene rings)
112	B_{1g}	152.730		38.417	scissoring (H_2 + H_3 at 2 opposite benzene rings) + asymm. stretching (N_H–H_N)
113	B_{1g}	157.667		52.337	scissoring (N_H–H_N) + rocking (all H_2)
114	B_{2u}	161.655	117.766 (‖)		scissoring (2 opposite isoindole arms) + asymm. stretching (N_H–H_N)
115	A_g	162.253		3192.172	symm. stretching (N vs. N)
116	B_{2u}	163.294	7.469 (‖)		asymm. stretching (N_H–H_N) + rocking (H_2)
117	B_{3u}	164.436	6.547 (‖)		rocking (H_2 at 2 opposite benzene rings) + scissoring (whole molecule)
118	B_{3u}	165.895	40.839 (‖)		rocking (H_2 + H_3 at 2 opposite benzene rings)
119	B_{1g}	166.148		73.221	rocking (H_2 + H_3 at 2 opposite benzene rings)

No. & Symm.		Calc. energy $\left(\begin{smallmatrix}10^{-3}\\ \text{eV}\end{smallmatrix}\right)$	Infrared int. $\left(\begin{smallmatrix}10^{3}\\ \text{m/mol}\end{smallmatrix}\right)$	Raman int. $\left(\begin{smallmatrix}10^{27}\\ \text{A}^4/\text{kg}\end{smallmatrix}\right)$	Mode assignment
120	B_{2u}	167.744	34.559 (‖)		rocking (H_2 + H_3 at 2 opposite benzene rings + N_H)
121	A_g	168.178		1610.367	breathing (whole molecule)
122	B_{1g}	168.219		138.531	rocking (H_2 + H_3 at 2 opposite benzene rings + N_H)
123	B_{3u}	169.498	230.495 (‖)		scissoring (2 opposite benzene rings) + rocking (H_2 + H_3 at other benzene rings)
124	B_{2u}	171.255	178.312 (‖)		scissoring (2 opposite benzene rings) + rocking (H_2 + H_3 at other benzene rings)
125	A_g	171.997		1348.300	rocking + scissoring (benzene rings)
126	A_g	174.691		4.866	rocking + scissoring (whole molecule)
127	B_{3u}	178.805	28.012 (‖)		scissoring (2 opposite isoindole arms)
128	A_g	182.273		253.666	scissoring (H_2 + H_3)
129	B_{1g}	182.498		271.263	symm. stretching (C_N–N_C + N_H–H_N)
130	B_{2u}	183.712	104.163 (‖)		scissoring (H_2 + H_3 at 2 opposite benzene rings + H_N)
131	A_g	184.664		986.177	scissoring (all benzene rings)
132	B_{3u}	185.996	58.828 (‖)		scissoring (2 opposite isoindole arms)
133	B_{1g}	187.907		31.053	rocking (C_3–H_3 at 2 opposite rings)
134	B_{3u}	187.959	4.167 (‖)		rocking (C_3–H_3 at 2 opposite benzene rings)
135	B_{2u}	188.870	19.224 (‖)		rocking (C_3–H_3 at 2 opposite benzene rings)
136	B_{1g}	189.028		57.363	rocking (C_3–H_3 at 2 opposite benzene rings)
137	B_{3u}	189.572	77.273 (‖)		symm. stretching (porphyrazine)
138	B_{2u}	190.548	31.267 (‖)		symm. stretching (porphyrazine)
139	A_g	192.239		885.774	symm. stretching (porphyrazine)

No. & Symm.		Calc. energy $\left(\begin{smallmatrix}10^{-3}\\ \text{eV}\end{smallmatrix}\right)$	Infrared int. $\left(\begin{smallmatrix}10^{3}\\ \text{m/mol}\end{smallmatrix}\right)$	Raman int. $\left(\begin{smallmatrix}10^{27}\\ \text{A}^4\text{/kg}\end{smallmatrix}\right)$	Mode assignment
140	B_{1g}	194.886		30.422	symm. stretching (porphyrazine)
141	B_{2u}	195.774	4.737 (‖)		symm. stretching (porphyrazine)
142	A_g	198.168		10927.901	symm. stretching (porphyrazine)
143	B_{3u}	200.294	0.044 (‖)		symm. stretching (C_1 vs. C_1' + C_3 vs. C_3' at 2 opposite benzene rings)
144	A_g	200.473		443.343	symm. stretching (C_1 vs. C_1' + C_3 vs. C_3' at 2 opposite benzene rings)
145	B_{2u}	202.040	2.728 (‖)		symm. stretching (C_1 vs. C_1' + C_3 vs. C_3' at 2 opposite benzene rings)
146	A_g	202.060		36.441	symm. stretching (C_1 vs. C_1' + C_3 vs. C_3' at 2 opposite benzene rings)
147	B_{1g}	204.415		0.026	stretching (2 opposite bezene rings)
148	B_{3u}	204.454	9.404 (‖)		stretching (2 opposite bezene rings)
149	B_{1g}	205.481		46.882	stretching (2 opposite bezene rings)
150	B_{2u}	205.491	14.209 (‖)		stretching (2 opposite bezene rings)
151	B_{3u}	392.791	8.066 (‖)		stretching (C–H at 2 opposite benzene rings)
152	B_{1g}	392.791		121.875	stretching (C–H at 2 opposite benzene rings)
153	B_{2u}	393.293	9.875 (‖)		stretching (C–H at 2 opposite benzene rings)
154	B_{1g}	393.293		134.733	stretching (C–H at 2 opposite benzene rings)
155	B_{2u}	394.771	63.935 (‖)		stretching (C–H at 2 opposite benzene rings)
156	A_g	394.775		376.690	stretching (C–H at 2 opposite benzene rings)

No. & Symm.		Calc. energy $\left(\begin{smallmatrix}10^{-3}\\ \text{eV}\end{smallmatrix}\right)$	Infrared int. $\left(\begin{smallmatrix}10^{3}\\ \text{m/mol}\end{smallmatrix}\right)$	Raman int. $\left(\begin{smallmatrix}10^{27}\\ \text{A}^4/\text{kg}\end{smallmatrix}\right)$	Mode assignment
157	B_{3u}	395.237	56.243 (‖)		stretching (C–H at 2 opposite benzene rings)
158	A_g	395.241		383.928	stretching (C–H at 2 opposite benzene rings)
159	B_{1g}	396.711		108.837	stretching (C–H at 2 opposite benzene rings)
160	B_{3u}	396.712	25.801 (‖)		stretching (C–H at 2 opposite benzene rings)
161	B_{2u}	397.278	11.317 (‖)		stretching (C–H at 2 opposite benzene rings)
162	B_{1g}	397.278		108.726	stretching (C–H at 2 opposite benzene rings)
163	B_{2u}	397.366	106.352 (‖)		stretching (C–H at 2 opposite benzene rings)
164	A_g	397.382		458.288	symm. stretching (C–H at 2 opposite benzene rings)
165	B_{3u}	397.862	83.916 (‖)		stretching (C–H at 2 opposite benzene rings)
166	A_g	397.876		531.017	symm. stretching (C–H at 2 opposite benzene rings)
167	B_{3u}	439.085	123.995 (‖)		asymm. stretching (N_H–H_N)
168	A_g	445.916		12.611	symm. stretching (N_H–H_N)

E.2 Manganese Phthalocyanine

The free MnPc molecule [Fig. E.1(b)] exhibits D_{4h} point group symmetry. The classification of the point group is based on the symmetry operations which are subject to MnPc:

- the identity E
- two conjugated, four-fold proper rotations $2C_4(z) = \left\{C_4^1(z), C_4^3(z)\right\}$ and a two-fold proper rotation $C_2(z) = C_4^2(z)$, all around the z-axis [Fig. E.3(a)]
- two conjugated, two-fold proper rotations $2C_2'$ around the C_2' axes and two further conjugated, two-fold proper rotations $2C_2''$ around the C_2'' axes [Fig. E.3(a)]
- two conjugated, two-fold improper rotations $2S_4 = \left\{S_4^1, S_4^3\right\}$ and an inversion $I = S_4^2$ around the Mn atom
- a horizontal reflection σ_h around the xy-plane [like in Fig. E.2(b)], two conjugated reflections around the vertical mirror planes σ_v [Fig. E.3(b)] and two around the dihedral mirror planes σ_d [Fig. E.3(c)].

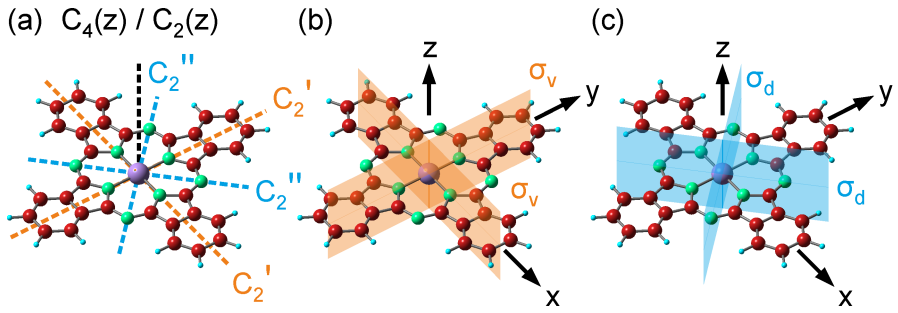

Fig. E.3: Symmetry operations of the D_{4h} point group. **(a)** N-fold proper rotations C_n around the indicated axes (dashed colored lines). **(b)** Reflections σ_v across vertical mirror planes (orange). **(c)** Reflections σ_d across dihedral mirror planes (blue).

The symmetry classes, Q_j, of the D_{4h} point group together with the characters, $\chi^{red}(Q_j)$, of specific reducible representations of MnPc are summarized in Tab. E.7.

Tab. E.7: Reducible representation of MnPc.

D_{4h}	E	$2C_4(z)$	C_2	$2C_2'$	$2C_2''$	I	$2S_4$	σ_h	$2\sigma_v$	$2\sigma_d$
$\chi^{red}(Q_j)$	165	−1	1	−1	−1	−3	−1	57	3	3

Tab. E.8: Character table of the D_{4h} point group. $A_{1g} \dots E_u$ denote irreducible representations and $E \dots \sigma_d$ symmetry classes Q_j of the group. The entries of the table are the characters $\chi_i^{irr}(Q_j)$ of Q_j in the ith irreducible representation.

D_{4h}	E	$2C_4(z)$	C_2	$2C_2'$	$2C_2''$	I	$2S_4$	σ_h	$2\sigma_v$	$2\sigma_d$
A_{1g}	+1	+1	+1	+1	+1	+1	+1	+1	+1	+1
A_{2g}	+1	+1	+1	−1	−1	+1	+1	+1	−1	−1
B_{1g}	+1	−1	+1	+1	−1	+1	−1	+1	+1	−1
B_{2g}	+1	−1	+1	−1	+1	+1	−1	+1	−1	+1
E_g	+2	0	−2	0	0	+2	0	−2	0	0
A_{1u}	+1	+1	+1	+1	+1	−1	−1	−1	−1	−1
A_{2u}	+1	+1	+1	−1	−1	−1	−1	−1	+1	+1
B_{1u}	+1	−1	+1	+1	−1	−1	+1	−1	−1	+1
B_{2u}	+1	−1	+1	−1	+1	−1	+1	−1	+1	−1
E_u	+2	0	−2	0	0	−2	0	+2	0	0

Using Eq. (E.1) and the character table of the D_{4h} point group (Tab. E.8), the number of times, a_i, specific irreducible representations appear in the reducible representations of MnPc may be calculated. As a result, the symmetry of vibrational modes of free MnPc may be described by the irreducible representation summarized in Tab. E.9.

Tab. E.9: Irreducible representation of MnPc. The number of times, a_i, a specific irreducible representation appears in the reducible representation (Tab. E.7) is given.

D_{4h}	A_{1g}	A_{2g}	B_{1g}	B_{2g}	E_g	A_{1u}	A_{2u}	B_{1u}	B_{2u}	E_u
a_i	14	13	14	14	13	6	8	7	7	28

The vibrational energies of modes belonging to the irreducible representations of free MnPc (Tab. E.8) were calculated within density functional theory [203] using Gaussian09 [204] with the hybrid functional B3LYP [205] and the Gaussian basis set $6-311G(2d,2p)$ [206, 207, 229–231].[3] The vibrational modes were calculated in the harmonic approximation with the molecule symmetry fixed to D_{4h}. The calculated energies together with the mode symmetry classes are listed in Tab. E.10. To compare calculations with experimental data the calculated energies were multiplied by 0.962, a factor that is similar to previous findings [284–286].

[3] MnPc represents a spin doublet. Therefore, unrestricted open-shell calculations were performed. The results are suitable for a comparison with experimental data since the spin contamination ($\langle S^2 \rangle = 0.7502$) is quite low after the Gaussian09 internal annihilation of the first spin contaminant.

Tab. E.10: Calculated vibrational modes of free MnPc listed along with their symmetry. For infrared-active modes the direction of the oscillating dipole moment is indicated (∥: in-plane, ⊥: out-of-plane). The mode assignment identifies oscillating atoms (Fig. E.1) and refers to in-plane (out-of-plane) vibrations as stretching, scissoring, rocking, breathing (twisting, wagging).

No. & Symm.		Calc. energy $\left(\frac{10^{-3}}{\text{eV}}\right)$	Infrared int. $\left(\frac{10^{3}}{\text{m/mol}}\right)$	Raman int. $\left(\frac{10^{27}}{\text{A}^4/\text{kg}}\right)$	Mode assignment
001	B_{2u}	2.337			wagging (at opposite isoindole arms)
002	A_{2u}	4.702	0.485 (⊥)		wagging (whole molecule)
003	B_{1u}	6.044			twisting (whole molecule)
004	E_g	8.233		0.075	twisting (2 opposite isoindole arms) + wagging (2 other isoindole arms)
005	E_g	8.233		0.075	twisting (2 opposite isoindole arms) + wagging (2 other isoindole arms)
006	B_{2g}	14.109		6.872	scissoring (whole molecule)
007	A_{1u}	14.758			twisting (at opposite isoindole arms)
008	E_u	15.189	2.900 (∥)		scissoring (2 opposite isoindole arms)
009	E_u	15.189	2.900 (∥)		scissoring (2 opposite isoindole arms)
010	E_g	15.210		5.631	twisting (2 opposite isoindole arms) + wagging (2 other isoindole arms)
011	E_g	15.210		5.631	twisting (2 opposite isoindole arms) + wagging (2 other isoindole arms)
012	B_{2u}	17.647			wagging (at opposite isoindole arms)
013	A_{2u}	20.995	10.967 (⊥)		wagging (whole molecule)
014	B_{1g}	24.790		4.866	asymm. stretching (at opposite isoindole arms)
015	A_{2g}	26.729			rocking (whole molecule)
016	B_{1u}	27.395			twisting (whole molecule)
017	B_{2g}	28.857		19.958	asymm. stretching (porphyrazine ring)
018	E_g	31.976		1.698	twisting (whole molecule)
019	E_g	31.976		1.698	twisting (whole molecule)
020	A_{1g}	32.496		48.725	asymm. stretching (whole molecule)
021	E_g	35.260		1.135	twisting (whole molecule, especially 2 opposite N_H atoms)

No. & Symm.		Calc. energy $\left(\begin{smallmatrix}10^{-3}\\ \text{eV}\end{smallmatrix}\right)$	Infrared int. $\left(\begin{smallmatrix}10^{3}\\ \text{m/mol}\end{smallmatrix}\right)$	Raman int. $\left(\begin{smallmatrix}10^{27}\\ \text{A}^4\text{/kg}\end{smallmatrix}\right)$	Mode assignment
022	E_g	35.260		1.135	twisting (whole molecule, especially 2 opposite N_H atoms)
023	E_u	36.963	3.848 (∥)		scissoring (2 opposite isoindole arms) + symm. stretching (2 other isoindole arms)
024	E_u	36.963	3.848 (∥)		scissoring (2 opposite isoindole arms) + symm. stretching (2 other isoindole arms)
025	A_{2u}	39.091	2.788 (⊥)		wagging (whole molecule)
026	B_{2u}	39.631			wagging (whole molecule. especially at opposite N_H atoms)
027	E_u	43.442	0.301 (∥)		diagonal stretching (Mn atom) + rocking (whole molecule)
028	E_u	43.442	0.301 (∥)		diagonal stretching (Mn atom) + rocking (whole molecule)
029	A_{2u}	46.183	0.007 (⊥)		wagging (Mn atom + porphyrazine ring)
030	A_{1u}	52.537			twisting (all isoindole arms)
031	E_g	53.857		0.026	wagging (H_2 atoms at 2 opposite benzole rings)
032	E_g	53.857		0.026	wagging (H_2 atoms at 2 opposite benzole rings)
033	B_{2u}	54.259			wagging (H_2 atoms at all benzole rings)
034	A_{2u}	55.387	9.844 (⊥)		wagging (H_2 atoms at all benzole rings)
035	B_{2g}	61.063		47.692	rocking (whole molecule)
036	E_g	62.880		0.407	twisting (whole molecule)
037	E_g	62.880		0.407	twisting (whole molecule)
038	E_u	64.411	3.787 (∥)		scissoring (2 opposite isoindole arms + porphyrazine ring)

No. & Symm.		Calc. energy $\left(\begin{smallmatrix}10^{-3}\\ \text{eV}\end{smallmatrix}\right)$	Infrared int. $\left(\begin{smallmatrix}10^{3}\\ \text{m/mol}\end{smallmatrix}\right)$	Raman int. $\left(\begin{smallmatrix}10^{27}\\ \text{A}^4\text{/kg}\end{smallmatrix}\right)$	Mode assignment
039	E_u	64.411	3.787 ($\parallel$)		scissoring (2 opposite isoindole arms + porphyrazine ring)
040	B_{1u}	66.290			twisting (all isoindole arms + aza bridges)
041	B_{1g}	71.378		0.936	asymm. stretching (whole molecule)
042	E_u	72.758	10.683 ($\parallel$)		stretching (whole molecule)
043	E_u	72.758	10.683 ($\parallel$)		stretching (whole molecule)
044	A_{2g}	73.298			stretching (whole molecule)
045	A_{1g}	74.963		62.395	breathing (whole molecule)
046	A_{1u}	76.716			twisting (all isoindole arms)
047	A_{2g}	78.863			rocking (porphyrazine ring + pyrrole rings)
048	E_g	78.963		0.777	twisting (whole molecule)
049	E_g	78.963		0.777	twisting (whole molecule)
050	E_u	81.837	3.719 ($\parallel$)		stretching (whole molecule)
051	E_u	81.837	3.719 ($\parallel$)		stretching (whole molecule)
052	B_{2u}	85.913			wagging (whole molecule)
053	A_{1g}	86.078		135.914	symm. stretching (whole molecule)
054	B_{1u}	86.286			twisting (all isoindole arms + aza bridges)
055	B_{2g}	87.291		4.469	asymm. stretching (all isoindole arms + aza bridges)
056	E_g	91.203		6.287	twisting (2 opposite isoindole arms)
057	E_g	91.203		6.287	twisting (2 opposite isoindole arms)
058	A_{2u}	93.380	220.792 ($\perp$)		wagging (whole molecule)
059	B_{1g}	95.022		349.137	scissoring (whole molecule, especially the porphyrazine ring)
060	E_u	95.547	53.657 ($\parallel$)		asymm. stretching (whole molecule, especially the porphyrazine ring)
061	E_u	95.547	53.657 ($\parallel$)		asymm. stretching (whole molecule, especially the porphyrazine ring)

No. & Symm.		Calc. energy $\left(\begin{smallmatrix}10^{-3}\\ \text{eV}\end{smallmatrix}\right)$	Infrared int. $\left(\begin{smallmatrix}10^{3}\\ \text{m/mol}\end{smallmatrix}\right)$	Raman int. $\left(\begin{smallmatrix}10^{27}\\ \text{A}^4\text{/kg}\end{smallmatrix}\right)$	Mode assignment
062	B_{2u}	96.700			wagging (H atoms at opposite benzene rings)
063	E_g	97.027		0.412	twisting (H atoms at 2 opposite benzene rings)
064	E_g	97.027		0.412	twisting (H atoms at 2 opposite benzene rings)
065	A_{1u}	98.334			wagging (whole molecule)
066	A_{2u}	98.741	20.364 ($\perp$)		twisting (whole molecule)
067	E_g	99.229		3.023	twisting (whole molecule)
068	E_g	99.229		3.023	twisting (whole molecule)
069	B_{1u}	99.315			twisting (all C and H_2 atoms + aza bridges)
070	B_{1g}	99.639		118.326	asymm. stretching (whole molecule)
071	E_u	101.823	0.370 ($\parallel$)		asymm. stretching (whole molecule)
072	E_u	101.823	0.370 ($\parallel$)		asymm. stretching (whole molecule)
073	A_{1g}	106.585		68.584	symm. stretching (whole molecule)
074	A_{2g}	108.095			asymm. stretching (whole molecule)
075	A_{1u}	110.924			twisting (all H atoms)
076	E_g	111.061		0.553	twisting (all H atoms at 2 opposite benzene rings)
077	E_g	111.061		0.553	twisting (all H atoms at 2 opposite benzene rings)
078	B_{1u}	111.138			twisting (all H atoms)
079	E_u	114.863	22.837 ($\parallel$)		asymm. stretching (porphyrazine ring + 2 opposite isoindole arms)
080	E_u	114.863	22.837 ($\parallel$)		asymm. stretching (porphyrazine ring + 2 opposite isoindole arms)
081	B_{2g}	120.189		10.317	asymm. stretching (whole molecule)
082	B_{2u}	120.675			wagging (pairs of H_2 + H_3 atoms at all benzene rings)
083	E_g	120.738		0.011	wagging (pairs of H_2 + H_3 atoms at 2 opposite benzene rings)

No. & Symm.		Calc. energy $\left(\begin{smallmatrix}10^{-3}\\ \text{eV}\end{smallmatrix}\right)$	Infrared int. $\left(\begin{smallmatrix}10^{3}\\ \text{m/mol}\end{smallmatrix}\right)$	Raman int. $\left(\begin{smallmatrix}10^{27}\\ \text{A}^4/\text{kg}\end{smallmatrix}\right)$	Mode assignment
084	E_g	120.738		0.011	wagging (pairs of H_2 + H_3 atoms at 2 opposite benzene rings)
085	A_{2u}	120.810	2.835 ($\perp$)		wagging (pairs of H_2 + H_3 atoms at all benzene rings)
086	A_{1u}	124.447			twisting (pairs of H_2 + H_3 atoms at all benzene rings)
087	E_g	124.477		0.009	twisting (pairs of H_2 + H_3 atoms at 2 opposite benzene rings)
088	E_g	124.477		0.009	twisting (pairs of H_2 + H_3 atoms at 2 opposite benzene rings)
089	B_{1u}	124.505			twisting (pairs of H_2 + H_3 atoms at all benzene rings)
090	B_{1g}	127.695		92.306	asymm. stretching (pairs of H_2 + H_3 atoms at all benzene rings)
091	E_u	127.760	10.139 ($\parallel$)		asymm. stretching (pairs of H_2 + H_3 atoms at 2 opposite benzene rings)
092	E_u	127.760	10.139 ($\parallel$)		asymm. stretching (pairs of H_2 + H_3 atoms at 2 opposite benzene rings)
093	A_{1g}	127.838		248.933	asymm. stretching (pairs of H_2 + H_3 atoms at all benzene rings)
094	B_{2g}	131.498		51.758	symm. stretching (whole molecule)
095	E_u	135.522	2.798 ($\parallel$)		stretching (porphyrazine ring + 2 opposite isoindole arms)
096	E_u	135.522	2.798 ($\parallel$)		stretching (porphyrazine ring + 2 opposite isoindole arms)
097	E_u	136.249	290.489 ($\parallel$)		asymm. stretching (pairs of C_1 + H_2 + H_3 atoms + 2 opposite N_H–C_N pairs)
098	E_u	136.249	290.489 ($\parallel$)		asymm. stretching (pairs of C_1 + H_2 + H_3 atoms + 2 opposite N_H–C_N pairs)
099	A_{2g}	138.633			scissoring (all H atoms)

No. & Symm.		Calc. energy (10^{-3} eV)	Infrared int. (10^3 m/mol)	Raman int. (10^{27} A^4/kg)	Mode assignment
100	B_{2g}	140.093		133.955	scissoring (all H atoms)
101	A_{2g}	140.513			rocking (porphyrazine ring)
102	E_u	141.610	168.612 (‖)		scissoring (all H atoms)
103	E_u	141.610	168.612 (‖)		scissoring (all H atoms)
104	A_{1g}	142.926		499.581	scissoring (all H atoms) + stretching (all pyrrole groups)
105	B_{1g}	143.812		959.974	scissoring (all H atoms) + stretching (all pyrrole groups)
106	A_{1g}	147.158		274.371	scissoring (primarily all H_3 atoms)
107	E_u	147.314	44.208 (‖)		scissoring (primarily H_3 atoms at 2 opposite benzene rings)
108	E_u	147.314	44.208 (‖)		scissoring (primarily H_3 atoms at 2 opposite benzene rings)
109	B_{1g}	149.346		522.938	scissoring (primarily all H_3 atoms)
110	A_{2g}	150.432			rocking (pairs of H_2 atoms) + scissoring (whole molecule)
111	E_u	150.659	1.201 (‖)		rocking (2 pairs of H_2 atoms) + stretching (whole molecule)
112	E_u	150.659	1.201 (‖)		rocking (2 pairs of H_2 atoms) + stretching (whole molecule)
113	B_{2g}	152.066		194.624	rocking (pairs of H_2 atoms) + scissoring (whole molecule)
114	E_u	164.007	46.107 (‖)		rocking (H atoms at 2 opposite benzene rings)
115	E_u	164.007	46.107 (‖)		rocking (H atoms at 2 opposite benzene rings)
116	A_{2g}	164.363			rocking (all H atoms)
117	B_{1g}	164.968		1842.814	stretching (whole molecule)
118	B_{2g}	165.361		117.111	rocking (all H atoms)
119	E_u	167.303	65.199 (‖)		stretching (2 opposite pyrrole rings)
120	E_u	167.303	65.199 (‖)		stretching (2 opposite pyrrole rings)

No. & Symm.		Calc. energy $\left(\begin{smallmatrix}10^{-3}\\ \text{eV}\end{smallmatrix}\right)$	Infrared int. $\left(\begin{smallmatrix}10^{3}\\ \text{m/mol}\end{smallmatrix}\right)$	Raman int. $\left(\begin{smallmatrix}10^{27}\\ \text{A}^4/\text{kg}\end{smallmatrix}\right)$	Mode assignment
121	A_{1g}	168.148		1179.829	stretching + breathing (whole molecule)
122	E_u	168.870	99.959 (‖)		stretching (2 opposite benzene rings) + rocking (H atoms at 2 other benzene rings)
123	E_u	168.870	99.959 (‖)		stretching (2 opposite benzene rings) + rocking (H atoms at 2 other benzene rings)
124	B_{1g}	170.220		1674.975	scissoring (all C_3 + H_3 atoms)
125	A_{1g}	174.282		55.355	scissoring (all C_3 + H_3 atoms) + stretching (whole molecule)
126	E_u	180.002	99.829 (‖)		scissoring (H atoms at 2 opposite benzene rings) + stretching (all C_N vs. N_C)
127	E_u	180.002	99.829 (‖)		scissoring (H atoms at 2 opposite benzene rings) + stretching (all C_N vs. N_C)
128	A_{1g}	181.810		156.382	scissoring (all H atoms) + breathing (all pyrrole rings)
129	B_{2g}	182.793		117.015	stretching (porphyrazine ring) + rocking (all H atoms)
130	B_{1g}	183.832		1433.867	scissoring (all H atoms) + asymm. stretching (C_1 vs. C_1')
131	E_u	186.585	25.623 (‖)		scissoring (H atoms at 2 opposite benzene rings) + rocking (H atoms at 2 other benzene rings)
132	E_u	186.585	25.623 (‖)		scissoring (H atoms at 2 opposite benzene rings) + rocking (H atoms at 2 other benzene rings)
133	A_{2g}	187.213			rocking (all H atoms)
134	B_{2g}	187.705		53.537	scissoring (all H atoms) + asymm. stretching (all benzene ring C atoms)

No. & Symm.		Calc. energy $\begin{pmatrix} 10^{-3} \\ \text{eV} \end{pmatrix}$	Infrared int. $\begin{pmatrix} 10^{3} \\ \text{m/mol} \end{pmatrix}$	Raman int. $\begin{pmatrix} 10^{27} \\ \text{A}^4/\text{kg} \end{pmatrix}$	Mode assignment
135	E_u	187.891	0.081 (‖)		scissoring + stretching (all isoindole arms + aza bridges)
136	E_u	187.891	0.081 (‖)		scissoring + stretching (all isoindole arms + aza bridges)
137	A_{2g}	188.204			stretching (porphyrazine ring) + rocking(all H atoms)
138	E_u	190.551	104.075 (‖)		asymm. stretching (C_N vs. N_C atoms)
139	E_u	190.551	104.075 (‖)		asymm. stretching (C_N vs. N_C atoms)
140	A_{1g}	192.548		639.541	asymm. stretching (C_N vs. N_C atoms + C_1 atoms)
141	B_{1g}	193.961		7687.244	asymm. stretching (C_N vs. N_C atoms)
142	B_{1g}	201.284		0.047	asymm. stretching (C_1 vs. C_1' + C_3 vs. C_3') + scissoring (all H atoms)
143	E_u	201.286	9.674 (‖)		asymm. stretching (C_1 vs. C_1' + C_3 vs. C_3' at 2 opposite benzene rings) + scissoring (H atoms at 2 opposite benzene rings)
144	E_u	201.286	9.674 (‖)		asymm. stretching (C_1 vs. C_1' + C_3 vs. C_3' at 2 opposite benzene rings) + scissoring (H atoms at 2 opposite benzene rings)
145	A_{1g}	201.460		92.694	asymm. stretching (C_1 vs. C_1' + C_3 vs. C_3') + scissoring (all H atoms)
146	A_{2g}	203.784			asymm. stretching (C_1 vs. C_2 + C_1' vs. C_2' at all benzene rings)
147	E_u	203.953	10.717 (‖)		asymm. stretching (C_1 vs. C_2 + C_1' vs. C_2' at 2 opposite benzene rings)

No. & Symm.		Calc. energy $\left(\frac{10^{-3}}{\text{eV}}\right)$	Infrared int. $\left(\frac{10^{3}}{\text{m/mol}}\right)$	Raman int. $\left(\frac{10^{27}}{\text{A}^4/\text{kg}}\right)$	Mode assignment
148	E_u	203.953	10.717 (‖)		asymm. stretching (C_1 vs. C_2 + C_1' vs. C_2' at 2 opposite benzene rings)
149	B_{2g}	204.167		1.953	asymm. stretching (C_1 vs. C_2 + C_1' vs. C_2' at all benzene rings)
150	A_{2g}	392.951			asymm. stretching (C–H at all benzene rings)
151	E_u	392.955	6.488 (‖)		asymm. stretching (C–H at 2 opposite benzene rings)
152	E_u	392.955	6.488 (‖)		asymm. stretching (C–H at 2 opposite benzene rings)
153	B_{2g}	392.956		251.141	asymm. stretching (C–H at all benzene rings)
154	B_{1g}	394.725		484.628	asymm. stretching (C–H at all benzene rings)
155	E_u	394.731	44.654 (‖)		asymm. stretching (C–H at 2 opposite benzene rings)
156	E_u	394.731	44.654 (‖)		asymm. stretching (C–H at 2 opposite benzene rings)
157	A_{1g}	394.743		481.831	asymm. stretching (C–H at all benzene rings)
158	A_{2g}	396.607			symm. + asymm. stretching (C–H at all benzene rings)
159	E_u	396.626	13.023 (‖)		symm. + asymm. stretching (C–H at 2 opposite benzene rings)
160	E_u	396.626	13.023 (‖)		symm. + asymm. stretching (C–H at 2 opposite benzene rings)
161	B_{2g}	396.646		223.824	symm. + asymm. stretching (C–H at all benzene rings)
162	B_{1g}	397.013		52.735	symm. stretching (C–H at all benzene rings)
163	E_u	397.028	57.713 (‖)		symm. stretching (C–H at 2 opposite benzene rings)

No. & Symm.	**Calc. energy** $\begin{pmatrix} 10^{-3} \\ \text{eV} \end{pmatrix}$	**Infrared int.** $\begin{pmatrix} 10^{3} \\ \text{m/mol} \end{pmatrix}$	**Raman int.** $\begin{pmatrix} 10^{27} \\ \text{A}^4/\text{kg} \end{pmatrix}$	**Mode assignment**
164 E_u	397.028	57.713 (‖)		symm. stretching (C–H at 2 opposite benzene rings)
165 A_{1g}	397.062		873.010	symm. stretching (C–H at all benzene rings)

F Properties of CO and Phthalocyanines on Ir(111)

Supplementary to Chapter 4, this appendix provides further insight into the density functional theory calculations which were performed to determine electronic and vibrational properties of CO and C_6H_6 on Ir(111). Different arrangements of CO and C_6H_6 on a five-layer Ir(111) slab were used to this end (Fig. F.1). Rather than identifying the energetically most favorable superstructures by calculating all conceivable adsorbate configurations, we have investigated selected configurations in order to understand the main trends.

F.1 Calculated Adsorption Structures

CO had been demonstrated to preferably adsorb at on-top sites of Ir(111) [256, 258]. According to our vibrational spectra a change of this adsorption site upon coadsorption of H_2Pc can be excluded. Therefore, we adopted the on-top adsorption site in superstructures with coadsorbed C_6H_6. Each supercell contained a single CO molecule, which corresponds to CO coverages of 0.04 ML [Ir(5×5) supercell] and 0.06 ML [Ir(4×4) supercell]. These CO coverages are close to the experimental CO coverage of ≈ 0.05 ML.

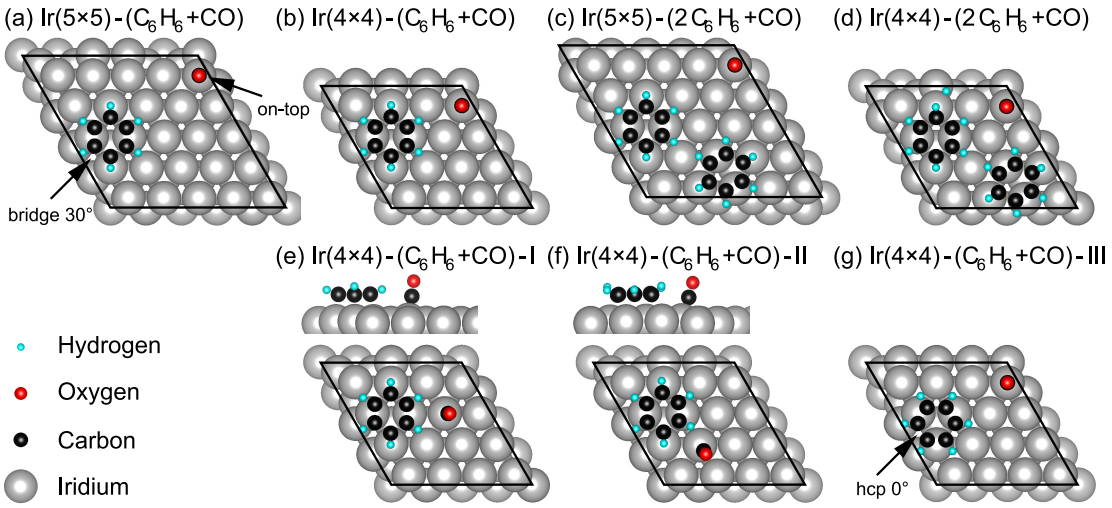

Fig. F.1: Relaxed geometries of calculated superstructures. **(a)**–**(d)** Adsorption of C_6H_6 and CO on a five-layer slab of Ir(111) with different supercell sizes. The supercell boundary is indicated by the black line. Different C_6H_6 coverages were simulated by placing different numbers of molecules in the Ir(5×5) and Ir(4×4) supercells. All supercells contain a single CO molecule corresponding to CO coverages of 0.04 ML in Ir(5×5) cells and 0.06 ML in Ir(4×4) cells. C_6H_6 (CO) is adsorbed at bridge-30° (on-top) Ir(111) sites. **(e)**, **(f)** Distortion of CO adsorption geometry at low C_6H_6–CO distances. **(g)** Same as (b) for adsorption of C_6H_6 at hcp-0° sites. All calculated structures were visualized using VESTA [261].

For the adsorption of C_6H_6 on Ir(111) the bridge-30° site had been shown to be the favored and the hexagonal close-packed (hcp) 0° site the second most favored adsorption site [287]. The angles 0° and 30° indicate the angle enclosed by C–C and nearest-neighbor Ir–Ir bonds. Our calculations revealed that the bridge-30° site [Fig. F.1(b)] is energetically preferred to the hcp-0° site [Fig. F.1(g)] by $\approx 100\,\text{meV}$ (Tab. F.2), also in the case of coadsorbed CO (Tab. F.3). Different coverages of C_6H_6 adsorbed at bridge-30° sites were modeled, *i. e.*, 0.16 ML [Fig. F.1(a)], 0.25 ML [Fig. F.1(b)], 0.32 ML [Fig. F.1(c)], 0.50 ML [Fig. F.1(d)].

Furthermore, we compared different configurations of C_6H_6 and CO in the Ir(4×4) supercell. According to our calculations the CO adsorption geometry becomes distorted at small CO–C_6H_6 distances. Figures F.1(e), (f) show that in this case the CO molecule is slightly shifted from the on-top position and exhibits a tilt of its axis with respect to the surface normal. These adsorption configurations of CO and C_6H_6 are energetically less favorable by 50 meV [Fig. F.1(e)] and 320 meV [Fig. F.1(f)] with respect to the configuration depicted in Fig. F.1(b). Consequently, the configurations of Figs. F.1(e), (f) will occur less frequently at room temperature than the configuration of Fig. F.1(b). The aforementioned distortions of the CO adsorption geometry occurred for distances between CO and the closest C atom of an adjacent C_6H_6 molecule lower than $\approx 4.7\,\text{Å}$. Therefore, superstructures with lower distances were omitted from the model calculations regarding the asymmetric line shape of the CO vibrational mode.

F.2 Electronic Properties

Calculated adsorption energies (E_{ads}), work function changes ($\Delta\Phi$) and induced molecular dipole moments (p_z) are summarized for CO on Ir(111) in Tab. F.1, for C_6H_6 on Ir(111) in Tab. F.2, and for coadsorbed CO and C_6H_6 on Ir(111) in Tab. F.3. For an accurate description of the energetics of C_6H_6 on transition metals van der Waals interactions have to be taken into account [288, 289]. Therefore, the exchange-correlation functional optB88-vdW [253, 254] was used in the calculations. In addition, for the sake of comparison with optB88-vdW results, the adsorption energies were determined with the exchange-correlation functional of Perdew, Burke and Ernzerhof (PBE) [219].

In order to calculate the adsorption energies for CO, C_6H_6 and coadsorbed CO, C_6H_6 on Ir(111) the Eqs. (F.1), (F.2), (F.3) were used, respectively.

$$E_{\text{ads}} = \left[E_{\text{Ir(111)+CO}} - E_{\text{Ir(111)}} - n_{\text{CO}} \cdot E_{\text{CO}}\right] / n_{\text{CO}} \tag{F.1}$$

$$E_{\text{ads}} = \left[E_{\text{Ir(111)+C}_6\text{H}_6} - E_{\text{Ir(111)}} - n_{\text{C}_6\text{H}_6} \cdot E_{\text{C}_6\text{H}_6}\right] / n_{\text{C}_6\text{H}_6} \tag{F.2}$$

$$E_{\text{ads}} = E_{\text{Ir(111)+CO+C}_6\text{H}_6} - E_{\text{Ir(111)}} - n_{\text{C}_6\text{H}_6} \cdot E_{\text{C}_6\text{H}_6} - n_{\text{CO}} \cdot E_{\text{CO}} \tag{F.3}$$

Here, n_{CO} and $n_{C_6H_6}$ indicate the number of adsorbed CO and C_6H_6 molecules, respectively. The total energies of the supercells with CO, C_6H_6 and coadsorbed CO and C_6H_6 on Ir(111) are given by $E_{Ir(111)+CO}$, $E_{Ir(111)+C_6H_6}$, and $E_{Ir(111)+CO+C_6H_6}$, respectively. The total energy of the clean Ir(111) surface is represented by $E_{Ir(111)}$, while the total energies of the isolated molecules are E_{CO} and $E_{C_6H_6}$. The latter were calculated in cubic supercells with a side length of 20 Å and using only the Γ point.

Surface dipole moments p_z upon molecule adsorption on Ir(111) were estimated using the work function change $\Delta\Phi = \Phi - \Phi_{Ir(111)}$, where Φ and $\Phi_{Ir(111)}$ are the work functions of the superstructure and the clean Ir(111) surface, respectively. Using the optB88-vdW functional, the work function of the clean Ir(111) surface was determined as $\Phi = 5.83\,\mathrm{eV}$. The calculated work function is virtually not affected by the lateral Ir(111) supercell size. Induced surface dipole moments were then evaluated for CO, C_6H_6 and coadsorbed CO and C_6H_6 on Ir(111) by Eqs. (F.4), (F.5), (F.6), respectively,

$$p_z = -\frac{1}{n_{CO}}\frac{\varepsilon_0 A\Delta\Phi}{\mathrm{e}} \tag{F.4}$$

$$p_z = -\frac{1}{n_{C_6H_6}}\frac{\varepsilon_0 A\Delta\Phi}{\mathrm{e}} \tag{F.5}$$

$$p_z = -\frac{\varepsilon_0 A\Delta\Phi}{\mathrm{e}} \tag{F.6}$$

where ε_0 is the vacuum permittivity, e the elementary charge, and $A = \sqrt{3}/4 \cdot (na)^2$ the supercell area with n the supercell size and $a = 3.886\,\text{Å}$ the lattice constant of Ir determined with the optB88-vdW functional.

Tab. F.1: Calculated adsorption energies (E_{ads}), work function changes ($\Delta\Phi$) and induced dipole moments (p_z) for CO on Ir(111) with different coverages (Θ_{CO}). E_{ads} and p_z represent adsorption energies and dipole moments per molecule. Calculations were performed using the PBE and optB88-vdW (vdW) exchange-correlation functionals.

supercell	Θ_{CO} (ML)	E_{ads} (eV)		$\Delta\Phi$ (eV)	p_z (eÅ)
		PBE	vdW	vdW	vdW
Ir(5 × 5)-CO	1/25	-2.11	-2.17	0.06	-0.05
Ir(4 × 4)-CO	1/16	-2.12	-2.18	0.09	-0.05
Ir(3 × 3)-CO	1/9	-2.11	-2.17	0.15	-0.05
Ir(2 × 2)-CO	1/4	-2.10	-2.16	0.31	-0.05
Ir($\sqrt{3} \times \sqrt{3}$)R30°-CO	1/3	-2.07	-2.15	0.43	-0.05

Tab. F.2: Like Tab. F.1 for C_6H_6 adsorbed on Ir(111).

supercell	$\Theta_{C_6H_6}$ (ML)	E_{ads} (eV)		$\Delta\Phi$ (eV)	p_z (eÅ)
		PBE	vdW	vdW	vdW
Ir(5 × 5)-C_6H_6	4/25	-1.58	-2.40	-0.80	0.73
Ir(4 × 4)-C_6H_6	4/16	-1.52	-2.34	-1.20	0.69
Ir(5 × 5)-2 C_6H_6	8/25	-1.41	-2.24	-1.41	0.64
Ir(4 × 4)-2 C_6H_6	8/16	-0.90	-1.79	-1.85	0.53
Ir(4 × 4)-C_6H_6-I/II	4/16	-1.52	-2.34	-1.20	0.69
Ir(4 × 4)-C_6H_6-III	4/16	-1.41	-2.22	-1.28	0.74

Tab. F.3: Like Tab. F.1 for C_6H_6 and CO on Ir(111). E_{ads} and p_z represent adsorption energies and dipole moments per supercell. The coverage of CO is 0.04 ML for Ir(5 × 5) supercells and 0.06 ML for Ir(4 × 4) supercells.

supercell	$\Theta_{C_6H_6}$ (ML)	E_{ads} (eV)		$\Delta\Phi$ (eV)	p_z (eÅ)
		PBE	vdW	vdW	vdW
Ir(5 × 5)-(C_6H_6+CO)	4/25	-3.67	-4.55	-0.71	0.64
Ir(4 × 4)-(C_6H_6+CO)	4/16	-3.57	-4.47	-0.99	0.57
Ir(5 × 5)-(2 C_6H_6+CO)	8/25	-4.88	-6.61	-1.29	1.17
Ir(4 × 4)-(2 C_6H_6+CO)	8/16	-3.79	-5.67	-1.61	0.93
Ir(4 × 4)-(C_6H_6+CO)-I	4/16	-3.48	-4.42	-0.98	0.57
Ir(4 × 4)-(C_6H_6+CO)-II	4/16	-3.21	-4.15	-1.00	0.58
Ir(4 × 4)-(C_6H_6+CO)-III	4/16	-3.46	-4.35	-1.09	0.63

F.3 Vibrational Properties

Vibrational energies and bond lengths of CO on Ir(111) were calculated as a function of the CO (Tab. F.4) and C_6H_6 (Tab. F.5) coverage using the optB88-vdW exchange-correlation functional. Calculations with this functional resulted in accurate CO vibrational energies. At a CO coverage of ≈ 0.05 ML electron energy loss spectra showed losses at 61 meV and 252 meV which were attributed to Ir–CO and C–O stretch modes. While calculations of the Ir(4 × 4)-CO supercell with the PBE (optPBE-vdW) [253, 254] exchange-correlation functional resulted in vibrational energies of 62.68 meV and 251.12 meV (60.66 meV and 248.50 meV), calculations with the optB88-vdW exchange-correlation functional yielded vibrational energies of 61.85 meV and 252.95 meV, in agreement with the experiment.

Tab. F.4: Calculated vibrational energies of Ir(111)–CO ($E_{\mathrm{vib}}^{\mathrm{Ir–CO}}$) and C–O ($E_{\mathrm{vib}}^{\mathrm{C–O}}$) stretch modes and Ir(111)–C ($l^{\mathrm{Ir–C}}$) and C–O ($l^{\mathrm{C–O}}$) bond lengths as a function of the CO coverage (Θ_{CO}).

supercell	Θ_{CO} (ML)	$E_{\mathrm{vib}}^{\mathrm{Ir–CO}}$ (meV)	$E_{\mathrm{vib}}^{\mathrm{C–O}}$ (meV)	$l^{\mathrm{Ir–C}}$ (Å)	$l^{\mathrm{C–O}}$ (Å)
Ir(5 × 5)-CO	1/25	61.81	252.71	1.853	1.160
Ir(4 × 4)-CO	1/16	61.85	252.95	1.852	1.160
Ir(3 × 3)-CO	1/9	62.07	253.58	1.851	1.160
Ir(2 × 2)-CO	1/4	62.31	256.05	1.851	1.160
Ir($\sqrt{3} \times \sqrt{3}$)$R30°$-CO	1/3	62.28	257.04	1.851	1.161

Tab. F.5: Like Tab. F.4 for different C_6H_6 coverages ($\Theta_{C_6H_6}$). The CO coverage is 0.04 ML (0.06 ML) in Ir(5 × 5) [Ir(4 × 4)] supercells. Distorted CO adsorption geometries and the C_6H_6 hcp-0° adsorption site are considered in rows 5, 6, 7.

supercell	$\Theta_{C_6H_6}$ (ML)	$E_{\mathrm{vib}}^{\mathrm{Ir–CO}}$ (meV)	$E_{\mathrm{vib}}^{\mathrm{C–O}}$ (meV)	$l^{\mathrm{Ir–C}}$ (Å)	$l^{\mathrm{C–O}}$ (Å)
Ir(5 × 5)-(C_6H_6+CO)	4/25	62.36	250.55	1.847	1.163
Ir(4 × 4)-(C_6H_6+CO)	4/16	63.04	248.24	1.841	1.166
Ir(5 × 5)-(2 C_6H_6+CO)	8/25	62.94	248.67	1.843	1.166
Ir(4 × 4)-(2 C_6H_6+CO)	8/16	64.25	244.70	1.831	1.171
Ir(4 × 4)-(C_6H_6+CO)-I	4/16	63.04	246.63	1.839	1.168
Ir(4 × 4)-(C_6H_6+CO)-II	4/16	61.26	244.95	1.851	1.169
Ir(4 × 4)-(C_6H_6+CO)-III	4/16	63.15	248.18	1.841	1.167

Coupling of Dynamic Dipoles

Here, we show that the coupling of dynamic dipoles leads to variations of the C–O stretch mode energy that are negligible compared to the variations due to the electrostatic dipole interactions. As an example, the adsorption of one CO and one C_6H_6 molecule per Ir(4×4) supercell was considered, which corresponds to a CO (C_6H_6) coverage of $\Theta_{CO} = 0.06\,ML$ ($\Theta_{C_6H_6} = 0.25\,ML$).

To evaluate the influence of electrostatic dipole interactions the vibrational energies were calculated for CO (C_6H_6) on Ir(111) [column 1 in Tab. F.6 (Tab. F.7)] and for CO (C_6H_6) on Ir(111) when C_6H_6 (CO) is coadsorbed but not allowed to vibrate [column 2 in Tab. F.6 (Tab. F.7)]. Due to the additional presence of C_6H_6, the C–O stretch mode energy is lowered by 4.71 meV and the Ir(111)–CO stretch mode energy is increased by 1.19 meV (columns 1, 2 in Tab. F.6). In the case of C_6H_6, the additional presence of CO varies all vibrational energies by a maximum of 0.29 meV (columns 1, 2 in Tab. F.7).

The influence of dynamic dipole coupling was unraveled by calculating the CO and C_6H_6 vibrational energies in the coadsorption superstructure when both adsorbates were allowed to vibrate (column 3 in Tabs. F.6, F.7). The differences between separate and simultaneous oscillation of the adsorbates in the coadsorption structure (columns 2, 3 in Tabs. F.6, F.7) can be attributed to dynamic effects. Here, both CO and C_6H_6 vibrational energies differ by a maximum of 0.13 meV which is approximately one order of magnitude lower than the determined electrostatic effects.

Tab. F.6: Calculated vibrational energies of CO (E_{vib}^{CO}) depending on the considered superstructure (first row). During the calculations either one molecular species was allowed to vibrate while the other species was fixed or both species were allowed to vibrate as indicated in the second row. The mode assignment identifies the displacement pattern of the CO vibrations.

supercell	Ir(4×4)-CO	Ir(4×4)-(C_6H_6+CO)		Mode assignment
vibrating species	CO	CO	CO + C_6H_6	
E_{vib}^{CO} (meV)	252.95	248.24	248.25	symm. stretching
	61.85	63.04	63.06	asymm. stretching
	55.45	56.23	56.22	bending in xy-plane
	55.45	55.83	55.83	bending in xy-plane
	7.56	7.22	7.23	rocking in x-direction
	7.50	7.10	6.97	rocking in y-direction

Tab. F.7: Like Tab. F.6 for vibrational energies of C_6H_6 ($E_{vib}^{C_6H_6}$).

supercell	Ir(4 × 4)-C_6H_6		Ir(4 × 4)-(C_6H_6+CO)			
vibrating species	C_6H_6		C_6H_6		C_6H_6 + CO	
$E_{vib}^{C_6H_6}$ (meV)	380.69	42.96	380.59	42.93	380.56	42.91
	380.48	21.03	380.34	21.07	380.33	21.04
	379.32	19.63	379.31	19.65	379.27	19.67
	379.18	19.26	379.21	19.30	379.19	19.31
	374.09		373.97		373.96	
	373.56		373.28		373.28	
	176.36		176.26		176.26	
	170.26		170.17		170.16	
	169.81		169.77		169.76	
	168.41		168.35		168.34	
	161.06		160.98		160.98	
	160.75		160.73		160.72	
	141.70		141.73		141.68	
	140.40		140.34		140.31	
	132.30		132.36		132.31	
	124.72		124.92		124.89	
	117.41		117.48		117.40	
	114.97		115.09		115.05	
	113.30		113.28		113.26	
	111.60		111.70		111.72	
	110.64		110.52		110.49	
	107.44		107.51		107.43	
	104.28		104.55		104.43	
	102.48		102.51		102.50	
	102.19		102.48		102.44	
	77.01		76.96		76.94	
	69.87		69.84		69.85	
	68.38		68.35		68.36	
	63.65		63.62		63.60	
	60.15		60.09		60.06	
	48.13		48.19		48.16	
	47.04		46.94		46.91	

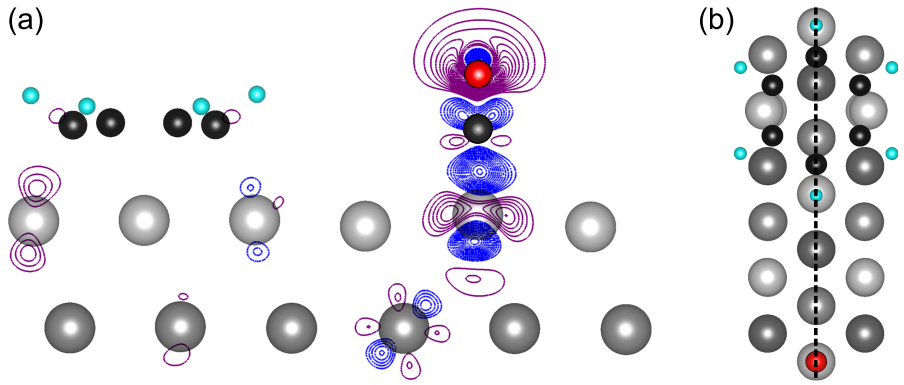

Fig. F.2: (a) Charge density difference $\Delta\varrho(\mathbf{r})$ [Eq. (F.7)] of the Ir(4×4)-(C_6H_6+CO) supercell [Fig. F.1(b)] in the plane indicated by the dashed line in (b). The isolines are drawn in linear scale from $-0.022\,\mathrm{e\AA}^{-3}$ to $0.024\,\mathrm{e\AA}^{-3}$ with an increment of $0.001\,\mathrm{e\AA}^{-3}$, excluding the isoline at $0\,\mathrm{e\AA}^{-3}$. Violet (blue) isolines denote accumulation (depletion) of electrons. **(b)** Top view of the superstructure in (a). The plane of the side view in (a) is indicated by the dashed line.

Intermolecular Charge Transfer

Chemical interaction of the coadsorbed species via charge transfer is a further effect that could potentially contribute to the energy shift of the C–O vibration. Based on calculations of the charge density we will show that this effect does not play a significant role in the shift of the C–O vibrational energy upon coadsorption of C_6H_6 on Ir(111). In Fig. F.2(a) the redistribution of electronic charge due to the coadsorption of CO and C_6H_6 on Ir(111) is illustrated in a plane containing the surface normal and a crystallographic direction [dashed line in Fig. F.2(b)]. The charge density difference was evaluated according to

$$\Delta\varrho(\mathbf{r}) = \varrho_{\mathrm{Ir(111)+CO+C_6H_6}}(\mathbf{r}) - \varrho_{\mathrm{Ir(111)+C_6H_6}}(\mathbf{r}) - \varrho_{\mathrm{Ir(111)+CO}}(\mathbf{r}) + \varrho_{\mathrm{Ir(111)}}(\mathbf{r}) \qquad \text{(F.7)}$$

where each term on the right hand side represents the respective charge density of the system indicated in the subscripts. All charge densities were calculated using the geometry of the coadsorption structure. The absence of strong charge density differences in the Ir lattice and the vacuum region between the molecules indicates negligible indirect and direct charge transfer [Fig. F.2(a)].

The absence of charge transfer between the adsorbed species can also be quantified by a Bader charge analysis [263, 264]. To this end, the Bader charge of CO and C_6H_6 adsorbed alone on Ir(111) is subtracted from the Bader charge of CO and C_6H_6 coadsorbed on Ir(111). The resulting charge differences ΔQ_{CO} and $\Delta Q_{\mathrm{C_6H_6}}$ are listed in Tab. F.8. For CO the Bader charge differences range from $\approx -0.03\,\mathrm{e}$ to $\approx -0.11\,\mathrm{e}$, while for C_6H_6 the

Tab. F.8: Differences in the Bader charges of CO (ΔQ_{CO}) and C_6H_6 ($\Delta Q_{C_6H_6}$) in units of the elementary charge (e) between indicated coadsorbed structures and corresponding structures with exclusively adsorbed CO or C_6H_6, respectively.

supercell	ΔQ_{CO} (e)	$\Delta Q_{C_6H_6}$ (e)
Ir(5 × 5)-(C_6H_6+CO)	-0.030	$1 \cdot 0.006$
Ir(4 × 4)-(C_6H_6+CO)	-0.065	$1 \cdot 0.008$
Ir(5 × 5)-(2 C_6H_6+CO)	-0.054	$2 \cdot 0.008$
Ir(4 × 4)-(2 C_6H_6+CO)	-0.110	$2 \cdot 0.017$

values are at minimum three times lower. This supports the statement that additional charge due to the coadsorption is not transferred between the adsorbed molecules. Rather, charge is only transferred between the individual adsorbates and nearby iridium atoms due to the suggested electrostatic interaction [Fig. F.2(a)].

C_6H_6-Induced Substrate Deformation

Apart from the bonding configuration of the adsorbate the atomic-scale environment plays an important role in its vibrational energies [290]. It was previously shown that surface stress of Cu substrates modified the C–O stretch mode energy [291]. Due to the adsorption of C_6H_6 the Ir(111) surface is slightly deformed. A comparison between the Cartesian coordinates of the Ir(4 × 4)-(C_6H_6+CO) supercell [Fig. F.3(a)] with those of the Ir(4 × 4)-CO supercell [Fig. F.3(c)] shows that Ir atoms are shifted laterally by a maximum of 0.10 Å and vertically by not more than 0.12 Å upon adsorption of C_6H_6.

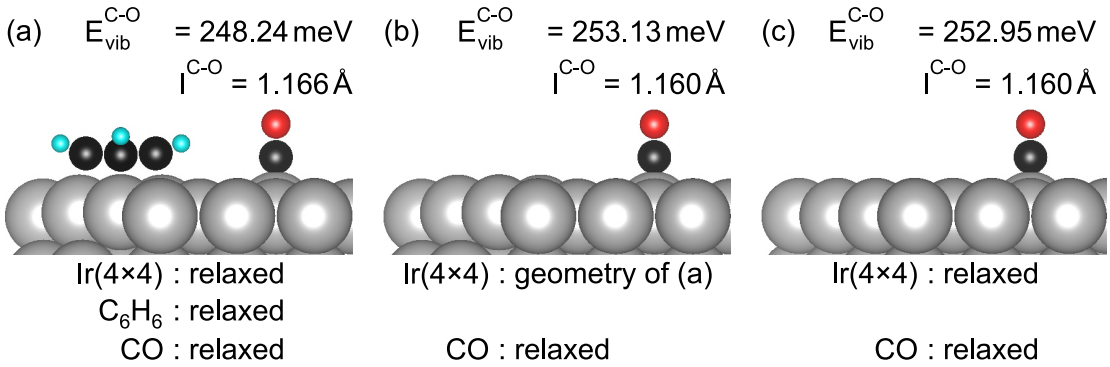

Fig. F.3: Calculated structure to determine the influence of the C_6H_6-induced substrate deformation on the energy shift of the C–O stretch mode. **(a)** Ir(4 × 4)-(C_6H_6+CO). **(b)** Same as (a) after removal of C_6H_6 and relaxation of only C and O. **(c)** Ir(4 × 4)-CO. The corresponding energies of the C–O stretch mode $E_{\mathrm{vib}}^{\mathrm{C–O}}$ and the C–O bond lengths $l^{\mathrm{C–O}}$ for each structure are indicated.

In order to investigate the influence of the C_6H_6-induced substrate deformation on the shift of the C–O stretch mode energy, the C_6H_6 molecule was removed from the Ir(4×4)-(C_6H_6+CO) structure [Fig. F.3(a)]. In a subsequent calculation, only the CO molecule was allowed to relax while the Ir atoms were frozen in the relaxed geometry of the Ir(4×4)-(C_6H_6+CO) structure [Fig. F.3(a)]. After this relaxation [Fig. F.3(b)] the vibrational energy of the C–O stretch mode and the C–O bond length resulted in almost the same values as for the fully relaxed Ir(4×4)-CO structure [Fig. F.3(c)]. Moreover, the C_6H_6-induced deformation induced a slight blueshift ($\approx 0.2\,\mathrm{meV}$) of the vibrational energy rather than a redshift as observed for increasing C_6H_6 coverage. Therefore, the C_6H_6-induced deformation of the Ir(111) surface is not responsible for the observed shift of the C–O stretch mode energy.

List of Figures

List of Tables

List of Publications (2011–2016)

Peer-Reviewed Journal Publications

1. M. Endlich, A. Michl, J. Hildisch, S. Müller, and J. Kröger:
   Energy and Spectroscopic Line Shape of the C–O Stretch Mode on Ir(111) in the Presence of Organic Molecules,
   J. Phys. Chem. C **120**, 11490 (2016).

2. R. J. Koch, S. Fryska, M. Ostler, M. Endlich, F. Speck, T. Hänsel, J. A. Schaefer, and T. Seyller:
   Robust Phonon-Plasmon Coupling in Quasi-Freestanding Graphene on Silicon Carbide,
   Phys. Rev. Lett. **116**, 106802 (2016).

3. M. Endlich, S. Gozdzik, N. Néel, A. L. da Rosa, T. Frauenheim, T. O. Wehling, and J. Kröger:
   Phthalocyanine Adsorption to Graphene on Ir(111): Evidence for Decoupling from Vibrational Spectroscopy,
   J. Chem. Phys. **141**, 184308 (2014).

4. M. Endlich, H. P. C. Miranda, A. Molina-Sánchez, L. Wirtz, and J. Kröger:
   Moiré-Induced Replica of Graphene Phonons on Ir(111),
   Ann. Phys. (Berlin) **526**, 372 (2014).

5. M. Endlich, A. Molina-Sánchez, L. Wirtz, and J. Kröger:
   Screening of Electron-Phonon Coupling in Graphene on Ir(111),
   Phys. Rev. B **88**, 205403 (2013).

6. M. Jahn, M. Müller, M. Endlich, N. Néel, J. Kröger, V. Chis, and B. Hellsing:
   Oxygen Vibrations and Acoustic Surface Plasmon on Be(0001),
   Phys. Rev. B **86**, 085453 (2012).

Given Talks

1. M. Endlich and J. Kröger:
   Investigations into Graphene on Ir(111),
   Special joint seminar on graphene in preparation of a DFG research training group (Ilmenau, Germany, 2014).

2. M. Endlich, A. Molina-Sánchez, H. P. C. Miranda, L. Wirtz, and J. Kröger:
Moiré-Induced Replica Bands of Graphene on Ir(111),
Verhandl. DPG (VI) **49**, 4/O19.3 (Dresden, Germany, 2014).

3. M. Endlich, A. Molina-Sánchez, L. Wirtz, and J. Kröger:
Investigations into Phonons of Graphene on Ir(111),
Seminar of the Institute of Physics (Ilmenau, Germany, 2013).

4. M. Endlich, A. Molina-Sánchez, L. Wirtz, and J. Kröger:
Phonons of Graphene on Ir(111),
Verhandl. DPG (IV) **48**, 3/O68.8 (Regensburg, Germany, 2013).

5. M. Endlich, R. J. Koch, T. Hänsel, T. Seyller and J. A. Schaefer:
Phonon-Plasmon Dispersion of Graphene and Quasi-Freestanding Graphene on 6H-SiC(0001),
Verhandl. DPG (VI) **46**, 1/O51.7 (Dresden, Germany, 2011).

Presented Posters

1. M. Endlich, H. P. C. Miranda, A. Molina-Sánchez, L. Wirtz and J. Kröger:
Investigations into the Dynamical Properties of Graphene on Ir(111),
Workshop on 2D Materials: Fundamentals and Applications (Ilmenau, Germany, 2015).

2. M. Endlich, H. P. C. Miranda, A. Molina-Sánchez, L. Wirtz and J. Kröger:
Investigations into the Dynamical Properties of Graphene on Ir(111),
European Workshop on Epitaxial Graphene and 2D Materials (Primošten, Crotia, 2014).

3. M. Endlich, S. Gozdzik, N. Néel, A. L. da Rosa, T. O. Wehling, and J. Kröger:
Metal-Free Phthalocyanines Adsorbed to Graphene on Ir(111),
563rd Wilhelm-Else-Heraeus seminar on "Functional Molecules at Surfaces" (Bad Honnef, Germany, 2014).

4. M. Endlich, A. Molina-Sánchez, L. Wirtz and J. Kröger:
Dynamical Properties of Graphene on Ir(111),
Colloquium of the Carl-Zeiss foundation (Oberkochen, Germany, 2013).

Bibliography

[1] A. K. Geim and K. S. Novoselov, Nat. Mater. **6**, 183 (2007).

[2] N. D. Mermin, Phys. Rev. **176**, 250 (1968).

[3] K. S. Novoselov, A. K. Geim, S. V. Morozov, D. Jiang, Y. Zhang, S. V. Dubonos, I. V. Grigorieva, and A. A. Firsov, Science **306**, 666 (2004).

[4] J. C. Meyer, A. K. Geim, M. I. Katsnelson, K. S. Novoselov, T. J. Booth, and S. Roth, Nature **446**, 60 (2007).

[5] C. Berger, Z. Song, T. Li, X. Li, A. Y. Ogbazghi, R. Feng, Z. Dai, A. N. Marchenkov, E. H. Conrad, P. N. First, and W. A. de Heer, J. Phys. Chem. B **108**, 19912 (2004).

[6] K. S. Novoselov, D. Jiang, F. Schedin, T. J. Booth, V. V. Khotkevich, S. V. Morozov, and A. K. Geim, Proc. Natl. Acad. Sci. U.S.A. **102**, 10451 (2005).

[7] K. S. Novoselov, A. K. Geim, S. V. Morozov, D. Jiang, M. I. Katsnelson, I. V. Grigorieva, S. V. Dubonos, and A. A. Firsov, Nature **438**, 197 (2005).

[8] Y. Zhang, Y.-W. Tan, H. L. Stormer, and P. Kim, Nature **438**, 201 (2005).

[9] P. R. Wallace, Phys. Rev. **71**, 622 (1947).

[10] A. Bostwick, T. Ohta, T. Seyller, K. Horn, and E. Rotenberg, Nat. Phys. **3**, 36 (2007).

[11] M. Sprinkle, D. Siegel, Y. Hu, J. Hicks, A. Tejeda, A. Taleb-Ibrahimi, P. Le Fèvre, F. Bertran, S. Vizzini, H. Enriquez, S. Chiang, P. Soukiassian, C. Berger, W. A. de Heer, A. Lanzara, and E. H. Conrad, Phys. Rev. Lett. **103**, 226803 (2009).

[12] X. Du, I. Skachko, A. Barker, and E. Y. Andrei, Nat. Nanotechnol. **3**, 491 (2008).

[13] S. V. Morozov, K. S. Novoselov, M. I. Katsnelson, F. Schedin, D. C. Elias, J. A. Jaszczak, and A. K. Geim, Phys. Rev. Lett. **100**, 016602 (2008).

[14] K. I. Bolotin, K. J. Sikes, J. Hone, H. L. Stormer, and P. Kim, Phys. Rev. Lett. **101**, 096802 (2008).

[15] A. S. Mayorov, R. V. Gorbachev, S. V. Morozov, L. Britnell, R. Jalil, L. A. Ponomarenko, P. Blake, K. S. Novoselov, K. Watanabe, T. Taniguchi, and A. K. Geim, Nano Lett. **11**, 2396 (2011).

[16] J. Baringhaus, M. Ruan, F. Edler, A. Tejeda, M. Sicot, A. Taleb-Ibrahimi, A.-P. Li, Z. Jiang, E. H. Conrad, C. Berger, C. Tegenkamp, and W. A. de Heer, Nature **506**, 349 (2014).

[17] A. C. Ferrari, F. Bonaccorso, V. Fal'ko, K. S. Novoselov, S. Roche, P. Bøggild, S. Borini, F. H. L. Koppens, V. Palermo, N. Pugno, J. A. Garrido, R. Sordan, A. Bianco, L. Ballerini, M. Prato, E. Lidorikis, J. Kivioja, C. Marinelli, T. Ryhänen, A. Morpurgo, J. N. Coleman, V. Nicolosi, L. Colombo, A. Fert, M. Garcia-Hernandez, A. Bachtold, G. F. Schneider, F. Guinea, C. Dekker, M. Barbone, Z. Sun, C. Galiotis, A. N. Grigorenko, G. Konstantatos, A. Kis, M. Katsnelson, L. Vandersypen, A. Loiseau, V. Morandi, D. Neumaier, E. Treossi, V. Pellegrini, M. Polini, A. Tredicucci, G. M. Williams, B. H. Hong, J.-H. Ahn, J.-M. Kim, H. Zirath, B. J. van Wees, H. van der Zant, L. Occhipinti, A. Di Matteo, I. A. Kinloch, T. Seyller, E. Quesnel, X. Feng, K. Teo, N. Rupesinghe, P. Hakonen, S. R. T. Neil, Q. Tannock, T. Löfwander, and J. Kinaret, Nanoscale **7**, 4598 (2015).

[18] B. J. Kim, H. Jang, S.-K. Lee, B. H. Hong, J.-H. Ahn, and J. H. Cho, Nano Lett. **10**, 3464 (2010).

[19] J. Lee, T.-J. Ha, H. Li, K. N. Parrish, M. Holt, A. Dodabalapur, R. S. Ruoff, and D. Akinwande, ACS Nano **7**, 7744 (2013).

[20] N. Tombros, C. Jozsa, M. Popinciuc, H. T. Jonkman, and B. J. van Wees, Nature **448**, 571 (2007).

[21] W. Han, R. K. Kawakami, M. Gmitra, and J. Fabian, Nat. Nanotechnol. **9**, 794 (2014).

[22] F. Bonaccorso, Z. Sun, T. Hasan, and A. C. Ferrari, Nat. Photonics **4**, 611 (2010).

[23] M. Freitag, T. Low, F. Xia, and P. Avouris, Nat. Photonics **7**, 53 (2013).

[24] K. S. Novoselov, V. I. Fal'ko, L. Colombo, P. R. Gellert, M. G. Schwab, and K. Kim, Nature **490**, 192 (2012).

[25] J. Wintterlin and M.-L. Bocquet, Surf. Sci. **603**, 1841 (2009).

[26] M. Batzill, Surf. Sci. Rep. **67**, 83 (2012).

[27] C. Busse, P. Lazić, R. Djemour, J. Coraux, T. Gerber, N. Atodiresei, V. Caciuc, R. Brako, A. T. N'Diaye, S. Blügel, J. Zegenhagen, and T. Michely, Phys. Rev. Lett. **107**, 036101 (2011).

[28] P. Sutter, J. T. Sadowski, and E. Sutter, Phys. Rev. B **80**, 245411 (2009).

[29] I. Pletikosić, M. Kralj, P. Pervan, R. Brako, J. Coraux, A. T. N'Diaye, C. Busse, and T. Michely, Phys. Rev. Lett. **102**, 056808 (2009).

[30] J. Coraux, A. T. N'Diaye, C. Busse, and T. Michely, Nano Lett. **8**, 565 (2008).

[31] A. T. N'Diaye, J. Coraux, T. N. Plasa, C. Busse, and T. Michely, New J. Phys. **10**, 043033 (2008).

[32] H. Chen, W. Zhu, and Z. Zhang, Phys. Rev. Lett. **104**, 186101 (2010).

[33] M. Pozzo, D. Alfè, P. Lacovig, P. Hofmann, S. Lizzit, and A. Baraldi, Phys. Rev. Lett. **106**, 135501 (2011).

[34] S. Runte, P. Lazić, C. Vo-Van, J. Coraux, J. Zegenhagen, and C. Busse, Phys. Rev. B **89**, 155427 (2014).

[35] M. Kralj, I. Pletikosić, M. Petrović, P. Pervan, M. Milun, A. T. N'Diaye, C. Busse, T. Michely, J. Fujii, and I. Vobornik, Phys. Rev. B **84**, 075427 (2011).

[36] P. Lacovig, M. Pozzo, D. Alfè, P. Vilmercati, A. Baraldi, and S. Lizzit, Phys. Rev. Lett. **103**, 166101 (2009).

[37] S. K. Hämäläinen, Z. Sun, M. P. Boneschanscher, A. Uppstu, M. Ijäs, A. Harju, D. Vanmaekelbergh, and P. Liljeroth, Phys. Rev. Lett. **107**, 236803 (2011).

[38] D. Subramaniam, F. Libisch, Y. Li, C. Pauly, V. Geringer, R. Reiter, T. Mashoff, M. Liebmann, J. Burgdörfer, C. Busse, T. Michely, R. Mazzarello, M. Pratzer, and M. Morgenstern, Phys. Rev. Lett. **108**, 046801 (2012).

[39] S. J. Altenburg, J. Kröger, T. O. Wehling, B. Sachs, A. I. Lichtenstein, and R. Berndt, Phys. Rev. Lett. **108**, 206805 (2012).

[40] F. Craes, S. Runte, J. Klinkhammer, M. Kralj, T. Michely, and C. Busse, Phys. Rev. Lett. **111**, 056804 (2013).

[41] Z. Yao, C. L. Kane, and C. Dekker, Phys. Rev. Lett. **84**, 2941 (2000).

[42] A. Javey, J. Guo, M. Paulsson, Q. Wang, D. Mann, M. Lundstrom, and H. Dai, Phys. Rev. Lett. **92**, 106804 (2004).

[43] T. Stauber, N. M. R. Peres, and F. Guinea, Phys. Rev. B **76**, 205423 (2007).

[44] F. T. Vasko and V. Ryzhii, Phys. Rev. B **76**, 233404 (2007).

[45] A. Barreiro, M. Lazzeri, J. Moser, F. Mauri, and A. Bachtold, Phys. Rev. Lett. **103**, 076601 (2009).

[46] E. Mariani and F. von Oppen, Phys. Rev. Lett. **100**, 076801 (2008).

[47] E. V. Castro, H. Ochoa, M. I. Katsnelson, R. V. Gorbachev, D. C. Elias, K. S. Novoselov, A. K. Geim, and F. Guinea, Phys. Rev. Lett. **105**, 266601 (2010).

[48] S. Marchini, S. Günther, and J. Wintterlin, Phys. Rev. B **76**, 075429 (2007).

[49] M. Gao, Y. Pan, L. Huang, H. Hu, L. Z. Zhang, H. M. Guo, S. X. Du, and H.-J. Gao, Appl. Phys. Lett. **98**, 033101 (2011).

[50] L. Meng, R. Wu, L. Zhang, L. Li, S. Du, Y. Wang, and H.-J. Gao, J. Phys.: Condens. Matter **24**, 314214 (2012).

[51] C.-H. Park, L. Yang, Y.-W. Son, M. L. Cohen, and S. G. Louie, Nat. Phys. **4**, 213 (2008).

[52] C.-H. Park, L. Yang, Y.-W. Son, M. L. Cohen, and S. G. Louie, Phys. Rev. Lett. **101**, 126804 (2008).

[53] F. Guinea, M. I. Katsnelson, and M. A. H. Vozmediano, Phys. Rev. B **77**, 075422 (2008).

[54] C.-H. Park, Y.-W. Son, L. Yang, M. L. Cohen, and S. G. Louie, Phys. Rev. Lett. **103**, 046808 (2009).

[55] L. Brey and H. A. Fertig, Phys. Rev. Lett. **103**, 046809 (2009).

[56] T. G. Pedersen, C. Flindt, J. Pedersen, N. A. Mortensen, A.-P. Jauho, and K. Pedersen, Phys. Rev. Lett. **100**, 136804 (2008).

[57] F. Rosei, M. Schunack, Y. Naitoh, P. Jiang, A. Gourdon, E. Laegsgaard, I. Stensgaard, C. Joachim, and F. Besenbacher, Prog. Surf. Sci. **71**, 95 (2003).

[58] S. M. Barlow and R. Raval, Surf. Sci. Rep. **50**, 201 (2003).

[59] F. S. Tautz, Prog. Surf. Sci. **82**, 479 (2007).

[60] C. Morin, D. Simon, and P. Sautet, J. Phys. Chem. B **107**, 2995 (2003).

[61] A. Hauschild, K. Karki, B. C. C. Cowie, M. Rohlfing, F. S. Tautz, and M. Sokolowski, Phys. Rev. Lett. **94**, 036106 (2005).

[62] L. Romaner, G. Heimel, J.-L. Brédas, A. Gerlach, F. Schreiber, R. L. Johnson, J. Zegenhagen, S. Duhm, N. Koch, and E. Zojer, Phys. Rev. Lett. **99**, 256801 (2007).

[63] L. Kilian, A. Hauschild, R. Temirov, S. Soubatch, A. Schöll, A. Bendounan, F. Reinert, T.-L. Lee, F. S. Tautz, M. Sokolowski, and E. Umbach, Phys. Rev. Lett. **100**, 136103 (2008).

[64] Y. Wang, J. Kröger, R. Berndt, and W. A. Hofer, Angew. Chem. Int. Ed. **48**, 1261 (2009).

[65] J. Brede, N. Atodiresei, S. Kuck, P. Lazić, V. Caciuc, Y. Morikawa, G. Hoffmann, S. Blügel, and R. Wiesendanger, Phys. Rev. Lett. **105**, 047204 (2010).

[66] R. Cuadrado, J. I. Cerdá, Y. Wang, G. Xin, R. Berndt, and H. Tang, J. Chem. Phys. **133**, 154701 (2010).

[67] E. Ćavar, M.-C. Blüm, M. Pivetta, F. Patthey, M. Chergui, and W.-D. Schneider, Phys. Rev. Lett. **95**, 196102 (2005).

[68] K. J. Franke, G. Schulze, N. Henningsen, I. Fernández-Torrente, J. I. Pascual, S. Zarwell, K. Rück-Braun, M. Cobian, and N. Lorente, Phys. Rev. Lett. **100**, 036807 (2008).

[69] X. H. Qiu, G. V. Nazin, and W. Ho, Science **299**, 542 (2003).

[70] N. Nilius, T. M. Wallis, and W. Ho, Phys. Rev. Lett. **90**, 046808 (2003).

[71] X. H. Qiu, G. V. Nazin, and W. Ho, Phys. Rev. Lett. **92**, 206102 (2004).

[72] A. J. Heinrich, J. A. Gupta, C. P. Lutz, and D. M. Eigler, Science **306**, 466 (2004).

[73] G. V. Nazin, S. W. Wu, and W. Ho, Proc. Natl. Acad. Sci. U.S.A. **102**, 8832 (2005).

[74] J. Repp, G. Meyer, S. M. Stojković, A. Gourdon, and C. Joachim, Phys. Rev. Lett. **94**, 026803 (2005).

[75] J. Repp, G. Meyer, S. Paavilainen, F. E. Olsson, and M. Persson, Phys. Rev. Lett. **95**, 225503 (2005).

[76] P. Liljeroth, J. Repp, and G. Meyer, Science **317**, 1203 (2007).

[77] Y. Wang, J. Kröger, R. Berndt, and H. Tang, J. Am. Chem. Soc. **132**, 12546 (2010).

[78] J. Zhao, C. Zeng, X. Cheng, K. Wang, G. Wang, J. Yang, J. G. Hou, and Q. Zhu, Phys. Rev. Lett. **95**, 045502 (2005).

[79] B. Li, C. Zeng, J. Zhao, J. Yang, J. G. Hou, and Q. Zhu, J. Chem. Phys. **124**, 064709 (2006).

[80] C. F. Hirjibehedin, C. P. Lutz, and A. J. Heinrich, Science **312**, 1021 (2006).

[81] F. Matino, G. Schull, F. Köhler, S. Gabutti, M. Mayor, and R. Berndt, Proc. Natl. Acad. Sci. U.S.A. **108**, 961 (2011).

[82] F. Schedin, A. K. Geim, S. V. Morozov, E. W. Hill, P. Blake, M. I. Katsnelson, and K. S. Novoselov, Nat. Mater. **6**, 652 (2007).

[83] W. Chen, S. Chen, D. C. Qi, X. Y. Gao, and A. T. S. Wee, J. Am. Chem. Soc. **129**, 10418 (2007).

[84] T. O. Wehling, K. S. Novoselov, S. V. Morozov, E. E. Vdovin, M. I. Katsnelson, A. K. Geim, and A. I. Lichtenstein, Nano Lett. **8**, 173 (2008).

[85] O. Leenaerts, B. Partoens, and F. M. Peeters, Phys. Rev. B **77**, 125416 (2008).

[86] S. Y. Zhou, D. A. Siegel, A. V. Fedorov, and A. Lanzara, Phys. Rev. Lett. **101**, 086402 (2008).

[87] R. Voggu, B. Das, C. S. Rout, and C. N. R. Rao, J. Phys.: Condens. Matter **20**, 472204 (2008).

[88] D. B. Farmer, R. Golizadeh-Mojarad, V. Perebeinos, Y.-M. Lin, G. S. Tulevski, J. C. Tsang, and P. Avouris, Nano Lett. **9**, 388 (2009).

[89] S. K. Saha, R. C. Chandrakanth, H. R. Krishnamurthy, and U. V. Waghmare, Phys. Rev. B **80**, 155414 (2009).

[90] C. Coletti, C. Riedl, D. S. Lee, B. Krauss, L. Patthey, K. von Klitzing, J. H. Smet, and U. Starke, Phys. Rev. B **81**, 235401 (2010).

[91] G. Hong, Q.-H. Wu, J. Ren, C. Wang, W. Zhang, and S.-T. Lee, Nano Today **8**, 388 (2013).

[92] Q. H. Wang and M. C. Hersam, Nat. Chem. **1**, 206 (2009).

[93] H. Huang, S. Chen, X. Gao, W. Chen, and A. T. S. Wee, ACS Nano **3**, 3431 (2009).

[94] S. Barja, M. Garnica, J. J. Hinarejos, A. L. Vázquez de Parga, N. Martín, and R. Miranda, Chem. Commun. **46**, 8198 (2010).

[95] J. Mao, H. Zhang, Y. Jiang, Y. Pan, M. Gao, W. Xiao, and H.-J. Gao, J. Am. Chem. Soc. **131**, 14136 (2009).

[96] A. J. Pollard, E. W. Perkins, N. A. Smith, A. Saywell, G. Goretzki, A. G. Phillips, S. P. Argent, H. Sachdev, F. Müller, S. Hüfner, S. Gsell, M. Fischer, M. Schreck, J. Osterwalder, T. Greber, S. Berner, N. R. Champness, and P. H. Beton, Angew. Chem. Int. Ed. **49**, 1794 (2010).

[97] M. Roos, D. Künzel, B. Uhl, H.-H. Huang, O. Brandao Alves, H. E. Hoster, A. Gross, and R. J. Behm, J. Am. Chem. Soc. **133**, 9208 (2011).

[98] X. Ling, L. Xie, Y. Fang, H. Xu, H. Zhang, J. Kong, M. S. Dresselhaus, J. Zhang, and Z. Liu, Nano Lett. **10**, 553 (2010).

[99] W. Dou, S. Huang, R. Q. Zhang, and C. S. Lee, J. Chem. Phys. **134**, 094705 (2011).

[100] X. Ling, L. G. Moura, M. A. Pimenta, and J. Zhang, J. Phys. Chem. C **116**, 25112 (2012).

[101] D. C. Langreth, Phys. Rev. Lett. **54**, 126 (1985).

[102] J. Kröger, Rep. Prog. Phys. **69**, 899 (2006).

[103] R. G. Musket, W. McLean, C. A. Colmenares, D. M. Makowiecki, and W. J. Siekhaus, Appl. Surf. Sci. **10**, 143 (1982).

[104] J. Coraux, A. T. N'Diaye, M. Engler, C. Busse, D. Wall, N. Buckanie, F.-J. Meyer zu Heringdorf, R. van Gastel, B. Poelsema, and T. Michely, New J. Phys. **11**, 023006 (2009).

[105] S. Lizzit and A. Baraldi, Catal. Today **154**, 68 (2010).

[106] R. van Gastel, A. T. N'Diaye, D. Wall, J. Coraux, C. Busse, N. M. Buckanie, F.-J. Meyer zu Heringdorf, M. Horn-von Hoegen, T. Michely, and B. Poelsema, Appl. Phys. Lett. **95**, 121901 (2009).

[107] A. T. N'Diaye, R. van Gastel, A. J. Martínez-Galera, J. Coraux, H. Hattab, D. Wall, F.-J. Meyer zu Heringdorf, M. Horn-von Hoegen, J. M. Gómez-Rodríquez, B. Poelsema, C. Busse, and T. Michely, New J. Phys. **11**, 113056 (2009).

[108] H. Hattab, A. T. N'Diaye, D. Wall, G. Jnawali, J. Coraux, C. Busse, R. van Gastel, B. Poelsema, T. Michely, F.-J. Meyer zu Heringdorf, and M. Horn-von Hoegen, Appl. Phys. Lett. **98**, 141903 (2011).

[109] H. Hattab, A. T. N'Diaye, D. Wall, C. Klein, G. Jnawali, J. Coraux, C. Busse, R. van Gastel, B. Poelsema, T. Michely, F.-J. Meyer zu Heringdorf, and M. Horn-von Hoegen, Nano Lett. **12**, 678 (2012).

[110] P. C. Rogge, S. Nie, K. F. McCarty, N. C. Bartelt, and O. D. Dubon, Nano Lett. **15**, 170 (2015).

[111] P. C. Rogge, K. Thürmer, M. E. Foster, K. F. McCarty, O. D. Dubon, and N. C. Bartelt, Nat. Commun. **6**, 6880 (2015).

[112] A. G. MacKay, Aust. J. Chem. **26**, 2425 (1973).

[113] S. L. Selvaraj and F. P. Xavier, J. Cryst. Growth **225**, 168 (2001).

[114] F. M. Propst and T. C. Piper, J. Vac. Sci. Technol. **4**, 53 (1967).

[115] H. Steininger, S. Lehwald, and H. Ibach, Surf. Sci. **123**, 264 (1982).

[116] H. Ibach, Phys. Rev. Lett. **24**, 1416 (1970).

[117] S. Lehwald, J. M. Szeftel, H. Ibach, T. S. Rahman, and D. L. Mills, Phys. Rev. Lett. **50**, 518 (1983).

[118] K.-D. Tsuei, E. W. Plummer, A. Liebsch, K. Kempa, and P. Bakshi, Phys. Rev. Lett. **64**, 44 (1990).

[119] J. A. Gaspar, A. G. Eguiluz, K.-D. Tsuei, and E. W. Plummer, Phys. Rev. Lett. **67**, 2854 (1991).

[120] A. Lucas, G. Gensterblum, J. J. Pireaux, P. A. Thiry, R. Caudano, J. P. Vigneron, P. Lambin, and W. Krätschmer, Phys. Rev. B **45**, 13694 (1992).

[121] R. Vollmer, M. Etzkorn, P. S. Anil Kumar, H. Ibach, and J. Kirschner, Phys. Rev. Lett. **91**, 147201 (2003).

[122] J. Rajeswari, H. Ibach, and C. M. Schneider, Phys. Rev. Lett. **112**, 127202 (2014).

[123] H. Ibach, (1982), U.S. Patent 4309607 A.

[124] H. Ibach, H.-D. Bruchmann, and S. Lehwald, (1989), U.S. Patent 4845361 A.

[125] H. Ibach, H.-D. Bruchmann, and S. Lehwald, (1994), U.S. Patent 5357107 A.

[126] H. Ibach, *Electron Energy Loss Spectrometers: The Technology of High Performance*, Springer Series in Optical Sciences, Vol. 63 (Springer, Berlin, 1991).

[127] H. Ibach, J. Electron Spectrosc. Relat. Phenom. **64-65**, 819 (1993).

[128] H. Ibach, M. Balden, and S. Lehwald, J. Chem. Soc., Faraday Trans. **92**, 4771 (1996).

[129] H. Ibach and D. L. Mills, *Electron Energy Loss Spectroscopy and Surface Vibrations* (Academic Press, New York, 1982).

[130] H. Ibach, J. Rajeswari, and C. M. Schneider, Rev. Sci. Instrum. **82**, 123904 (2011).

[131] *SPECS DELTA 0.5 Manual: Instrumentation and Software*, SPECS Surface Nano Analysis GmbH, Berlin (2002).

[132] H. Lüth, *Solid Surfaces, Interfaces and Thin Films*, 5th ed. (Springer, Berlin, 2010).

[133] H. Ibach and J. Rajeswari, J. Electron Spectrosc. Relat. Phenom. **185**, 61 (2012).

[134] H. Ibach, Phys. Rev. Lett. **27**, 253 (1971).

[135] A. A. Lucas and M. Šunjić, Phys. Rev. Lett. **26**, 229 (1971).

[136] E. Evans and D. L. Mills, Phys. Rev. B **5**, 4126 (1972).

[137] E. Evans and D. L. Mills, Phys. Rev. B **7**, 853 (1973).

[138] D. L. Mills, Surf. Sci. **48**, 59 (1975).

[139] D. Šokčević, Z. Lenac, R. Brako, and M. Šunjić, Z. Phys. B: Condens. Matter **28**, 273 (1977).

[140] B. N. J. Persson, Solid State Commun. **24**, 573 (1977).

[141] F. Delanaye, A. A. Lucas, and G. D. Mahan, Surf. Sci. **70**, 629 (1978).

[142] Z. Lenac, M. Šunjić, D. Šokčević, and R. Brako, Surf. Sci. **80**, 602 (1979).

[143] B. N. J. Persson, Surf. Sci. **92**, 265 (1980).

[144] P. Avouris and J. Demuth, Annu. Rev. Phys. Chem. **35**, 49 (1984).

[145] P. A. Thiry, M. Liehr, J. J. Pireaux, and R. Caudano, Phys. Scr. **35**, 368 (1987).

[146] C. H. Li, S. Y. Tong, and D. L. Mills, Phys. Rev. B **21**, 3057 (1980).

[147] S. Y. Tong, C. H. Li, and D. L. Mills, Phys. Rev. Lett. **44**, 407 (1980).

[148] F. Fromm, M. H. Oliveira, Jr., A. Molina-Sánchez, M. Hundhausen, J. M. J. Lopes, H. Riechert, L. Wirtz, and T. Seyller, New J. Phys. **15**, 043031 (2013).

[149] A. Allard and L. Wirtz, Nano Lett. **10**, 4335 (2010).

[150] S. Piscanec, M. Lazzeri, F. Mauri, A. C. Ferrari, and J. Robertson, Phys. Rev. Lett. **93**, 185503 (2004).

[151] E. Starodub, A. Bostwick, L. Moreschini, S. Nie, F. El Gabaly, K. F. McCarty, and E. Rotenberg, Phys. Rev. B **83**, 125428 (2011).

[152] A. Politano, A. R. Marino, and G. Chiarello, J. Phys.: Condens. Matter **24**, 104025 (2012).

[153] X. Gonze, J.-M. Beuken, R. Caracas, F. Detraux, M. Fuchs, G.-M. Rignanese, L. Sindic, M. Verstraete, G. Zérah, F. Jollet, M. Torrent, A. Roy, M. Mikami, P. Ghosez, J.-Y. Raty, and D. C. Allan, Comput. Mater. Sci. **25**, 478 (2002).

[154] X. Gonze and C. Lee, Phys. Rev. B **55**, 10355 (1997).

[155] S. Baroni, S. de Gironcoli, A. Dal Corso, and P. Giannozzi, Rev. Mod. Phys. **73**, 515 (2001).

[156] P. J. Feibelman, Phys. Rev. B **77**, 165419 (2008).

[157] I. Horcas, R. Fernández, J. M. Gómez-Rodríguez, J. Colchero, J. Gómez-Herrero, and A. M. Baro, Rev. Sci. Instrum. **78**, 013705 (2007).

[158] A. Varykhalov, D. Marchenko, M. R. Scholz, E. D. L. Rienks, T. K. Kim, G. Bihlmayer, J. Sánchez-Barriga, and O. Rader, Phys. Rev. Lett. **108**, 066804 (2012).

[159] L. Wirtz and A. Rubio, Solid State Commun. **131**, 141 (2004).

[160] M. Lazzeri, C. Attaccalite, L. Wirtz, and F. Mauri, Phys. Rev. B **78**, 081406 (2008).

[161] J. Maultzsch, S. Reich, C. Thomsen, H. Requardt, and P. Ordejón, Phys. Rev. Lett. **92**, 075501 (2004).

[162] A. Grüneis, J. Serrano, A. Bosak, M. Lazzeri, S. L. Molodtsov, L. Wirtz, C. Attaccalite, M. Krisch, A. Rubio, F. Mauri, and T. Pichler, Phys. Rev. B **80**, 085423 (2009).

[163] W. Kohn, Phys. Rev. Lett. **2**, 393 (1959).

[164] B. Hellsing, A. Eiguren, and E. V. Chulkov, J. Phys.: Condens. Matter **14**, 5959 (2002).

[165] E. W. Plummer, J. Shi, S.-J. Tang, E. Rotenberg, and S. D. Kevan, Prog. Surf. Sci. **74**, 251 (2003).

[166] M. Lazzeri and F. Mauri, Phys. Rev. Lett. **97**, 266407 (2006).

[167] A. Politano, A. R. Marino, V. Formoso, and G. Chiarello, Carbon **50**, 734 (2012).

[168] A. Marini, C. Hogan, M. Grüning, and D. Varsano, Comput. Phys. Commun. **180**, 1392 (2009).

[169] M. Cazzaniga, L. Caramella, N. Manini, and G. Onida, Phys. Rev. B **82**, 035104 (2010).

[170] C. Attaccalite, L. Wirtz, M. Lazzeri, F. Mauri, and A. Rubio, Nano Lett. **10**, 1172 (2010).

[171] T. Aizawa, R. Souda, Y. Ishizawa, H. Hirano, T. Yamada, K. Tanaka, and C. Oshima, Surf. Sci. **237**, 194 (1990).

[172] A. M. Shikin, D. Farías, V. K. Adamchuk, and K.-H. Rieder, Surf. Sci. **424**, 155 (1999).

[173] Y. S. Dedkov and M. Fonin, New J. Phys. **12**, 125004 (2010).

[174] D. Eom, D. Prezzi, K. T. Rim, H. Zhou, M. Lefenfeld, S. Xiao, C. Nuckolls, M. S. Hybertsen, T. F. Heinz, and G. W. Flynn, Nano Lett. **9**, 2844 (2009).

[175] A. T. N'Diaye, S. Bleikamp, P. J. Feibelman, and T. Michely, Phys. Rev. Lett. **97**, 215501 (2006).

[176] M. Sicot, S. Bouvron, O. Zander, U. Rüdiger, Y. S. Dedkov, and M. Fonin, Appl. Phys. Lett. **96**, 093115 (2010).

[177] H. G. Zhang, J. T. Sun, T. Low, L. Z. Zhang, Y. Pan, Q. Liu, J. H. Mao, H. T. Zhou, H. M. Guo, S. X. Du, F. Guinea, and H.-J. Gao, Phys. Rev. B **84**, 245436 (2011).

[178] J. Sánchez-Barriga, A. Varykhalov, D. Marchenko, M. R. Scholz, and O. Rader, Phys. Rev. B **85**, 201413 (2012).

[179] R. Heid and K.-P. Bohnen, Phys. Rep. **387**, 151 (2003).

[180] M. Endlich, A. Molina-Sánchez, L. Wirtz, and J. Kröger, Phys. Rev. B **88**, 205403 (2013).

[181] T. Aizawa, R. Souda, S. Otani, Y. Ishizawa, and C. Oshima, Phys. Rev. B **42**, 11469 (1990).

[182] M. Mohr, J. Maultzsch, E. Dobardžić, S. Reich, I. Milošević, M. Damnjanović, A. Bosak, M. Krisch, and C. Thomsen, Phys. Rev. B **76**, 035439 (2007).

[183] K. Yamamoto, M. Fukushima, T. Osaka, and C. Oshima, Phys. Rev. B **45**, 11358 (1992).

[184] A. Politano, F. de Juan, G. Chiarello, and H. A. Fertig, Phys. Rev. Lett. **115**, 075504 (2015).

[185] C. Leznoff and A. B. P. Lever, *Phthalocyanines: Properties and Applications* (VCH, Weinheim, 1989).

[186] K. M. Khadis, K. M. Smith, and R. Guilard, *The Porphyrin Handbook* (Academic Press, Boston, 1999).

[187] S. R. Forrest, Chem. Rev. **97**, 1793 (1997).

[188] N. R. Armstrong, J. Porphyrins Phthalocyanines **4**, 414 (2000).

[189] D. E. Hooks, T. Fritz, and M. D. Ward, Adv. Mater. **13**, 227 (2001).

[190] J. Kröger, H. Jensen, R. Berndt, R. Rurali, and N. Lorente, Chem. Phys. Lett. **438**, 249 (2007).

[191] E. V. Tsiper, Z. G. Soos, W. Gao, and A. Kahn, Chem. Phys. Lett. **360**, 47 (2002).

[192] S. Berner, M. de Wild, L. Ramoino, S. Ivan, A. Baratoff, H.-J. Güntherodt, H. Suzuki, D. Schlettwein, and T. A. Jung, Phys. Rev. B **68**, 115410 (2003).

[193] Y. Wang, R. Yamachika, A. Wachowiak, M. Grobis, and M. F. Crommie, Nat. Mater. **7**, 194 (2008).

[194] M. Häming, C. Scheuermann, A. Schöll, F. Reinert, and E. J. Umbach, J. Electron Spectrosc. Relat. Phenom. **174**, 59 (2009).

[195] T. G. Gopakumar, T. Brumme, J. Kröger, C. Toher, G. Cuniberti, and R. Berndt, J. Phys. Chem. C **115**, 12173 (2011).

[196] J. Cho, J. Smerdon, L. Gao, Ö. Süzer, J. R. Guest, and N. P. Guisinger, Nano Lett. **12**, 3018 (2012).

[197] M. Scardamaglia, S. Lisi, S. Lizzit, A. Baraldi, R. Larciprete, C. Mariani, and M. G. Betti, J. Phys. Chem. C **117**, 3019 (2013).

[198] S. Yoshimoto and N. Kobayashi, in *Functional Phthalocyanine Molecular Materials*, Structure and Bonding, Vol. 135 (Springer, Berlin, 2010) pp. 137–167.

[199] J. Ren, S. Meng, Y.-L. Wang, X.-C. Ma, Q.-K. Xue, and E. Kaxiras, J. Chem. Phys. **134**, 194706 (2011).

[200] K. Yang, W. D. Xiao, Y. H. Jiang, H. G. Zhang, L. W. Liu, J. H. Mao, H. T. Zhou, S. X. Du, and H.-J. Gao, J. Phys. Chem. C **116**, 14052 (2012).

[201] S. K. Hämäläinen, M. Stepanova, R. Drost, P. Liljeroth, J. Lahtinen, and J. Sainio, J. Phys. Chem. C **116**, 20433 (2012).

[202] P. Järvinen, S. K. Hämäläinen, K. Banerjee, P. Häkkinen, M. Ijäs, A. Harju, and P. Liljeroth, Nano Lett. **13**, 3199 (2013).

[203] W. Kohn and L. J. Sham, Phys. Rev. **140**, A1133 (1965).

[204] M. J. Frisch, G. W. Trucks, H. B. Schlegel, G. E. Scuseria, M. A. Robb, J. R. Cheeseman, G. Scalmani, V. Barone, B. Mennucci, G. A. Petersson, H. Nakatsuji, M. Caricato, X. Li, H. P. Hratchian, A. F. Izmaylov, J. Bloino, G. Zheng, J. L. Sonnenberg, M. Hada, M. Ehara, K. Toyota, R. Fukuda, J. Hasegawa, M. Ishida, T. Nakajima, Y. Honda, O. Kitao, H. Nakai, T. Vreven, J. A. Montgomery, Jr.,

J. E. Peralta, F. Ogliaro, M. Bearpark, J. J. Heyd, E. Brothers, K. N. Kudin, V. N. Staroverov, R. Kobayashi, J. Normand, K. Raghavachari, A. Rendell, J. C. Burant, S. S. Iyengar, J. Tomasi, M. Cossi, N. Rega, J. M. Millam, M. Klene, J. E. Knox, J. B. Cross, V. Bakken, C. Adamo, J. Jaramillo, R. Gomperts, R. E. Stratmann, O. Yazyev, A. J. Austin, R. Cammi, C. Pomelli, J. W. Ochterski, R. L. Martin, K. Morokuma, V. G. Zakrzewski, G. A. Voth, P. Salvador, J. J. Dannenberg, S. Dapprich, A. D. Daniels, Ö. Farkas, J. B. Foresman, J. V. Ortiz, J. Cioslowski, and D. J. Fox, *Gaussian 09 Revision A.02* (Gaussian Inc., Wallingford CT, 2009).

[205] A. D. Becke, J. Chem. Phys. **98**, 5648 (1993).

[206] A. D. McLean and G. S. Chandler, J. Chem. Phys. **72**, 5639 (1980).

[207] R. Krishnan, J. S. Binkley, R. Seeger, and J. A. Pople, J. Chem. Phys. **72**, 650 (1980).

[208] Y. J. Chabal, Phys. Rev. Lett. **55**, 845 (1985).

[209] C. J. Hirschmugl, G. P. Williams, F. M. Hoffmann, and Y. J. Chabal, Phys. Rev. Lett. **65**, 480 (1990).

[210] J. Kröger, S. Lehwald, and H. Ibach, Phys. Rev. B **55**, 10895 (1997).

[211] J. Kröger, D. Bruchmann, S. Lehwald, and H. Ibach, Surf. Sci. **449**, 227 (2000).

[212] F. S. Tautz, M. Eremtchenko, J. A. Schaefer, M. Sokolowski, V. Shklover, and E. Umbach, Phys. Rev. B **65**, 125405 (2002).

[213] S. H. Chang, S. Kuck, J. Brede, L. Lichtenstein, G. Hoffmann, and R. Wiesendanger, Phys. Rev. B **78**, 233409 (2008).

[214] P. Amsalem, L. Giovanelli, J. M. Themlin, and T. Angot, Phys. Rev. B **79**, 235426 (2009).

[215] Y. Wang, X. Ge, C. Manzano, J. Kröger, R. Berndt, W. A. Hofer, H. Tang, and J. Cerda, J. Am. Chem. Soc. **131**, 10400 (2009).

[216] P. E. Blöchl, Phys. Rev. B **50**, 17953 (1994).

[217] G. Kresse and J. Hafner, J. Phys.: Condens. Matter **6**, 8245 (1994).

[218] G. Kresse and D. Joubert, Phys. Rev. B **59**, 1758 (1999).

[219] J. P. Perdew, K. Burke, and M. Ernzerhof, Phys. Rev. Lett. **77**, 3865 (1996).

[220] A. Tkatchenko and M. Scheffler, Phys. Rev. Lett. **102**, 073005 (2009).

[221] V. Palermo, Chem. Commun. **49**, 2848 (2013).

[222] T. G. Gopakumar, T. Davran-Candan, J. Bahrenburg, R. J. Maurer, F. Temps, K. Reuter, and R. Berndt, Angew. Chem. Int. Ed. **52**, 11007 (2013).

[223] C. G. Barraclough, R. L. Martin, S. Mitra, and R. C. Sherwood, J. Chem. Phys. **53**, 1638 (1970).

[224] L. Bogani and W. Wernsdorfer, Nat. Mater. **7**, 179 (2008).

[225] L. Liu, K. Yang, Y. Jiang, B. Song, W. Xiao, L. Li, H. Zhou, Y. Wang, S. Du, M. Ouyang, W. A. Hofer, A. H. Castro Neto, and H.-J. Gao, Sci. Rep. **3**, 1210 (2013).

[226] X. Shen, L. Sun, E. Benassi, Z. Shen, X. Zhao, S. Sanvito, and S. Hou, J. Chem. Phys. **132**, 054703 (2010).

[227] Y.-S. Fu, S.-H. Ji, X. Chen, X.-C. Ma, R. Wu, C.-C. Wang, W.-H. Duan, X.-H. Qiu, B. Sun, P. Zhang, J.-F. Jia, and Q.-K. Xue, Phys. Rev. Lett. **99**, 256601 (2007).

[228] Z. Hu, B. Li, A. Zhao, J. Yang, and J. G. Hou, J. Phys. Chem. C **112**, 13650 (2008).

[229] A. J. H. Wachters, J. Chem. Phys. **52**, 1033 (1970).

[230] P. J. Hay, J. Chem. Phys. **66**, 4377 (1977).

[231] K. Raghavachari and G. W. Trucks, J. Chem. Phys. **91**, 1062 (1989).

[232] M. Scheffler, Surf. Sci. **81**, 562 (1979).

[233] M. W. Severson, C. Stuhlmann, I. Villegas, and M. J. Weaver, J. Chem. Phys. **103**, 9832 (1995).

[234] H. Aizawa, Y. Morikawa, S. Tsuneyuki, K. Fukutani, and T. Ohno, Surf. Sci. **514**, 394 (2002).

[235] X. Lin, K. C. Hass, W. F. Schneider, and B. L. Trout, J. Phys. Chem. B **106**, 12575 (2002).

[236] P. Deshlahra, J. Conway, E. E. Wolf, and W. F. Schneider, Langmuir **28**, 8408 (2012).

[237] A. Politano, G. Chiarello, G. Benedek, E. V. Chulkov, and P. M. Echenique, Surf. Sci. Rep. **68**, 305 (2013).

[238] A. P. Graham and J. P. Toennies, Phys. Rev. B **56**, 15378 (1997).

[239] P. Rudolf, C. Astaldi, G. Cautero, and S. Modesti, Surf. Sci. **251-252**, 127 (1991).

[240] P. He and K. Jacobi, Phys. Rev. B **53**, 3658 (1996).

[241] S.-Å. Lindgren, C. Svensson, L. Walldén, A. Carlsson, and E. Wahlström, Phys. Rev. B **54**, 10912 (1996).

[242] U. Seip, I. C. Bassignana, J. Küppers, and G. Ertl, Surf. Sci. **160**, 400 (1985).

[243] A. Görling, L. Ackermann, J. Lauber, P. Knappe, and N. Rösch, Surf. Sci. **286**, 26 (1993).

[244] H. Kondoh, H. Orita, and H. Nozoye, J. Phys. Chem. **99**, 8790 (1995).

[245] G. Blyholder, J. Phys. Chem. **68**, 2772 (1964).

[246] P. Jakob and A. Schiffer, Surf. Sci. **603**, 1135 (2009).

[247] M. Endlich, S. Gozdzik, N. Néel, A. L. da Rosa, T. Frauenheim, T. O. Wehling, and J. Kröger, J. Chem. Phys. **141**, 184308 (2014).

[248] G. Kresse and J. Hafner, Phys. Rev. B **47**, 558 (1993).

[249] G. Kresse and J. Hafner, Phys. Rev. B **49**, 14251 (1994).

[250] G. Kresse and J. Furthmüller, Comput. Mater. Sci. **6**, 15 (1996).

[251] G. Kresse and J. Furthmüller, Phys. Rev. B **54**, 11169 (1996).

[252] J. Neugebauer and M. Scheffler, Phys. Rev. B **46**, 16067 (1992).

[253] J. Klimeš, D. R. Bowler, and A. Michaelides, J. Phys.: Condens. Matter **22**, 022201 (2010).

[254] J. Klimeš, D. R. Bowler, and A. Michaelides, Phys. Rev. B **83**, 195131 (2011).

[255] M. Methfessel and A. T. Paxton, Phys. Rev. B **40**, 3616 (1989).

[256] J. Lauterbach, R. W. Boyle, M. Schick, W. J. Mitchell, B. Meng, and W. H. Weinberg, Surf. Sci. **350**, 32 (1996).

[257] W. P. Krekelberg, J. Greeley, and M. Mavrikakis, J. Phys. Chem. B **108**, 987 (2004).

[258] M. Gajdoš, A. Eichler, and J. Hafner, J. Phys.: Condens. Matter **16**, 1141 (2004).

[259] P. S. Bagus, C. J. Nelin, W. Müller, M. R. Philpott, and H. Seki, Phys. Rev. Lett. **58**, 559 (1987).

[260] S. A. Wasileski, M. T. M. Koper, and M. J. Weaver, J. Phys. Chem. B **105**, 3518 (2001).

[261] K. Momma and F. Izumi, J. Appl. Cryst. **44**, 1272 (2011).

[262] M. Mamatkulov and J.-S. Filhol, Phys. Chem. Chem. Phys. **13**, 7675 (2011).

[263] R. F. W. Bader, *Atoms in Molecules* (Oxford University Press, Oxford, 1990).

[264] G. Henkelman, A. Arnaldsson, and H. Jónsson, Comput. Mater. Sci. **36**, 354 (2006).

[265] R. M. Badger, J. Chem. Phys. **2**, 128 (1934).

[266] G. Witte, J. Braun, A. Lock, and J. P. Toennies, Phys. Rev. B **52**, 2165 (1995).

[267] G. Lange, J. P. Toennies, P. Ruggerone, and G. Benedek, Europhys. Lett. **41**, 647 (1998).

[268] J. Lobo, D. Farías, E. Hulpke, J. P. Toennies, and E. G. Michel, Phys. Rev. B **74**, 035303 (2006).

[269] R. Larciprete, S. Ulstrup, P. Lacovig, M. Dalmiglio, M. Bianchi, F. Mazzola, L. Hornekær, F. Orlando, A. Baraldi, P. Hofmann, and S. Lizzit, ACS Nano **6**, 9551 (2012).

[270] S. Ulstrup, M. Andersen, M. Bianchi, L. Barreto, B. Hammer, L. Hornekær, and P. Hofmann, 2D Mater. **1**, 025002 (2014).

[271] E. Grånäs, J. Knudsen, U. A. Schröder, T. Gerber, C. Busse, M. A. Arman, K. Schulte, J. N. Andersen, and T. Michely, ACS Nano **6**, 9951 (2012).

[272] N. A. Vinogradov, K. A. Simonov, A. V. Generalov, A. S. Vinogradov, D. V. Vyalikh, C. Laubschat, N. Mårtensson, and A. B. Preobrajenski, J. Phys.: Condens. Matter **24**, 314202 (2012).

[273] E. Gråsäs, M. Andersen, M. A. Arman, T. Gerber, B. Hammer, J. Schnadt, J. N. Andersen, T. Michely, and J. Knudsen, J. Phys. Chem. C **117**, 16438 (2013).

[274] M. Petrović, I. Šrut Rakić, S. Runte, C. Busse, J. T. Sadowski, P. Lazić, I. Pletikosić, Z.-H. Pan, M. Milun, P. Pervan, N. Atodiresei, R. Brako, D. Šokčević, T. Valla, T. Michely, and M. Kralj, Nat. Commun. **4**, 2772 (2013).

[275] S. Schumacher, F. Huttmann, M. Petrović, C. Witt, D. F. Förster, C. Vo-Van, J. Coraux, A. J. Martínez-Galera, V. Sessi, I. Vergara, R. Rückamp, M. Grüninger, N. Schleheck, F. Meyer zu Heringdorf, P. Ohresser, M. Kralj, T. O. Wehling, and T. Michely, Phys. Rev. B **90**, 235437 (2014).

[276] M. Andersen, L. Hornekær, and B. Hammer, Phys. Rev. B **90**, 155428 (2014).

[277] G. Profeta, M. Calandra, and F. Mauri, Nat. Phys. **8**, 131 (2012).

[278] B. M. Ludbrook, G. Levy, P. Nigge, M. Zonno, M. Schneider, D. J. Dvorak, C. N. Veenstra, S. Zhdanovich, D. Wong, P. Dosanjh, C. Straßer, A. Stöhr, S. Forti, C. R. Ast, U. Starke, and A. Damascelli, Proc. Natl. Acad. Sci. U.S.A. **112**, 11795 (2015).

[279] M. M. Ugeda, D. Fernández-Torre, I. Brihuega, P. Pou, A. J. Martínez-Galera, R. Pérez, and J. M. Gómez-Rodríguez, Phys. Rev. Lett. **107**, 116803 (2011).

[280] S. Standop, O. Lehtinen, C. Herbig, G. Lewes-Malandrakis, F. Craes, J. Kotakoski, T. Michely, A. V. Krasheninnikov, and C. Busse, Nano Lett. **13**, 1948 (2013).

[281] M. M. Ugeda, I. Brihuega, F. Guinea, and J. M. Gómez-Rodríguez, Phys. Rev. Lett. **104**, 096804 (2010).

[282] B. Wang and S. T. Pantelides, Phys. Rev. B **86**, 165438 (2012).

[283] M. S. Dresselhaus, G. Dresselhaus, and A. Jorio, *Group Theory: Application to the Physics of Condensed Matter* (Springer, Berlin, 2008).

[284] M. W. Wong, Chem. Phys. Lett. **256**, 391 (1996).

[285] J. M. L. Martin, J. El-Yazal, and J.-P. François, J. Phys. Chem. **100**, 15358 (1996).

[286] J. Spanget-Larsen, Chem. Phys. **240**, 51 (1999).

[287] W. Liu, V. G. Ruiz, G.-X. Zhang, B. Santra, X. Ren, M. Scheffler, and A. Tkatchenko, New J. Phys. **15**, 053046 (2013).

[288] W. Liu, J. Carrasco, B. Santra, A. Michaelides, M. Scheffler, and A. Tkatchenko, Phys. Rev. B **86**, 245405 (2012).

[289] J. Carrasco, W. Liu, A. Michaelides, and A. Tkatchenko, J. Chem. Phys. **140**, 084704 (2014).

[290] Y. J. Chabal, Surf. Sci. Rep. **8**, 211 (1988).

[291] E. Kampshoff, E. Hahn, and K. Kern, Phys. Rev. Lett. **73**, 704 (1994).